

# **Dynamic Self-Assembly of Magnetic Colloidal Particles**

Von der Universität Bayreuth

zur Erlangung des Grades eines

Doktors der Naturwissenschaften (Dr. rer. nat.)

Genehmigte Abhandlung

Von

Nebojša Časić

geboren am 17. Februar 1980 in Pakrac/Jugoslawien

1. Gutachter: Prof. Dr. Thomas M. Fischer
2. Gutachter: Prof. Dr. Werner Köhler

Tag der Einreichung: 13.05.2013

Tag des Kolloquiums: 12.07.2013



*Où finit le télescope,*

*Where the telescope ends,*

*le microscope commence.*

*the microscope begins.*

*Lequel des deux a la vue la plus grande?*

*Which of the two has grander view?*

***“Les Misérables”***

***Victor Marie Hugo***



*Овај докторски рад посвећујем мојим  
родитељима.*



# Abstract

Dynamic self-assembly represent one of the most powerful tools in Nature to spontaneously organize a system on a hierarchy of different scales. Most of the processes at the nano/micro scale occur at very low Reynold's number where inertia can be neglected. Creeping flow magnetic systems can be characterized by the Mason number. The Mason number measures the ratio between the viscous and the magnetic torque and is the main parameter governing the behavior of paramagnetic colloids investigated in this thesis. The work presented in this thesis explores new dynamic regimes of colloidal dynamics which occur when suddenly switching to high Mason numbers.

In a static magnetic field the equilibrium structure of paramagnetic colloids are chains. At high Mason number in a rotating magnetic field the time averaged equilibrium conformation is a two dimensional cluster. By switching from a static to a rotating magnetic external field, we cause a transient dynamics from a static to the dynamic equilibrium state. The first question addressed in this thesis is: what is the physics that determines the transient folding pathway from one to the other equilibrium state?

Dynamic magnetic fields were used by others to propel top down DNA-linked chains of paramagnetic colloids in a liquid. The second question asked is whether we can dynamically self assemble swimmers taking a fully bottom up approach? The third question is: is it possible to assemble more complex dynamic patterns that lead to motion of the swimmers governed by more collective coupled hydrodynamics that goes beyond slender body theory of the linked chains?

This thesis answers the three questions and contributes to the understanding of colloidal dynamics and self assembly in dynamic magnetic fields in the regime of high Mason numbers. We explore two aspects of the dynamic self assembly i.e. the transient kinetics between two dynamic self-assembled equilibria and the dynamically self assembled propulsion of magnetic swimmers beyond slender body hydrodynamics. The thesis therefore aims at achieving magnetic control over the assembly of complex dynamic colloidal structures.

# Ausgangsfragestellung

Die dynamische Selbstassemblierung ist eines der effektivsten Konzepte, die in der Natur zur spontanen Organisation hierarchischer, sich über verschiedene Längenskalen erstreckender, Strukturen führt. Viele Prozesse, welche auf nanoskopischen oder mikroskopischen Längenskalen ablaufen, können durch sehr kleine Reynoldszahlen charakterisiert werden, so dass die Trägheit keine Rolle für den physikalischen Mechanismus spielt. Kriechender Fluss magnetischer Systeme kann deshalb durch eine einzige dimensionslose Größe, die Mason Zahl, charakterisiert werden, die das Verhältnis zwischen viskosen und magnetischen Drehmomenten misst. Sie bestimmt das physikalische Verhalten in dieser Arbeit untersuchter paramagnetischer Kolloide. Die vorliegende Arbeit untersucht neue dynamische Regionen der kolloidalen Dynamik, welche dadurch erschlossen werden, dass das ursprünglich bei niedrigen Masonzahlen vorliegende System abrupt hohen Masonzahlen ausgesetzt wird.

Die Gleichgewichtskonformation paramagnetischer Kolloide in einem statischen Feld besteht aus Kolloidketten. Bei hohen Masonzahlen, in einem dynamischen Magnetfeld ist die zeitgemittelte Gleichgewichtsstruktur ein zweidimensionaler Cluster. Durch das plötzliche Umschalten von einem statischen zu einem rotierenden Magnetfeld wird eine transiente Dynamik zwischen beiden Gleichgewichtskonformationen verursacht. Die erste mit dieser Arbeit untersuchte Frage ist: welche physikalischen Mechanismen bestimmen den transienten Faltungspfad von der einen zur anderen Gleichgewichtskonformation?

Dynamische Magnetfelder wurden von anderen Gruppen dazu benutzt DNS-verknüpfte paramagnetische Kolloidketten in einer Flüssigkeit schwimmen zu lassen. Die zweite, in dieser Arbeit untersuchte Frage lautet: Ist es auch möglich einen mikroskopischen Schwimmer aus seinen Einzelteilen mit einem *bottom up* Ansatz dynamisch selbst zu assemblieren? Die dritte in dieser Arbeit zu klärende Frage ist: Lassen sich komplexere Muster dynamisch selbst assemblieren, die zu einer Schwimmbewegung führen, welche über eine hydrodynamische ungekoppelte Theorie schlanker Körper hinausgeht und eine Beschreibung mittels kollektiv gekoppelter Hydrodynamik zwischen den Einzelteilen notwendig macht?

Die vorliegende Dissertation beantwortet die drei Fragen und trägt zum Verständnis der kolloidalen Dynamik der Selbstassemblierung in zeitabhängigen Magnetfeldern bei hohen Masonzahlen bei. Es werden zwei Aspekte der dynamischen Selbstassemblierung: zum einen die transiente Kinetik zwischen zwei dynamisch selbst assemblierten Gleichgewichtskonformationen, zum anderen die dynamisch selbst assemblierte Vorwärtsbewegung eines magnetischen nicht schlanken Schwimmers, untersucht. Das mit dieser Arbeit verfolgte Ziel ist die magnetische Kontrolle über die Assemblierung komplexer kolloidaler Strukturen.



# Table of Contents

1 General introduction .....	1
2 Introduction and background .....	5
2.1 Dynamic self-assembly .....	5
2.2 Magnetorheological (MR) fluids .....	15
2.3 Dynamic self-assembly of magnetorheological fluids.....	22
2.3.1 Dynamic self-assembly of magnetorheological fluids at low Mason number .....	22
2.3.2 Linear increase from small to large Mason Number .....	27
2.3.3 Nonlinear increase from small to large Mason number .....	30
3 Theoretical concepts and simulation methods.....	31
3.1 Magnetic properties of materials .....	31
3.2 Hydrodynamic equations and Reynolds number .....	32
3.3 Magnetic dipole interaction .....	36
3.4 Mason number $Mn$ .....	40
3.5 Motion between particles in the fluid and simulation methods .....	43
3.5.1 Method of reflection: the Rotne-Prager approximation.....	44
3.5.2 Lubrication theory, shearing, squeezing and the fluid particle dynamics (FPD) method.....	48
3.6 Overdamped sine-Gordon and double sine-Gordon equation .....	50
4 Experimental setup .....	57
4.1 Friction-controlled bending solitons as folding pathway toward colloidal clusters .....	57

4.2 Dynamic conformations of self-assembled helical ribbons.....	58
4.3 Healing of the ribbons, frequency and eccentricity dependent colloidal structures .....	59
5 Experimental results .....	61
5.1 Friction-controlled bending solitons as folding pathway toward colloidal clusters .....	61
5.1.1 Introduction.....	61
5.1.2 Results and discussion .....	64
5.1.3 Conclusion .....	74
5.2 Dynamic conformations of self-assembled helical ribbons.....	75
5.2.1 Introduction.....	75
5.2.2 Results and discussion .....	77
5.2.3 Conclusion .....	92
5.3 Healing of the ribbons, frequency and eccentricity dependent colloidal structures .....	93
5.3.1 Introduction.....	93
5.3.2 Assembling and healing of colloidal ribbon .....	94
5.3.3 Compression and expansion with self-assembled paramagnetic particles structures .....	99
5.3.4 Conclusion .....	104
6 Materials and Methods .....	105
6.1 Materials .....	105
6.1.1 Paramagnetic colloidal particles and ferrofluid droplets .....	105
6.1.3 Optical Microscopy and video analysis .....	107

6.2 Methods.....	110
6.2.1 Friction-controlled bending solitons as folding pathway toward colloidal clusters.....	110
6.2.2 Dynamic conformations of self-assembled helical ribbons .....	111
6.2.3 Healing of the ribbons, frequency and eccentricity dependent colloidal structures .....	112
6.2.4. Preparing the PSS solution.....	113
6.2.5. Coating with PSS solution.....	113
7 Summary.....	115
Zusammenfassung.....	117
8 Bibliography .....	120
Acknowledgement .....	132



# 1 General introduction

In the past few decades we have been confronted with a general trend of miniaturization. Such a trend is observed in many products, including computer chips, transistors, targeted drug delivery, microstirrers and microchannels. To achieve continued miniaturization, scientists and engineers search for a solution to problems they encounter and try to explain physical behavior at micro- and nano-scales where systems have rather different behavior to those observed in the macroscopic world. One of the key problems encountered with extreme miniaturization is finding tools and skills that can assemble components at the micro and nanometer scale. Because of the limitation that, today's available engineering skills and tools experience when they are confronted with the systems that are in micrometer and nanometer range, it is necessary to find new approach for this range of sizes. To solve this problem science and engineering are searching for a new approach and ideas that can organize and build systems even on these small scales. One of the commonly used, relatively simple, modeling systems for some more complex interactions are colloidal suspensions. Like so many times in the past, possible solutions to engineering problems can be found in nature. Nature has one very efficient tool for building and organizing living and non-living things called self-assembly. Self assembly is the way in which Nature organizes parts from atomic up to galactic scales. Living cells are self-assembled systems. Self-assembly can be one of the practical ways to realize ensembles of nanostructures and further the progress of nanotechnology and robotics. Self-assembly can be used for dynamic, multicomponent systems, smart materials, self-healing structures up to netted sensors, pattern bridges and computer networks [57].

Soft matter systems such as polymers and colloidal suspensions can serve as a simple model for research on self-assembled systems. Colloidal suspensions are mesoscopic systems, where complex structures and dynamics resulting from simple and tunable interactions between individual particles can be studied in real space. Paramagnetic particles, which can be produced in a wide range of sizes and can carry different functional groups, in a combination with external magnetic, electric or optical field parallel to x and/or y and/or z-axis can be very powerful tools in the attempt to realize simple but functional self-assembled systems. Uniaxial magnetic fields (static and dynamic) will induce a magnetic moment in paramagnetic particles which will lead to the self-assembly mainly driven by head-to-tail interaction. As the result of this

interaction particles become organized into chain-like structures. Biaxial fields, created by combining two orthogonal alternating magnetic fields with the same frequency but with  $\pi/2$  phase shift with respect to each other can lead to net attractive interactions in a plane. This attraction will result in a dynamic self-assembly of aggregated structures which can include crystal clusters, sheet-like structures, networks and membranes. Triaxial magnetic fields, which represent the combination of three orthogonal magnetic fields, where at least two must vary in time, can lead to even more complex structures and interactions [58, 59].

Self-assembled systems can be used as devices to measure intra-cell viscosity for the viscosity measuring in the cells, as micro mixers, membranes, or for targeted drug delivery amongst other uses. In the last decade there has been growing interest in developing propelling systems using paramagnetic particles. For this purpose scientists have created dynamic self-assembled systems in the bulk and also at the interface (liquid-liquid and liquid-air respectively). In both cases spontaneous symmetry breaking leads to propulsion in self-assembled systems [58]. Paramagnetic particles can be connected to DNA or some polymer linkages resulting in flexible structures which can then be further manipulated with magnetic fields or with optical tweezers [18, 60]. Magnetic interactions are not screened in solution which gives them an advantage compared to electric interactions [59].

Understanding the principles of self-assembly, both static and dynamics, is vital for the continued development of synthetic tools to manipulate organic and inorganic building-blocks over several length scales. Self-assembly can help to create novel kinds of integrated biological, physical and chemical systems in nanotechnology [58]. The variety of the shapes can also contribute to a better understanding of self-assembly [61].

Driven by the desire to obtain a deeper understanding of dynamic self-assembly, we have performed and presented experimental work using micrometer-size paramagnetic particles which were self-assembled in biaxial and triaxial magnetic fields.

In Chapter 2 I have presented an overview of work on similar systems to the one that I have used. Here one can find results from different researchers studying systems where the Mason number ( $Mn$ )(defined in Chapter 3.4) is very small or  $\geq 1$ , and a summary of different systems able to achieve propulsion. Chapter 3 provides insights into the theoretical concepts used to perform and explain experimental results. Here we

also give an explanation of the numerical and simulation methods used during the work presented in this thesis. In Chapter 4 I have briefly described experimental setup and the external field configuration. Chapter 5 details the experiments performed in this thesis with explanations of the observed phenomena. In Chapter 6 I have extended the experimental setup shown in Chapter 4 and describe in more detail materials and methods used to obtain experimental results presented in Chapter 5. Finally I have summarized our results in Chapter 7. Chapter 8 gives an overview of the literature.



# 2 Introduction and background

## 2.1 Dynamic self-assembly

Keeping in mind the breadth of the different branches of today's scientific research in many areas, including multidisciplinary endeavours incorporating aspects of biology, chemistry, physics etc. one can pose the question: what is self-assembly? Alternatively, considering the fact that self-assembly plays a role in different processes from the molecular level up to the scale of planets and galaxies one can pose the opposite question: what is not self-assembly?

Assembly is defined in the Merriam-Webster's Dictionary as the process of "*fitting together* of manufactured *parts* into a complete machine, structure, or unit of a machine [62]. B. A. Grzybowski et al. propose the following definition of self-assembly: "*Self-assembly is the spontaneous formation of organized structures from many discrete components that interact with one another directly (e.g., by electrostatic repulsions) and/or indirectly, through their environment (e.g., magnetohydrodynamic SA)*" [63].

As we can see from the definition of assembly the emphasis is on "*fitting together*" and "*parts*" and self-assembly points to autonomous organization (they put themselves together) of these "*parts*" (basic building blocks) into the patterns or structures without direction by an external influence (i.e. without human intervention). The principles of self-assembly are very ingrained throughout nature and technology and can involve components from the molecular to the planetary scale. Many different kinds of interactions are involved in self-assembly [63, 64].

Self-assembly can be divided in two main categories: static and dynamic self-assembly (examples for different types of self-assembly are shown in Table 1.). In general, the distinction between the two types can be made on the basis of energy dissipation and equilibrium state. Static self-assembly (SSA) systems do not dissipate energy and have achieved global or local equilibrium. This refers only to the final self-assembled structure. In fact, to achieve static self-assembly one must drive the system away from equilibrium by supplying (externally) energy to the system in order to

generate stable structures. These structures are then characterized by zero entropy production. Examples of static self-assembled systems are molecular crystals, globular proteins, quasi-crystals, lipid bilayers, pairing of bases, folding of some proteins etc. To form these ordered structures by static self-assembly may require energy, but once the structures are formed they remain stable and do not dissipate the energy. In other words, structures made by static self-assembly cannot be further adjusted/reconfigured and it is not possible to change their function even if there is a change in external conditions. In this way they can be defined as “crystals,” and not as “cells” [65].

In contrast to static self-assembly, the formation of ordered structures or patterns between components by dynamic self-assembly (DySa) requires that the system is dissipating energy. Once the flow of energy ceases structures will collapse and be disassembled (“die”). Since dynamic self-assembly takes place in a non-equilibrium regime the law of entropy maximization is not valid. As a result, dynamically self-assembled systems can dwell in a low entropy state in which they can be often characterized by complex spatial or coherent spatio-temporal organization. This feature enables the self-assembly system to be systematically designed and controlled by dissipative interactions (by continuous supply of energy to the system) [63]. Examples of dynamically self-assembled systems are compositional patterns formed by competition between reaction and diffusion in oscillating chemical reactions, biological cells, behavior of actin filaments, histones and chromatin, magnetorheological fluids, electrorheological fluids, magnetohydrodynamic self-assembly Rayleigh-Bernard convection cells, patterns that form in fluidized beds of particles etc. The majority of today’s research in self-assembly has focused on the understanding and examination of static self-assembly, but the greatest opportunities and challenges lie in studying dynamic self-assembly.

In Figure 2.1 we show schematically the principal difference between static and dynamic self-assembly. Static self-assembly will organize in the way that is necessary to minimise the thermodynamic potential. During the process of structure assembly, the system can dissipate energy, which is normally released as heat to the surrounding environment. Once the structure is assembled into the stable structure, the system will stay in a local minimum of thermodynamic potential without “losing” any more energy to the surroundings. In contrast, dynamically self-assembled systems will dissipate energy during the process of organization into the ordered structure and during the maintenance of this structure. Once the flow of energy to the system ceases, the structure will fall apart. Varying the energy flow into dynamically self-assembled

systems can cause the system to adjust into different configurations by processes which can be completely reversible [66].

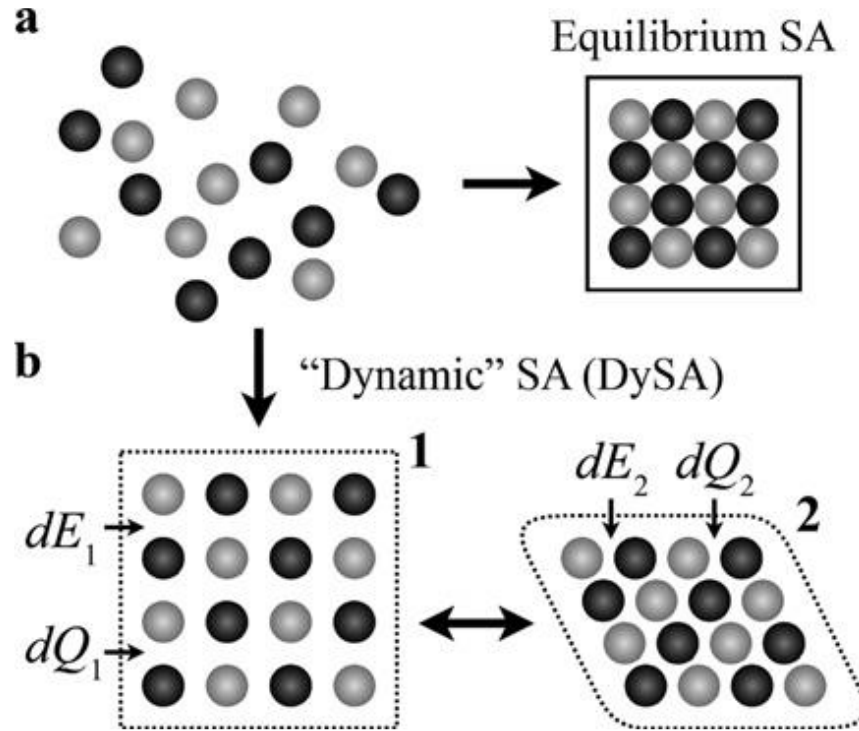


**Fig. 2.1:** Equilibrium vs. dynamic self-assembly. (a) equilibrium (static) self-assembly. Components of the system will organize in such a way to accomplish a state of thermodynamic potential minimisation. (b) nonequilibrium or “dynamic” self-assembly (DySA). Components of the system will organize and stay together only through a continuous supply of energy,  $dE$ . This energy  $dE$  will dissipate from the system as heat,  $dQ$ . Dynamic self-assembly system may adjust into the different configurations depending on the rate of energy input. This figure was taken from Ref. [66].

Further to static and dynamic self-assembly, there can be defined two subgroups, so-called template (T) self-assembly and biological (B) self-assembly. Templated self-assembly involves interactions between the components of the system and regular features in their environment which determine the structures that form. Crystallization of colloids in three-dimensional optical fields, crystallization on surfaces that determine the morphology of the crystal are two examples of templated self-assembly. The template often comprises a 2D substrate. This substrate is usually treated, mechanically or/and chemically, in the way required to build the pattern that can selectively interact with components of the system that one wishes to assemble.

These patterns will govern the organization and assembling of the components through the interaction between components of the system and the substrate. Large particles on the interface (which can serve as a template) can be used to direct the self-assembly of smaller particles (which are called substrate) on the other interface. In template self-assembly (TSA) one can use a prefabricated template structure in order to i) orient and direct structures that will have better long-range order than non-templated ones, ii) form novel structures/phases which will be very difficult or impossible to build without template and/or iii) control the form and structure of assemblies [57, 63, 67]. The main characteristic of biological self-assembly (BSA) is a high complexity and wide variety of functions that can be made.

Beside these different kinds of self-assembly G. A. Ozin et al. present a slightly different partition of static and dynamic self-assembly. They divide static and dynamic self-assembly into three different sub-sections: co-assembly, hierarchical self-assembly and directed self-assembly. The divisions between these different types of self-assembly is rather blurred. Co-assembly can be defined as simultaneous self-assembly of different building blocks (which are the part of the same system) which leads to a synergic architecture that could not have been produced by the isolated self-assembly of individual building blocks. Hierarchical self-assembly can be defined as the organization of a single building block over multiple length scales. Directed self-assembly represents the case where self-assembly is directed by some external forces. Directed self-assembly represent the typical case for bottom-up-meets-top-down approaches (for example, using a lithographic pattern to direct the self-assembly of colloids from solution on a substrate, garnet films). Bottom-up and top-down approaches to self-assembly will be discussed in more detail later in this Chapter [64].

One of the main prerequisites for self-assembly to take place at all is the mobility of the self-assembling components. By mobility we mean the ease with which components can move with respect to each other. Because of this requirement, self-assembly usually takes place in fluid phases or on smooth surfaces. If components irreversibly stick together during the collision, they will form a glass rather than a crystal or some other regular structure. As previously mentioned, dynamic self-assembly will occur only when system is in a nonequilibrium state and able to dissipate energy. This feature of dynamic self-assembly is key to the development of strategies for preparing different structures and materials. Controlling the amount of externally energy delivered to the system, one can control properties and internal organization of the system (e.g., as tunable optical elements, sensors or reconfigurable machines) [57].

System	Type	Applications/importance
Atomic, ionic, and molecular crystals	S	Materials, optoelectronics
Phase-separated and ionic layered polymers	S	
Self-assembled monolayers (SAMs)	S, T	Microfabrication, sensors, nanoelectronics
Lipid bilayers and black lipid films	S	Biomembranes, emulsions
Liquid crystals	S	Displays
Colloidal crystals	S	Band gap materials, molecular sieves
Bubble rafts	S	Models of crack propagation
Macro- and mesoscopic structures (MESA)	S or D, T	Electronic circuits
Fluidic self-assembly	S, T	Microfabrication
Light matter <sup>66</sup>	D, T	
Oscillating and reaction-diffusion reactions	D	Biological oscillations
Bacterial colonies	D, B	
Swarms (ants) and schools (fish)	D, B	New models for computation /optimization
Weather patterns	D	
Solar systems	D	
Galaxies	D	

**Table 2.1:** Different examples of self-assembly. Here letters denotes different types of self-assembly: S- static; D-dynamic; T-templated and B-biological self-assembly. This table was taken from Ref. [57].

Over time, Nature has developed very efficient ways to control self-assembly from the atomic and subatomic length scales up to cosmological length scales. At present, Humans are not as successful. At the present day we are able to control some

aspects of self-assembly from atomic scale to meter scale. One of the reasons for this limited range is the difficulty in achieving full control over the tools and methods which will allow us to control the size of building blocks, shape and surface properties to a high level of precision. There are two different approaches by which matter can be shaped, positioned and organized in the process of self-assembly. One is bottom-up approach and the second one is top-down approach. Today's science and technology uses the top-down approach in most of the self-assembly systems, contrary to Nature where the bottom-up approach is the main tool to realize self-assembling systems and different structures. In the top-down approach one tries to find and derive simple mathematical models that can, in adequately describe and predict the behavior of the target system [68]. Most of today's methods of top-down approach are based on two steps. The first step consists of writing down the features on the substrate (e.g., by optical and e-beam lithography). The second step consists of deposition or etching processes in which microscopic and/or nanoscopic features are engraved into the substrate. The top-down approach has been successfully used in the process of dynamic self-assembly using Langmuir–Blodgett (LB) transfer or dip-coating, reaction-diffusion, complex systems (e.g., Benard convection), swarming of motile organisms networks etc. The main disadvantage of this method is a limitation to existing experimental arrangements and the absence of potential to create new ones [64, 68, 69].

From both approaches we have learnt that matter of all kinds (colloids and polymers, atoms and molecules) can experience spontaneous organization to a higher level of structural complexity. This ordering is driven by different forces acting over different length scales. To realize a high efficiency of self-assembly and self organization we need to be able to synthesize building blocks with specified dimensions and form. Furthermore, we need to control their surface properties (e.g., charge, functionality, hydrophobicity, hydrophilicity), thereby gaining command over the attractive and repulsive forces between them in order to assemble structures over multiple length scales and create systems (physical, chemical, or biological systems) with appropriate functionality. Among the scientific community there is a discussion about whether the top-down or bottom-up approach is most conducive to further advancement. While until now the top-down approach have given very good results in order to achieve the particular nanofabrication objectives, it would be very difficult to imagine top-down methods that could match the flexibility and power of the bottom-up self-assembly approach. For example it is hard to imagine how one can be able; using the top-down approach, to match the bottom-up approach for producing an inorganic nanowires with diameters below 2 nm [64].

For successful realization of a self-assembling system one needs to use particles with well-defined and narrow distributions in size and shape. Typical particles used in self-assembly are spherical but recently there have been reported other particle shapes such as anisometric colloids, ellipsoids (produced by stretching of spherical particles), anisotropic particles that have been produced by microcontact printing, selective deposition and interfacial reaction and also polyhedral building blocks created from spherical particles. These new particles and structures have the potential to extend the range of structures that can be made with colloids [61]. To realize a successful self-assembly system, one needs to find a way to “program” the components of the system in such a way that they can organize, reorganize and transform themselves into the controllable and desired structure [63].

Grzybowski B. A. et al. [63] propose a useful four-step strategy to design dynamic (non-equilibrium) self-assembled systems. The first step consists of the identification of suitable structures. This means that at least one type of interaction in the system must be regulated and depends on the externally delivered energy (external magnetic field, intense optical field, hydrodynamic flows etc.). The second step is choosing “competing” interactions. This means that if only one type of force is present in the system it will fall apart (if only repulsive forces are present) or “stick” together but in a disordered way (if only attractive forces are present). Only if we have competition of these two forces in the system is it possible to realize and govern a self-assembling system. The third step consists of the choice of length scale. At this length scale, the magnitudes of the attractive and repulsive forces acting on the system need to be similar. To make this choice one needs to have knowledge of the material properties of the surrounding medium, how individual interactions scale with object size, what is the distance between objects etc. The fourth step consists of synthesis. Dynamically self-assembling systems should be built from simple components. This can be accomplished by “bottom-up” approach where a system of complex materials can be formed from simple reactants. More details can be found in Refs [61] and [63].

The number of different methods to manipulate self-assembly systems, both static and dynamic, has increased in the last few decades. Among these methods, present in the laboratory and in nature, are light, temperature, solvent polarity, or even concentration of certain additives (ions). All of these methods can be very useful ways to realize self-assembly. One of the powerful methods for realizing and tailoring the mechanical, optical, and electronic properties of materials during self-assembly is the application of external fields: electric, magnetic or a combination of both fields [70]

For all the above mentioned reasons, the field-directed self-assembly method promises to be a very serious candidate in the bottom-up fabrication of novel materials and devices. In externally derived fields, particles will be polarized (electric field) or magnetized (magnetic field) which leads to anisotropic dipole-dipole interaction between particles. When the dipole-dipole interaction is strong enough to overcome the Brownian motion, particles will organize into chains and more complex structures. The ratio between the thermal energy and the maximum of dipole-dipole interaction is characterized by the dipole strength  $\lambda$  (equation 3.23). More details about dipole-dipole interaction can be found in Chapters 2.2 and 3.3 [70].

One of the main advantages of the external-field (electric, magnetic, and optical) directed self-assembly (here field is used as a physical template) is the possibility that fields can be tuned dynamically and switched on/off. Specifically, when the applied field is static and time-independent, it behaves like a physical template, modifying the free energy landscape on which the components evolve and guiding their assembly toward structures characterized by new energy minima. For example, optical fields are used in “optical tweezers” to direct polarizable particles to regions of highest field strength (three-dimensional colloidal crystals, two-dimensional colloidal assemblies used for epitaxial growth). Using uniform electric fields one can template assemblies with improved long-range order and controlled orientation (diblock copolymers, highly ordered lamellar and cylindrical domains). Using static and dynamic magnetic fields, it is possible to orientate the magnetic domains of nano/micrometer particles and self-assemble these particles into more complex structures. Using a time-varying (dynamic) magnetic field one can construct structures that have no template-like analogies. Dynamic magnetic fields can be used to agitate an equilibrium structure in order to remove energetically undesirable defects from the system and to build-up and preserve the self-assembled system [63]. In the magnetic field magnetic colloids can organize into linear chains, zigzag chains, magnetic nanowires, 2D arrays, pyramids [71], rings, static and dynamic lattices on the surface of fluids etc. [59].

One of the very popular ways to realize dynamic self-assembled systems is to use capillary forces. These forces act on the particles trapped between two interfaces (liquid-liquid or liquid air). Because the methods of capillarity-induced clustering can have several disadvantages, such as lack of long-range order, clusters can have a various number of defects. It is not possible to have complete control over the self-assembly processes, so methods utilizing capillary forces usually incorporate external

electric or magnetic fields. An external field provides control over the interaction between the colloidal particles, leading to a greater variety of potential self-assembled structures. In this case the structures are strongly dependent on the parameters of the external field [58].

Snezhko A. et al. have created a system of snakelike self-assembled structures in an ensemble of magnetic microparticles placed at the liquid-air interface. This structure was induced by an alternating (AC) magnetic field. By attaching a large bead to a magnetic snake (bead-snake hybrid) they were able to spontaneously break the symmetry of surface flows and turn it into a self-propelled object. The magnetic snake structure was formed as a result of the interplay between surface waves on the liquid's surface and the collective response of magnetic particles to an external AC magnetic field [72, 73].

The use of capillarity-induced forces to run so-called magnetic spinners was also exploited by Grzybowski B. A. et al. [70]. In this work they created two-component rotors. In the external rotating field, the cores begin to rotate and center inside the gears, generating a hydrodynamic flow. Due to vortex-vortex repulsions only one rotor resides in a local energetic minimum. Due to localized magnetic fields created by electromagnetic actuators placed below the liquid's surface, the rotors self-assemble into a unique structure [63]. The basic principle lying behind the assembly at the interface (liquid- liquid or liquid-air, where the interface serves as a template for assembly) is the reduction in the interfacial energy. Further assemblies can be controlled by lateral interface mediated capillary forces [70].

Inspired by the propulsion of biological microorganism and bacteria, there has been a rising interest in both academia and industry, to realize self-assembled systems that can propel themselves in a microfluidic environment. To realize efficient propulsion in a nano/micro environment is a challenging task due to absence of inertia in low-Reynolds number systems. Purcell's famous "scallop theorem" summarized the difficulties that can arise to achieve any net propulsion at low Reynolds numbers [74]. For the motion at low Reynolds number (in the case of incompressible flows), the governing equations are the continuity equation and the Stokes equation (Chapter 3.2). Nature uses two different approaches to realize propulsion at low Reynolds number. One is illustrated by beating cilia and the flagella of sperm, which use rodlike polymers that are anchored to the surface. The motion of these systems consists out of two steps. The first step is power stroke and the second step is recovery stroke. The second type of

motion is used in bacterial flagellae, where hydrodynamic friction converts rotational motion of helices into propulsion along their axes [75].

Until now science has successfully developed two different ways to realize propulsion on a micro/nano scale. One way is to use chemically-powered nanomotors [76] and the other way is to use externally-powered propellers. In our work we use the latter approach. Pak O. S. et al. [77] propose further categorization of the externally-powered propellers in three separate sub-groups. The first type consists of helical propellers, which induce propulsion by the rotation imposed by an external magnetic field (this type of propulsion has been inspired by helical bacterial flagella). The second type of propellers uses an interface to break the spatial symmetry. Examples of this type of propulsion motion are called surface walkers. The third type of propeller are flexible propellers, which use the deformation of flexible filaments to realize the propulsion [77]. In the experimental work presented in this thesis we use a combination of the first and third type of propulsion motion. A question that is very close bound with the propulsion is: “What is the minimal design that is necessary to convert the rotational power of built-up structures into directed thrust in a viscous environment?” [75].

Tierno et al. [78] introduce an asymmetric paramagnetic doublet consisting of two paramagnetic particles ( $1\mu\text{m}$  and  $2.8\mu\text{m}$  in diameter) “glued” together with DNA. These doublets rotate close to a glass surface in an externally induced circular and elliptic magnetic field. According to the Purcell scallop theorem [74] two degrees of freedom are required to break the spatial symmetry. To satisfy this condition the doublet must be displaced parallel and perpendicular to the solid wall [78]. There is an example where rotating clusters have been used as stirring components to enhance mixing and biochemical reactions. Mixing accelerates chemical and biological reactions relative to diffusion-only processes. Micropumps and artificial swimmers have also been developed from the clusters run and controlled by external fields [79]. Concerning the fact that science needs to find a worthwhile<sup>1</sup> application (e.g. in economic terms must be profitable), one can pose the question: “What is the benefit of dynamic self-assembly?”. Based on the experimental point of view, Fialkowski M. et al. [65] propose three unique advantages of dynamic self-assembly over the static one.

---

<sup>1</sup> Sufficiently valuable or important to be worth one's time, effort, or interest (www.thefreedictionary.com)

The first advantage is adaptability. Dynamic self-assembled systems are also called “smart” structures. They can build themselves spontaneously from components and they are able to react to changes in the environment and transitions between different structures (as illustrated in Fig.1). Contrary to static self-assembly, dynamic self-assembly is far from equilibrium and by tuning the flow of energy to the system one can reversibly tumble different structures.

The second advantage is self-healing. For dynamical self-assembled structures, any perturbation of the system that belongs to the same phase space will return the system to its stable configuration. If the perturbation is too large, the system will transform to another kind (mode) of assembly. This is reflected in the behavior where a system is able to heal itself from small “wounds”, while for large ones it will reconfigure itself and adapt to the new conditions.

The third advantage is self-replication. To realize self-replication one needs to deliver chemical energy to the system. An example of a system capable of static self-replication is the DNA double helix. When the flow of chemical energy stops the system will cease replication, but already replicated structures will not disassemble. An example of dynamic self-replication is the replication of cells where different parts first need to self-assemble and then diffuse (migrate) to specific locations in order to assemble the cell [65].

Dynamic self-assembled structures have already found applications in robotics and manufacturing, microelectronics, nanoscience and technology, netted systems, and crystallization at all scales [57]. The truth is that we, until now, have very little knowledge explaining how dissipation of energy can lead systems from disordered components to ordered structures. Studying the methods of self assembly can be a very useful way to extend our knowledge and lead us closer to an answer to the posed question. Only the combined work of different branches of science can bring us closer to this goal.

## **2.2 Magnetorheological (MR) fluids**

Magnetic particles have great importance in many different areas of science and industry. In the last three decades there has been growing interest to find model particle systems where particles can move freely in a liquid medium. Development of the various chemical techniques and methods, such as co-precipitation, thermal

decomposition, hydrothermal synthesis, microemulsions etc., have provided a broad range of possibilities for synthesis of micrometer and nanometer size particles (spherical or elliptical), rods, chains, networks and so on. Particles can be produced in broad range of sizes and shapes, they can be monodisperse or polydisperse, with different charges and functional groups etc. Three different groups of systems can be roughly defined by their characteristics and methods of preparation:

- Ferrofluids: colloidal suspensions of ferromagnetic nanoparticles dispersed in some carrier fluids, oil or water.
- Magnetorheological (MR) fluids: colloidal suspensions of magnetic or magnetizable micro-particles immersed in a non-magnetic fluid. There is an electric analog to MR fluids, so-called electrorheological (ER) fluids.
- So-called magnetic holes: non-magnetic microparticles immersed in a ferrofluid [36].

Particles used in MR fluids (or magnetic holes) are typically in the range of micrometers or several hundreds of nanometers, in contrast to those used in ferrofluids which have sizes of nanometers up to a few tens of nanometres. Of special interest are so-called superparamagnetic particles. Superparamagnetic particles consist of nanometer size iron cores (a few tens of nanometer in size) coated with a polystyrene matrix, with functionalized groups attached to particle surfaces. The size of these particles is important because their magnetic moment induced by applied external magnetic field depends on particle volume. For MR fluids this will result in a strong magnetization of the particles and high induced dipole moments. This will lead to larger particle-particle interaction and, consequently, shorter response times and stronger mechanical actions. In this respect, MR fluids have a more important role in mechanical systems that require a fast and efficient way to control force or torque transmission and applications dealing with control of vibrations, viscosity, friction, actuation, damping, robotics etc. These applications are becoming more and more relevant to academic and industrial pursuits. J. de Vicente et al. divide applications of MR fluids into three well separated areas: 1. colloids with adjustable rheological properties, 2. patterned anisotropic self-assembled materials, and 3. sensors for monitoring mechanical vibrations. While particles used in MR fluids traditionally have a spherical shape, in the last few years there has been an increased interest in the use of non-spherical particles (spheroidal and plate-like shapes) [32, 34, 37].

In our experimental work (Chapter 5) we have mainly concentrated on MR fluids and now we will give some main characteristics and applications of them. Most of the characteristics of MR fluids are the same as for ER fluids. There are few different definitions of MR and ER fluids but in general they can be defined as colloidal dispersions of nanometer or micrometer size magnetizable particles (MR fluids) or polarizable particles (ER fluids), immersed in a carrier fluid with medium to low viscosity (i.e., silicone oil, water etc.) [32]. We will explain the advantages of MR fluids compared to ER fluids later in this thesis.

Since they were first discovered in the 1940s by the work of Rabinow and Winslow [47-49], magnetorheological (MR) and electrorheological (ER) fluids experienced a brief period of intense interest and research. After this short period, work on MR and ER fluids subsided for almost 30 years. The next considerable work was reported by Klass and Martinek on ER fluids comprised of silica and calcium titanate. From the end of 1980' until the beginning of 1990', MR and ER fluids became a subject of numerous research and has grown into a multidisciplinary field whose importance has stood up to the present day. This work, on MR and ER fluids, may have been encouraged by the Nobel Prize in physics for 1991 which was awarded to P. G. de Gennes for their work on the statistical theories of soft matter [41]. This Nobel Prize led to an increase in the amount of fundamental research in the field of soft matter and statistical physics. Using the tools provided by the field of statistical physics, one can predict the properties of soft matter. These properties can later be confirmed and exploited directly in experiments and used for the synthesis and characterization of a wide range of new materials [35].

MR and ER fluids are complex systems (complex does not mean complicated) which can exhibit a very fast reversible transition (on the order of milliseconds) from liquid to nearly solid behaviour when an external magnetic field is applied. Due to this phase transition, viscosity can change by several orders of magnitude for applied magnetic flux densities with a magnitude of  $\sim 1$  T [37]. This transition occurs as a result of the attractive induced (nonpermanent) dipolar forces between the particles which can be monitored by the application of a magnetic or electric field. The ability to accomplish a significant change in viscosity (several orders of magnitude, some authors report increase in viscosity by factor of  $10^6$  [32]) in a fraction of millisecond, is a key advantage of MR and ER fluids over conventional mechanical interfaces. MR fluids which change viscosity as a result of variations in the intensity of an external magnetic field are also known as “tunable fluids”. This “tuning”

capability of forces or torques is one of the basic properties of MR and ER fluids which provides wide opportunities for structural examination. When the external magnetic field is removed, aggregation of particles (chains, clusters, sheets or networks) will dissolve due to Brownian motion of particles and the fluid will experience transitions from a solid-like state back to a liquid-like state. This behavior appears because the dipole moment is not permanent. By removing the external field, the dipolar interaction between particles also vanishes. In this way all changes caused by the external magnetic field, in the sense of general properties of the macroscopic fluid system, can be reversed.

By changing their concentration, paramagnetic particles in an applied magnetic field can form different aggregated structures ranging from chains, networks or sheets of particles. In the case of two immiscible fluids, the size and shape of droplets can be changed by applying different fields and hence the rheology of the mixture changes. Forces opposing these aggregation processes caused by applied magnetic field, are hydrodynamic and thermal forces. The interplay between these three opposing forces leads to very rich spectrum of different types of behavior, which are not yet well understood [34, 37, 50].

MR fluids represent analogs of ER fluids and have many similar properties to ER fluids, but not without some fundamental differences. Some of these differences we will shortly explain here. More detail can be found in the cited literature. Some of the key differences and advantages of MR fluids compared to ER fluids are the absence of charge dependence, polarization of electrodes, adsorbed water, field inhomogeneities, greater stability over a broader range of temperature, higher strength etc. MR fluids are free of all of these difficulties and while they show analogous behavior when submitted to the external field (in this case magnetic field), they can serve as a better model system than ER fluids [33]. Depending on particle concentration, strength of magnetic field and composition of MR fluids, due to similar behavior as Newtonian fluid, MR fluids can demonstrate a distinct maximum in yield stress up to 100 kPa. In general they will show a Bingham plastic fluid behavior. In work with ER fluids, polarization of electrode and direct contact with fluid can generate some difficulties, which are not evident in experiments with MR fluids. Despite the aforementioned advantages of MR fluids, there are not as many experiments which include MR fluids as those involving ER fluids because tribological properties of MR fluids have not yet been well-characterized. This presents a wide

range of opportunities for future research, both theoretically and experimentally [50, 51].

One of the most prominent features of MR fluids is the fact that all questions can be studied simultaneously by experiment, computer simulation and theory. A theoretical understanding of the basic principles and mechanisms of phase transformations shows that MR fluids and colloids in general can serve as model systems for wide range of processes and phenomena in the field of condensed matter. One of the advantages of MR fluids lies in the possibility of a relatively easy and fast change in external perturbation of the system. The relaxation time of MR fluids is on the order of milliseconds, which enables experiments in real-time and real-space. Hence, most experimental results can be directly compared with theoretical predictions and computer simulations [35]. This very useful attribute of MR fluids has contributed to the rising interest for application of MR fluids as model systems for much more complicated and not yet fully understood behavior of different kind of biological and biophysical processes in nature (ranging from biological polymers to living cells) and for commercial uses. For biological research MR fluids are of special interest for measuring the viscoelastic properties of very small sample volumes. For example, for viscoelastic measurements of biological semitransparent samples which are only available in small volumes (200  $\mu\text{l}$  are sufficient). Also, using single particle chain rotation in the cell interior, one can investigate the rheology of the cytoplasm of living cells or measure the viscoelastic properties of inhomogeneous materials [38].

This growing interest in MR (and ER) fluids is accompanied by the development and application of a wide range of different techniques and methods for their observation and characterization. C. Wilhelm et al. [38] divide these microrheological methods into two distinct approaches concerning the way in which the sample or probe is manipulated. The first approach is the passive manipulation of the probe. This can be achieved by applying the external magnetic field or using optical tweezers. The second approach is that by using particles as active probes and using the fluctuation dissipation theorem, viscoelasticity can be estimated by observing the Brownian motion of the particles [38].

As already mentioned, by applying an external magnetic field, a system will experience a very fast transition from a liquid-like to a solid-like phase. As a consequence of this transition, the induced dipole moment will cause particles to aggregate into a broad range of different structures, depending on their concentration

and other experimental conditions. This transition in suspension microstructure will induce consequential change in flow properties due to restriction in fluid motion. Hence, the viscosity of the fluid and optical properties of suspension will change. This change in optical properties, which can manifest as optical anisotropy (birefringence and/or dichroism), opens the possibility of using different diffraction techniques, such as laser light and neutron diffraction. Due to the formation of chains (or more complex structures), which are optically anisotropic, dichroism arises and provides information about the number of aggregated particles versus single particles [30]. A disadvantage of optical techniques lies in the fact that they produce only an average picture of spatial and temporal effects and thus cannot be used for in-vivo examination. This disadvantage can be avoided by using relatively large microparticles ( $\geq 0,5 \mu\text{m}$ ), which is the resolution limit for usage of optical microscopy. With particles of this size one can, combining different methods of optical microscopy and video imaging tools, observe pattern formation and dynamics of individual particles in real time [32, 52].

One of the techniques based on the diffraction of light by chains of magnetic particles is the so-called magnetic chaining technique (MCT), which was introduced for the first time in 1994 by F. Leal Calderon et al. [43] and later improved and extended for smaller sample volumes. The performance and resolution of this technique is explained in more detail by R. Dreyfus et al. [44]. This method is very suitable for measurement of small interaction energies per unit area and interparticle forces up to  $10^{-13}$  N. This method is based on the following principle. By using monodisperse particles which have sizes in the range of the visible light, scattered light from each particle in the chain will interfere constructively. Using Bragg's law one can calculate the distance  $d$  between particles in the chain from the measured diffraction wavelength. Distances between particles in the chain can be controlled and tuned by changing the strength and frequency of magnetic field.

One of the methods for characterizing colloid-colloid interaction is so-called optical tweezers. Optical tweezers are powerful tools that can be used to probe and characterize the viscoelastic properties and exerted forces on molecular motors (myosin, kinesin, ribosomes etc.), composite structures (chromatin and chromosomes), DNA, aggregated protein fibers (actin), cell membranes etc. Optical tweezers work by trapping particles in regions of high optical field strength. The trapping strength is proportional to the power of the laser. A wide range of applications of optical tweezers is possible when they are combined with other techniques in the sense of creating permanent structures. However, proper use of optical tweezers is restricted to relatively

small sample areas. Use of optical tweezers over a larger area can be coupled with several difficulties. One of disadvantages of optical tweezers is significant heating caused by the optical field, which can produce undesirable effects in examination of living cells and biological materials [42, 44, 45].

The development of different experimental methods and techniques has accompanied the development of different simulation methods and theoretical models. These simulation methods can be split into methods that include hydrodynamic interaction and methods in which hydrodynamic interaction is neglected. The effect of hydrodynamic interactions between paramagnetic particles can be investigated using Stokesian dynamics (SD) and lattice Boltzmann (LB) methods. Stokesian dynamics (SD) simulation is based on two different levels of approximation of hydrodynamic interaction. One approximation is based on the additivity of forces (AF) and the other approximation is based on the additivity of velocities (AV). In particle dynamics (PD) simulations hydrodynamic interaction are neglected. Multi-body hydrodynamic interactions are governed by the motions of particles in real colloidal solutions. SD and LB methods provide tools that predict phase lag (the angle between the direction of the chain of magnetic particles and the direction of the applied external magnetic field) more accurately. On the other hand PD method can more accurately predict chain formation dynamics [46].

Since the similar governing equations can explain different systems, microscopic particles can be used as a many-body model system for describing processes that take place on a molecular scale and thus used for solving very complicated equations of motion. Comparing these results with computer simulations results can provide a new tool for solving many different problems in natural systems [32].

The potential applicability of MR fluids has triggered a vast quantity of research in developing devices that have very broad range of applications [17]. Taking into account all the aforementioned advantages and applications of MR fluids for scientific research, there is a rapidly growing interest for commercial applications of MR fluids. MR fluids have been used as models for crystalline assemblies [9], glasses [10], van der Waals crystals [11], phononic crystals [12] and dipolar chains [13]. For commercial use they have been widely used in the automotive industry in addition to many engineering applications such as shock absorbers, dampers, clutches, brakes, torque transducers, ultrafine polishing technology, seismic protection, hanging bridge

stabilization etc. providing semi-active control of systems. In medicine and biology, uses include prosthetic bioengineering, investigating properties of living materials, biomedical applications, for microfluidics motions and manipulation of small fluid droplets, for transport through cell membranes, for protein crystallization, for drug delivery and for cancer therapeutic methods [32, 35, 51].

### 2.3 Dynamic self-assembly of magnetorheological fluids

As mentioned in Chapter 2.2, induced dipole moment causes paramagnetic particles to organize into one dimensional (1D) chains when exposed to an external magnetic field. The behavior of these 1 D colloidal chains can be roughly subdivided into three different regimes following the difference in the value of the Mason number (for more details about Mason number see Chapter 3.4). In the first two regimes, which will be discussed in Chapter 2.3.1 and 2.3.2, there are different chain responses to the external rotating magnetic field. The simplest of these two behaviors is the synchronous regime where the chain follows the external magnetic field with a constant phase lag angle and for which the Mason number is slightly above zero (Chapter 2.3.1). The second regime is the asynchronous regime for which the Mason number is below or proportional to one (Chapter 2.3.2). In this case the phase lag angle between magnetization and the external magnetic field increases with time due to the rotational viscous torque preventing the chain from following the external field. A transition between the synchronous and asynchronous regimes, for a given  $Mn$ , can be calculated by solving the following equation:  $\sin(2\alpha) = 32N\eta\omega/\eta_0\chi^2H_0^2\ln(N/2)$ . As long as  $\sin(2\alpha) < 1$  the chain will rotate synchronously with the field and asynchronously when the phase lag angle is  $< \pi/4$ . For chains which length is shorter than the critical chain length, rotation is synchronous with the magnetic field. Rotation becomes asynchronous when the chain length is above the critical length for a given frequency [18]. These two regimes were the subject of numerous studies conducted by several research groups in the last two and a half decades. Later in this thesis we will describe a brand new type of behavior, which arises from a sudden switch from small to very large Mason number (Chapter 2.3.3).

#### 2.3.1 Dynamic self-assembly of magnetorheological fluids at low Mason number

When an external magnetic field is applied, dipole repulsion and attraction mechanisms cause particles to aggregate into chains parallel to the direction of the

external magnetic field, lining up and minimizing the magnetic potential energy in the system [53]. This occurs if the dipole interaction between the particles overcomes the thermal energy. The strength of the interaction can be expressed by dipole strength  $\lambda$  which is the ratio of the maximum magnetic interaction energy between two particles aligned with the external magnetic field to the thermal energy (Chapter 3.3). When the strength of the external magnetic field is sufficient, individual particles will start to organize into chains. The length of the chains depends on the strength of the applied magnetic field and on particle concentration. For high values of the magnetic field and concentration, different structures beside the 1D chains have been reported [11, 32, 34, 39, 40] (branches, clusters etc.). There are several models that describe diffusion of the particles into clusters which then also diffuse to form larger clusters (some authors use the name 1D cluster for the 1D chain of particles) [32]. Smaller chains will start to aggregate and produce longer chains (consist of many particles) in the longitudinal direction. When two chains are close to each other laterally one chain will start to diffuse towards the closer end of the other chain. When ends of these two chains are in close proximity they connect tip-to-tip and become a single longer chain. Short-range interactions are expected in chains consisting of rigid particles. Paramagnetic chains will be surrounded by a lateral field which gives rise to a repulsive or an attractive interaction. Free dipoles at the ends of the chain can have significant interaction with the ends of neighboring chains. This lateral attractive interaction between the neighboring chains can be caused either by the magnetic interaction between long chains or by magnetic fluctuations. Recent theoretical and experimental work shows that lateral attractive interaction is significantly weaker than longitudinal interaction i.e. tip-to-tip (or head-to-tail) aggregation of the chains [40]. Experimentally, the average size of the observed aggregates has been observed to scale with the inverse of the square root of the frequency of the rotating field, and the maximum number of beads for a stable chain scales with the inverse of the square root of the Mason number [39].

Experimental work performed and explained by Sonia Melle, James Martin, Lisa Gast and several other groups reveals the behavior of colloidal suspension at low values of Mason number, mostly below and slightly above one. There are two distinct behavioral regimes of colloidal suspensions in rotating fields, depending of the value of Mason number. One is called the low-frequency regime (which will be discussed in this Chapter) and the other is called the high-frequency regime (which will be discussed in Chapter 2.3.2). In the low-frequency regime, chains will rotate synchronous or with

phase lag behind the external magnetic field. In this regime chain will rotate without cracks or ruptures in chain structure [25, 26, 29, 30].

Chains of particles will rotate due to the magnetic torque  $\Gamma_m$ . As long as the magnetic torque is larger or equal to the drag torque  $\Gamma_v$ , the chain will rotate synchronously with the magnetic field. When the drag torque  $\Gamma_v$ , is larger than magnetic torque  $\Gamma_m$ , the chain will rotate asynchronously with the magnetic field, leading to a phase lag between the field direction and chain orientation (Equation 3.21) [39].

Paramagnetic chains of particles can be formed by linking particles using DNA or some other bifunctional molecules which are able to react with functional groups of the paramagnetic particles. With these methods it is possible to create very rigid chains, semiflexible chains and chains that are very flexible. In this case, instead of breaking, chains will deform when the frequency of the external magnetic field is increased. Paramagnetic chains formed in this way can be bent and stretched using optical tweezers to determine the flexural rigidity or bending stiffness of the chain. When the frictional torque surpasses the magnetic torque, chain rotation evolves from the synchronous to asynchronous regime. Increasing the frequency of magnetic field causes phase lag between the rotation of the chain and direction of external magnetic field to increase and the chain rotation slows relative to the rotation of the external magnetic field. The chain reverses direction when the phase lag angle surpasses the angle value of  $\pi/2$ , and will realign the dipole moments with the external magnetic field. This type of a rotation that consists of stop and backward motions is known as “jerky motion”.

Biswal S. L. and Gast A. P. [18] used superparamagnetic particles organized in 1D chains, where particles were linked together with flexible bis-biotin- polyethylene-glycol (PEG) spacer molecules as well as with gluteraldehyde. They showed that in the synchronous regime, some of the longer chains were folded into a shape with a smaller effective length. Varying the length of the spacer molecule they were able to tune the chain flexibility. Because the particles in the chains are linked together, the chain will, instead of breaking down, start to bend and form S- or U- shape chains or will buckle toward the chain center of mass. If one can understand the interplay between elastic, viscous and magnetic forces this would be a powerful tool for controlling the shape of variably rigid chains at various external magnetic field frequencies [18, 31].

S-shape and U-shape rotating chains have also been reported [17,30]. These two different shapes appear when the chains rotate with positive phase lag with respect to the external magnetic field. In this case ends of the chain will bend trying to decrease phase lag with the field. It can be considered that S-shaped and U-shaped rotating chains represent an intermediate state between straight chains and chain fragmentation (Chapter 2.3.2) [17, 30].

Wilhelm C. et al. [38] introduce a very interesting feature of paramagnetic particle chain related to biological applications. They use magnetic nanoparticles (“magnetic endosomes”) to probe the intracellular dynamics at local scale. The chains of these magnetic endosomes were formed inside the living cell. By measuring viscosity  $\eta$  and a relaxation time  $\tau$  (time required for relaxation of the stress), one can quantify viscoelastic properties of rotational chain compared to the rotation of the external magnetic field. Understanding aspects of the rheological behavior of cells, such as their capability to undergo applied stress, are very important for explaining and understanding cellular function (muscle contraction, adhesion, division, and spreading of the cell). Viscoelasticity of cytoplasm can be probed using the rotational microrheological technique. This technique consists of measuring the response of the chains under the application of a controlled magnetic torque. Soft materials can behave both like fluids, through their ability to dissipate mechanical energy (viscosity) and like solids, through their ability to store mechanical energy (elasticity). From the sum of a viscous and an elastic contribution one can find angular velocity and depending on the relaxation time one can distinguish between solid-like and fluid-like behavior. If  $\tau = \infty$ , one can define medium as a purely elastic and when  $\tau = 0$ , one can define medium as a purely fluid medium. The dynamics of chains formed inside cells are governed by the viscoelasticity of the surrounding microenvironment. The rheological behavior of cytoplasm can be described by the Maxwell and Voigt approximation. More details can be found in Ref. [38].

As already mentioned in Chapter 2.2, Dreyfus R. et al. [44] describe improvement related to the magnetic chaining technique (MCT). Using particles with sizes in the range of visible light, allowed them to use Bragg’s law of diffraction,  $d = k\lambda/n(1 + \cos \theta)$ , to measure the distance  $d$  between the particles. By increasing the intensity of the external magnetic field, the distance between the particles was observed to decrease due to the increase in attractive magnetic force. As a consequence, wavelength  $\lambda$  will also decrease causing a change in the sample color. Interparticle distance  $d$  is a result of mechanical equilibrium between repulsive and attractive forces.

Repulsive forces can result from electrostatic charge of the particle surface or from surface adsorbed polymers, or both. Attractive forces have their origins in the magnetic dipolar force, and depend on the strength of the applied external magnetic field. Short-range van der Waals forces can also contribute to attractive forces between the particles in the chain (these forces need to be considered for interparticle distance  $< 20$  nm). Analyzing the signal that is diffracted by the chain of particles, one can find the interparticle distance  $d$ . This method offers a very accurate and easy way to measure any kind of repulsive force between the magnetic particles [44].

Now, we will give a short review of different methods that consist of rotation of a sample cell with different angular frequency or application of fluid flow on the chain of particles formed in a static external magnetic field. In a low-Reynolds number regime microfluidic flow is usually dominated by laminar flow and the interaction between reagents is limited to diffusion. This process can be time-consuming for large molecules (biological and organic) with very low diffusivities. Capillary tubes filled with a suspension of paramagnetic particles can be submitted to a rotational motion which will create viscous drag force.

Applied external magnetic field can be fixed at certain values and capillary can rotate with different angular velocities. In these circumstances, chains will follow a fluid that rotates as a solid body. Vectors of magnetic moment in the chain will point in the magnetic field direction. Particles in capillary tubes will form chains in a magnetic field and from the length of the chains at a given angular velocity one can study the dynamics of the particles. Conditions at which it is no longer possible to create chains of paramagnetic particles yields a critical value for Mason number. Examining chain length while varying the viscosity of the liquid and rotation speed can be useful in biological and organic applications in order to find the best methods for passive and active mixing. Formation of paramagnetic chains in microfluidic devices has an influence on the viscosity of suspension. This is important for very sensitive biosensors. Also in this case chains can be used to boost mixing and to accelerate biochemical reactions. Probing different experimental conditions, one can find the optimal value of Mason number that will enhance mixing. This optimal value of Mason number should favor formation of the chain and suppress formation of other structures. Paramagnetic chains have larger surface areas and reaction site densities than other aggregated structures and clusters [54]. Colloidal chains might also serve as a model system for folding pathways. One of the interesting features of this system is the

possibility of using it for measuring phase lag in different systems due to the viscosity of the surrounding fluid.

### 2.3.2 Linear increase from small to large Mason Number

In the previous Chapter we describe the behavior of chains of paramagnetic particles in the so-called low-frequency regime. Now we will show what is happening with the 1D chains when they are in the so-called high-frequency regime, which appears above a critical value of Mason number. Above this value, chains are no longer stable and will break into smaller fragments, mostly doublets, which again can rotate with the same frequency as the frequency of the rotating magnetic field [25, 26, 29, 30].

Melle S. et al [17, 30] found that the crossover Mason number ( $Mn \sim 1$ ) does not generally depend on volume fraction, and that chain length will increase until a steady state is reached. In the rotating magnetic field there is competition between the hydrodynamic forces of the chain and magnetic dipolar interaction which will determine the final size of aggregates of paramagnetic particles. For longer chains, phase lag is greater than for shorter chains, which consequently shows that chain length i.e. size of aggregated particles decreases when Mason number is increased. The crossover Mason number marks the point at which the aggregation into chains in the rotating magnetic field is no longer possible. They measure dichroism that arises from optically anisotropic chains and thus give information about the number of aggregated particles. Measurement of the dichroism of the system shows existence of two different regions of frequency. The crossover frequency  $f_c$  defines the point between these two regimes. Below  $f_c$ , dichroism is not frequency dependent and remains almost constant; however above  $f_c$  systems show a very strong dependence on frequency and it will decrease with a power law with exponent -1. In this region one can find only a few short chains that are contributing to dichroism. This shows that the dipolar magnetic forces are surpassed by hydrodynamic friction forces. As a result, to decrease viscous drag force, chains break up. When the value of the Mason number exceeds 1 ( $Mn > 1$ ) chains that consist of two particles become unstable. As a consequence, the total number of aggregated particles will decrease with time [17, 30].

As previously mentioned, at the critical frequency  $f_c$  of magnetic field, chains will rotate asynchronously with the magnetic field and longer chains will break in to smaller chains (consisting of only two particles) which are still able to rotate synchronously with the field. One of the parameters that defines the value of the critical

frequency  $f_c$  is the viscous dissipation in the surrounding fluid, which as a consequence defines maximum elongation of the rotational paramagnetic chain. The longer the chains are, the critical frequency of the field that these chains can still follow is smaller. Sandre O. et al. [31] used liquid droplets instead of the solid particles with a predetermined size ratio. These liquid droplets were able to exchange matter between themselves. Using liquid droplets they were able to have prolate ellipsoid droplets that were able to rotate synchronously with the external magnetic fields up to the frequency of  $\Omega/2\pi < 10$  Hz (compared to experiments with solid paramagnetic particles, where chains break into smaller chains when the frequency of the external field is  $\Omega \leq 1$  Hz). Above the threshold frequency, droplets will break up and divide into droplets with smaller aspect ratio. These droplets will rotate synchronously with the external magnetic field. Hydrodynamic flow inside the rotating ellipsoids will reduce the viscous torque. Viscous torque is significant for a ratio of inner fluid to outer fluid  $\eta_i/\eta_0 < 10$  when ellipsoid eccentricity  $e = \sqrt{1 - (b/a)^2}$  is small. They also show that these small droplets, with increasing frequency of external field, become closer to each other and have a tendency to form a hexagonal network. These hexagonal networks are formed because of the dynamic repulsive interaction between the rotating droplets [31]. We use this feature of the system in our experiment with ferrofluid droplets in order to accomplish buckling motion of the chain.

One, very interesting class of tunable fluids, that show similar characteristics as MR fluids, are so-called inverse ferrofluids or magnetic holes. Magnetic holes represent micron-sized non-magnetizable particles dispersed in a ferrofluid. Varying the saturation magnetization and/or the strength of the magnetic field one can control mechanical properties of the ferrofluid. Different shape, size, and functionality of non-magnetizable particles contribute to the growing interest in and different application of inverse ferrofluids [37].

Similarly to MR fluids, non-magnetizable particles in ferrofluids will form chains of spheres when submitted to an external static magnetic field. When a rotating magnetic field is applied these chains will start to rotate. Depending on the frequency of the applied magnetic field, they can rotate synchronously or asynchronously with the field. Increasing the frequency of the magnetic field, chains of particles will rotate with a phase lag relative to the external magnetic field. Above a certain frequency the chain will break into smaller chains that still can follow rotation of the magnetic field. This frequency depends on the velocity and viscous drag that acts on the ends of the chain [55]. Helgesen et al. found for a pair of two spheres, which is the shortest possible

chain, two different behaviors depending on the way in which the spheres are connected. If the spheres are weakly bound (if the only force that acts between them is dipole-dipole interaction), during one period of rotation, particles can separate and rotate as individual spheres for a short period of time. If particles are bound by surface contact forces (in addition to dipolar forces) spheres are not able to separate and rotate as individual particles. In our experiment we also notice individual rotation of particles which can lead to conclusion that in our system dipole-dipole interaction between the particles is dominant. These doublets can rotate synchronously and nonsynchronously with respect to the frequency of rotating field. The motion in magnetic holes systems in an external rotating magnetic field can be described with an equation of motion similar to the equation for a damped pendulum under a constant torque. Varying the ratio between viscous and magnetic forces can lead to wide range of different behavior [52, 55].

For all above mentioned experiments, which utilise the same approach that we use, chains of particles (or spherical droplets) were submitted to an external magnetic field that can rotate with different frequencies. Competition between magnetic and viscous forces was observed. There is another approach that considers dynamics of paramagnetic chain of particles in a periodic channels.

Kang T. G. et al. [56] found that dynamics of paramagnetic chains of particles in periodic channels circumstantially depends on the Mason number, particle fraction and magnetic susceptibility. Above the critical Mason number chains will rotate as a rigid body and they found three different conformations depending on the value of the Mason number: 1) the system will prefer chains with branches rather than linear chains; 2) linear chains will tilt and break into two chains allowing slip zone between them and 3) shorter chains rotate in the channel. Behavior of the system at lower Mason number is guided by magnetic forces and at high Mason number by viscous forces. Magnetic permeability (difference between the particles and the fluid) and particle fraction can also have influence on the dynamics of magnetic particles. Although experiments that involves chains of paramagnetic particles in the rotational magnetic field and chains of paramagnetic particles suspended in capillary tubes and microfluidic channels in a static magnetic field are very similar there is one fundamental difference. The chains of particles that rotate due to an externally applied rotational magnetic field will rotate as propeller. This will consequently produce an interference effect between different chains. This effect does not exist in the experiments that involve simple shear flow [56].

### 2.3.3 Nonlinear increase from small to large Mason number

In Chapters 2.3.1 and 2.3.2 we discuss the behavior of the chain of the particles when the value of the Mason number is  $Mn < 1$  and  $Mn \sim 1$ . Also we show that in the case when  $Mn > 1$  the chains consist out two particles also start to dissolve in magnetic field and all aggregated structures disappear over the time. Now we will describe a brand new type of behavior, which was for the first time noticed and described during work on this thesis. This new feature of the system arises during a sudden switch from small to very large Mason number ( $Mn \gg 1$ ). For the large Mason number the frequency of the rotating magnetic field is so fast that even the doublets cannot longer follow the field rotation. Instead of breaking up, chains will start to curl from both ends (clockwise or anticlockwise depending on the phase difference between fields in x- and y-direction) toward the center of the chain collapsing to the rotating cluster. Before our experiment this behavior was only partially reported for chains that are made out of permanently linked particles (chains will form S- and U- shape structures, see Chapter 2.3.1). We also performed experiments with spherical ferrofluid droplets that also collapse to the cluster but via buckling motion toward the center. More details about these experiments can be found in Chapter 5.1.

# 3 Theoretical concepts and simulation methods

In this Chapter, we will give a short overview of important theoretical concepts, simulation methods and equations that are important for explaining the phenomena observed during the experimental work of this thesis. The idea for this chapter is to serve as a quick reminder of all the important equations and the way how to derive them. Also we will give the basics of magnetisms and relevant equations concerning magnetic dipole energy. This chapter is connected with Chapter 5 and it will serve as an extension of this chapter.

## 3.1 Magnetic properties of materials

Magnetic materials are classified, depending of their magnetic susceptibility  $\chi_m$  or relative permeability  $\mu_r$ , in three major classes:

Diamagnetic materials: are the class of materials for which magnetic susceptibility is  $\chi_m < 0$ . In this class of materials, the magnetic field due to electronic motion of orbiting and spinning completely cancel each other. Consequently, the permanent magnetic moment of each atom is zero and diamagnets are forced towards minima of magnetic field strength i.e. they are “squeezed out” from the magnetic fields. Most materials are weakly diamagnetic, with  $\chi_m$  on order of  $10^{-5}$  including water, copper, silicon, diamonds, proteins, DNA, polymers, glass etc.

Ferromagnetic materials such as iron, cobalt and nickel, which have relatively large magnetic moments,  $M \neq \chi_m H$  and are strongly attracted to magnetic fields.

Paramagnetic materials are the class of materials for which magnetic susceptibility is  $\chi_m > 0$ . They will align parallel to the magnetic field and experience a small force towards magnetic field maxima, i.e. they are attracted to magnetic fields. Paramagnetic materials include platinum, potassium, oxygen etc. A special case of paramagnetism, which is of great interest for us, is the so called superparamagnetism. Superparamagnetic particles have a small iron oxide core coated with a polymer shell. The particles will gain induce magnetic moment when subjected to a magnetic field.

This kind of particles, however, does not have magnetic memory and once the external field is removed, the particles redisperse and show Brownian motion [80, 81]. More about superparamagnetic particles used in our experiments can be found in Chapter 6.1.

## 3.2 Hydrodynamic equations and Reynolds number

When negatively charged paramagnetic particles are dispersed in the carrier fluid, they will experience random Brownian motion. By applying a static external magnetic field due to induce dipole moment, particles will organize into chains parallel to the magnetic field. The velocity of this chaining effect depends on the interplay between the thermal (Brownian) forces and the magnetic forces. When the external rotating field is applied to two or more particles, it will start to move in a viscous fluid. To fully describe and understand the dynamics of the system in these new conditions, we need to take into account one additional force called hydrodynamic interactions. Hydrodynamic interactions are long-range interactions and they are present only in the conditions when particles are moving. For the micrometer size particles, for which motion take place at low Reynolds number ( $10^{-3}$ - $10^{-5}$ ), where inertial forces can be neglected, the dynamics of the system is determined by hydrodynamic interactions. In this section, we will give a short overview of hydrodynamic equations, such as the Navier-Stokes equation, Stokes equation, and Reynolds number. More details can be found in Ref. [82, 83, 85, 87].

The continuity equation is the differential equation for the conservation of mass, which connects mass density  $\rho(\mathbf{r},t)$  of a fluid with flow field  $\mathbf{v}(\mathbf{r},t)$ .  $\mathbf{v}(\mathbf{r},t)$  is also known as Eulerian velocity. The continuity equation can be written as:

$$\frac{\partial \rho}{\partial t} + \nabla \cdot (\rho \mathbf{v}) = 0 \quad (3.1)$$

From this equation one can see that matter is neither destroyed nor created. This equation balances between the change of the mass in an arbitrary volume with time ( $\partial \rho / \partial t$ ) and the mass flux through the surface  $S$  of a determined volume  $V$  ( $\rho \mathbf{v}$ ). If possible, a change of the fluid density, both with time and space, are excluded i.e.  $\rho(\mathbf{r},t) = \rho$ . In that case, the continuity equation can be written as

$$\nabla \cdot \mathbf{v} = 0, \quad (3.2)$$

This equation shows that velocity field is solenoidal, and fluids that obey this equation i.e. all fluids for which  $\rho = \text{const.}$  are called incompressible fluids. Water is example of an incompressible fluid

Conservation of momentum for a Newtonian fluid can be expressed with a partial differential equation called the Navier–Stokes equation. Following Newton’s law of motion, the sum of the surface and body forces acting on the volume needs to be equal to the time rate of change of linear momentum inside the volume:

$$\int_{R(t)} \frac{\partial}{\partial t} (\rho \mathbf{v}) dV + \int_{S(t)} (\rho \mathbf{v}) \mathbf{v} \cdot \mathbf{n} dS = \int_{R(t)} \rho f dV + \int_{S(t)} \Sigma dS, \quad (3.3)$$

where the labels  $R(t)$  and  $S(t)$  (on the integral signs) indicate that the integrations are performed over the volume of the system and over its surface (following the Reynolds transport theorem). The first term on the left-hand side of the equation represents the time ratio of the change of the momentum in volume  $V$ , the second term on left side represent the flux of mass entering the volume  $V$  trough the bounding surface  $S$ . The first term on the right side represents the total body force acting over the volume  $V$  and is given by the volume integral  $F_B = \int_{R(t)} \rho f dV$ . The second term on the right side represents the total body force acting on an infinitesimally small element  $dS$  of the surface  $S$  and is given by the surface integral  $F_S = \int_{S(t)} \Sigma dS$ . This surface integral can be rewritten in terms of the stress tensor instead of the stress vector. In this case can be written as  $F_S = \int_S (\mathbf{n} \cdot \boldsymbol{\sigma}) dS$ . Applying the Gauss theorem, surface integral can be replaced by the volume integral  $F_S = \int_{R(t)} (\nabla \cdot \boldsymbol{\sigma}) dV$ . Equation (3.3) can be written as:

$$\int_{R(t)} \frac{\partial}{\partial t} (\rho \mathbf{v}) dV + \int_{S(t)} (\rho \mathbf{v}) \mathbf{v} \cdot \mathbf{n} dS = \int_{R(t)} \rho f dV + \int_{R(t)} (\nabla \cdot \boldsymbol{\sigma}) dV, \quad (3.4)$$

With help from the Gauss theorem, the flux integral can be transformed into a volume integral in tensor form (because  $(\rho \mathbf{v}) \mathbf{v}$  is a tensor). Now we can write the following equation:

$$\int_{R(t)} \left( \frac{\partial(\rho \mathbf{v})}{\partial t} + \nabla \cdot (\rho \mathbf{v} \mathbf{v}) - \rho \mathbf{f} - \nabla \cdot \boldsymbol{\sigma} \right) dV = 0, \quad (3.5)$$

The integrand is equal to zero because volume is arbitrary. Finally, the law of momentum conservation can be written as:

$$\frac{\partial(\rho \mathbf{v})}{\partial t} + \nabla \cdot (\rho \mathbf{v} \mathbf{v}) = \rho \mathbf{f} + \nabla \cdot \boldsymbol{\sigma}, \quad (3.6)$$

This form of the differential momentum equation is known as the conservative form and it is used to solve the governing equation in computational fluid dynamics as a starting point in many numerical algorithms. Another form of differential momentum equation can be obtained by expanding the divergence term and time derivative. This form is known as traditional form and can be written as:

$$\rho \left( \frac{\partial \mathbf{v}}{\partial t} + \mathbf{v} \nabla \cdot \mathbf{v} \right) + \mathbf{v} \left[ \frac{\partial \rho}{\partial t} + \mathbf{v} \nabla \rho + \rho \nabla \cdot \mathbf{v} \right] = \rho \mathbf{f} + \nabla \cdot \boldsymbol{\sigma}, \quad (3.7)$$

Since the mass over the volume  $V$  is conserved, the term in the square bracket is equal to zero so we obtain the differential momentum equation in the final form as:

$$\rho \left( \frac{\partial \mathbf{v}}{\partial t} + \mathbf{v} \nabla \cdot \mathbf{v} \right) = \rho \mathbf{f} + \nabla \cdot \boldsymbol{\sigma}, \quad (3.8)$$

To complete this equation we need to consider two types of contributions to the stress tensor  $\boldsymbol{\sigma}$ , i.e. we need to find the relation between the stress in the fluid and the state of the fluid. The first contribution comes from gradient in the hydrostatic pressure  $p$  (in the case of static fluid) and the force density can be written as  $-\nabla p$  or  $\nabla \cdot (-p \mathbf{1})$ , where  $\mathbf{1}$  is the unit tensor. The second contribution comes from the relative motion of neighboring fluid elements and from this motion viscous forces will arise. These forces will be linear in the case when velocity gradients are not large enough. They are linear in the first-order derivatives  $\nabla \mathbf{v}$  and  $\nabla \cdot \mathbf{v}$ .  $\nabla \mathbf{v}$  is a tensor gradient  $(\nabla \mathbf{v})_{\alpha\beta} = (\partial / \partial r_{\alpha}) v_{\beta}$ . In the case when fluid consists out of spherical particles i.e. when the fluid is isotropic we can write  $\nabla \mathbf{v} + (\nabla \mathbf{v})^T$ . Superscript T denotes the transpose of a

second-rank tensor. Combining these two contributions to the stress tensor we obtain the so-called Newtonian constitutive equation:

$$\boldsymbol{\sigma} = -p\mathbf{1} + \eta[\nabla\mathbf{v} + (\nabla\mathbf{v})^T], \quad (3.9)$$

Newtonian fluids are all fluids that can be described by this equation. Here  $\eta$  is dynamic viscosity and there exists a specific value for each material. Applying the substitution equation (3.9) to equation (3.8) we finally come to the expression for Navier-Stokes equation for incompressible fluid:

$$\rho \left( \frac{\partial\mathbf{v}}{\partial t} + \mathbf{v}\nabla \cdot \mathbf{v} \right) = -\nabla p + \eta\nabla^2\mathbf{v} + \rho\mathbf{f}, \quad (3.10)$$

$$\nabla \cdot \mathbf{v} = 0, \quad (3.11)$$

More detailed discussion on the derivation of Navier-Stokes equation can be found in Ref. [82, 83, 86].

For investigation of the fluid flow around small particle suspended in the viscous fluid one first needs to rescale variables in order to obtain the dimensionless Navier-Stokes equation. Particles suspended in a viscous fluid have a characteristic linear dimension  $a$  and they move at velocity  $u$ . In this way we can write rescaled variables as  $\mathbf{r}' = \mathbf{r}/a$  for dimension and  $\mathbf{v}' = \mathbf{v}/u$  for velocity. Now the Navier-Stokes equation can be written as:

$$\frac{\rho a^2}{\eta\tau} \frac{\partial\mathbf{v}'}{\partial t'} + Re(\mathbf{v}'\nabla')\mathbf{v}' = \nabla'^2\mathbf{v}' - \nabla'p' + \mathbf{f}', \quad (3.12)$$

where  $\mathbf{f}' = \mathbf{f}/(\eta u/a^2)$  is the rescaled force and  $p' = p/(\eta u/a)$  is the rescaled pressure. Time scale  $\tau$  is connected with the time  $\tau_m$  which is the time that a particle needs to lose initial momentum due to friction with the fluid. For most experiments with colloidal particles  $\tau_m$  scales from 1 to 100 ns (for particles up to  $1\mu\text{m}$ ). Time scale  $\tau$  scales from 1 ms to 1s. From this we can conclude that  $\tau \gg \tau_m$ .  $Re$  is the dimensionless factor known as the Reynolds number. Reynolds number is the measure

of the ratio between inertial forces  $\rho(\mathbf{v}\cdot\nabla)\mathbf{v}$  (they scales as  $\eta u^2/a$ ) and viscous forces  $\eta\nabla^2\mathbf{v}$  (they scales as  $\eta u/a^2$ ). Ratio  $\rho/\eta$  that enters into the dimensionless Navier-Stokes equation is known as kinematic viscosity  $\nu$ . Reynolds number is defined as:

$$R_e = \frac{\rho u a}{\eta}, \quad (3.13)$$

Navier-Stokes equations are nonlinear and as a consequence can be solved only for specific cases. One of the cases that we are interested in takes place at a very low Reynolds number ( $R_e \ll 1$ ). In this case, the term  $(\mathbf{v}\cdot\nabla)\mathbf{v}$  vanishes and we can write the following equation:

$$\rho \frac{\partial \mathbf{v}}{\partial t} = -\nabla p + \eta \nabla^2 \mathbf{v} + \rho \mathbf{f}, \quad (3.14)$$

For interactions that take place at a low Reynolds number, we can neglect the inertial term from the left side of the equation (3.14). In this case we can say that the system is in an over-damped regime and dynamics of the system can be described by the stationary Stokes equation. This equation is also known as the creeping-flow equation [82, 83]:

$$-\nabla p + \eta \nabla^2 \mathbf{v} + \rho \mathbf{f} = 0, \quad (3.15)$$

### 3.3 Magnetic dipole interaction

Paramagnetic particles will acquire induce dipole moment  $m$  when external magnetic field  $H$  is applied. The interaction energy between two particles with aligned dipole moments is given by following equation:

$$U_{mag}(r, \alpha) = \frac{m^2}{4\pi} \frac{(1 - 3\cos^2\alpha)}{r^3}, \quad (3.16)$$

where  $\alpha$  is the angle between the applied field and the line connecting centers of the spheres and  $r$  is the distance between sphere centers. The magnetic force acting between particles (which are approximated by a point dipole) includes two

components, radial  $\mathbf{F}^r$  and tangential  $\mathbf{F}^\theta$  component and is given by following equation:

$$\mathbf{F}_{mag} = \mathbf{F}^r + \mathbf{F}^\theta = \frac{3\mu_0 m^2}{4\pi r^4} (3\cos^2\alpha - 1) + \frac{3\mu_0 m^2}{4\pi r^4} \sin(2\alpha), \quad (3.17)$$

When particles are organized in to the chain that consist of  $2N+1$  particle (labeled from  $-N$  to  $N$ ), magnetic force acting on the  $i$ th is  $\mathbf{F}_i = F_i^r \mathbf{u}_r + F_i^\theta \mathbf{u}_\theta$ .

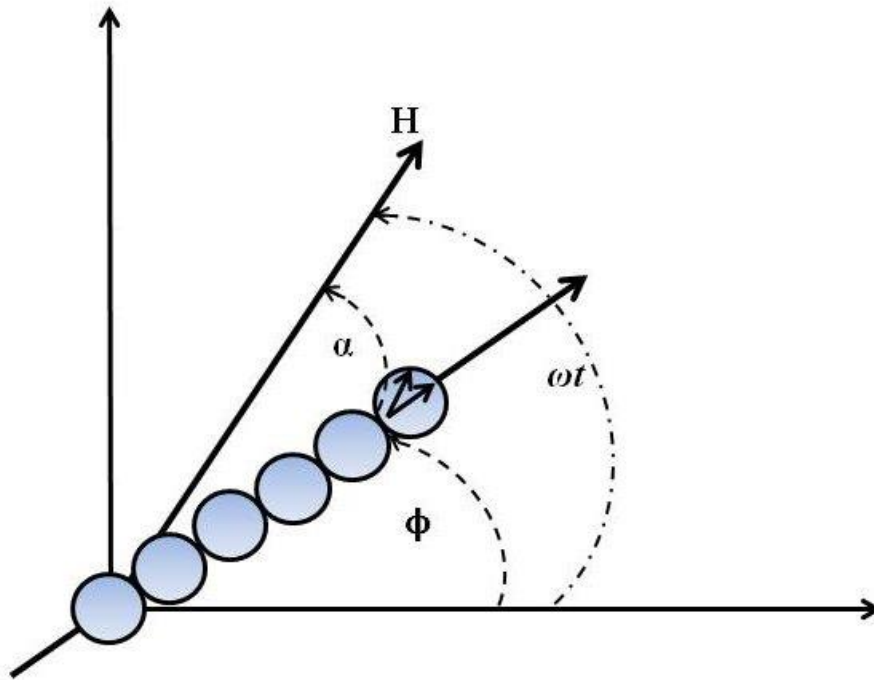


*Figure 3.1: Chain of paramagnetic particles in rotating magnetic field.*

When a magnetic field starts to rotate with angular velocity  $\omega$ , the dipole interaction generates a magnetic torque on the chain. Due to this torque, a chain of paramagnetic particles will start to rotate following the external magnetic field with the phase lag angle  $\alpha = \omega t - \theta$ . This rotation occurs due to magnetic torque  $\mathbf{\Gamma}_m$ , acting on the chain of  $N$  spherical magnetic particles and is given by:

$$\mathbf{\Gamma}_m = \mathbf{m} \times \mathbf{H} = \frac{3\mu_0 m^2}{4\pi} \frac{N^2}{2(2R)^3} \sin 2\alpha, \quad (3.18)$$

Magnetic torque is counterbalanced by thermal Brownian torque; the torque due to inertia; the elastic torque due to the ends of and the chain bending away from the center and the viscous drag torque. For the over-damped regime, in which the Reynolds number is low ( $\sim 10^{-4}$ ), the inertial torque may be neglected as well as chain-chain interactions. For the field used in our experiment viscous forces will dominate over thermal Brownian forces. The dynamics of the rotation of the paramagnetic chains can be understood from the interplay between magnetic, elastic and viscous torque. The viscous torque acting on the chain consists of  $N$  spherical particles and is given by equation:

$$\Gamma_v = \zeta_r \omega = \kappa V \eta \omega, \quad (3.19)$$

where  $\eta$  is viscosity of a medium,  $V = N(\frac{4}{3})\pi R^3$  and  $\kappa$  is the shape factor. For a linear chain consisting of  $N$  particles,  $\kappa$  is given by

$$\kappa = \frac{2N^2}{\ln(N/2)}, \quad (3.20)$$

For a given strength and frequency of the magnetic chain, at a steady angular velocity, for which two counteracting torques are in balance in the center of the chain, the phase lag angle is defined and can be calculated from following equation:

$$\sin(2\alpha) = \frac{32N\eta\omega}{\mu_0\chi^2 H_0^2 \ln(N/2)}, \quad (3.21)$$

The strength of the interaction between the magnetic field and the chain of particles can be characterized by using two characteristic dimensionless parameters, dipole strength  $\lambda$  and Mason number  $Mn$ , which are connected to each other by Péclet number  $Pe$ . Péclet number is given by the following formula:

$$Pe = \lambda Mn = \frac{32\pi\eta\omega R^3}{9k_B T}, \quad (3.22)$$

Since the magnetic particles are large comparing to the solvent particles, Brownian motion can be neglected, since the thermal forces, that are proportional to  $k_B T$ , are very small compared to the hydrodynamic and magnetic forces. Dipole strength  $\lambda$  shows the ratio of the maximum magnetic interaction energy between two particles aligned with the external magnetic field to the thermal energy:

$$\lambda = \frac{\pi\mu_0 R^3 \chi^2 H_0^2}{9k_B T}, \quad (3.23)$$

If the dipole strength  $\lambda$  is small, Brownian motion will dominate over the dipole interaction and chains of particles will not form. For  $\lambda$  large enough dipole interaction will dominate over the thermal (Brownian) motion which results in the formation of the chains. Thermal fluctuation of the chain becomes more significant as the length of the chain increases.

The second parameter that describes the interaction between magnetic particles and surrounding solvent is the so-called Mason number  $Mn$ . The Mason number shows the ratio of the magnetic force and viscous force (hydrodynamic force that can be estimated as Stokes drag):

$$Mn = \frac{32\eta\omega}{\mu_0 \chi^2 H_0^2}, \quad (3.24)$$

Equation (3.24) shows the most widely used equation for the Mason number. Since the Mason number is a very important parameter for the characterization of all experiments performed during the work presented in this thesis, in the following subchapter we will present more detailed derivation and different formulations and equations for the Mason number. Some of the recent experiment shows that some other forces (acid-base, van der Waals etc.) can also play an important role. But, in the case when these forces can be neglected, a system can be completely described by  $\phi$  (volume fraction),  $\lambda$  (dipole strength) and  $Mn$  (Mason number) [18, 25, 37].

### 3.4 Mason number $Mn$

In the Chapter 3.2 we have discussed and derived Navier –Stokes, Stokes equation and Reynolds number. In Chapter 3.3 we have discussed magnetic dipole energy as well as Péclet and Mason number. In this chapter we will the derive equation for the Mason number which is one of the most important parameters to define our experiment. In Chapter 3.2 we show, that for our experimental system, consisting of superparamagnetic colloidal particles, the Reynolds number is very small, on the order of  $10^{-4}$ - $10^{-5}$ . Due to this behavior, the system will be in an over damped regime with no inertial forces exerted on it. The parameter which describe properties of our system is the ratio between the hydrodynamic and magnetic force in a fluid so-called Mason number. The Mason number was for the first time introduced and defined by Gast A. P. and Zukoski C. F. [16] and later investigated and more detailed explained by several works performed by J. E. Matin and S. Melle. Some authors instead refer to the Mason number as the magnetoviscous number [31] which is an analogous name. The Mason number is a dimensionless parameter that compares this forces and can be smaller than 1, bigger than 1 or much larger than 1. Depending on the value of Mason number, a system will show three different types of behavior which has been discussed in more details in Chapter 2.3. Depending on the literature there are different denotation of the Mason number, such as  $Mn$  [27, 28],  $Ma$  [17], and  $\mathcal{M}$ . In this thesis we use the denotation  $Mn$ . The Mason number was first derived for ER suspensions and afterwards was also extended to MR suspensions. Here we will show the derivation only for the MR suspensions that we are interested in.

The Langevin equation is the governing equation of motion for paramagnetic particles and for motion of the  $i$  –th particle we can write,

$$m \frac{d^2 \mathbf{r}_i}{dt^2} = \mathbf{F}_i^b + \mathbf{F}_i^{wall} + \mathbf{F}_i^{ev} + \mathbf{F}_i^h + \mathbf{F}_i^m, \quad (3.25)$$

where  $m$  is the particle mass,  $\mathbf{r}_i$  the position of the  $i$ th particle,  $\mathbf{F}_i^b$  is the Brownian force,  $\mathbf{F}_i^{wall}$  the repulsive force, or the excluded-volume force between the particle and the wall  $\mathbf{F}_i^{ev}$  is excluded-volume force,  $\mathbf{F}_i^h$  is the hydrodynamic Stokes force,  $\mathbf{F}_i^m$  is the magnetic dipolar force. For an over damped regime, for low Reynolds number, inertial force can be neglected. For the reasons mentioned in the previous section, the

Brownian force can be also neglected. By assuming an infinite fluid in which magnetic particles exist, the repulsive forces between the particles and the wall can also be neglected. For this reasons we can write equation (3.25) as:

$$0 = \mathbf{F}_i^{ev} + \mathbf{F}_i^h + \mathbf{F}_i^m, \quad (3.26)$$

Excluded volume force  $\mathbf{F}_i^{ev}$  can be expressed by following equation:

$$\mathbf{F}_i^{ev} = A \frac{3\mu_0 m^2}{4\pi(2a)^2} \sum_{\substack{j=1, \\ j \neq i}}^N \widehat{\mathbf{r}}_{ij} \exp\left[-\xi \left(\frac{r_{ij}}{2a} - 1\right)\right], \quad (3.27)$$

where  $A$  and  $\xi$  are specified constant. For the purpose of the experiment  $A$  is set to be 2. For  $A=2$ , when two particles are in contact, and aligned along the direction of the field, interacting via a dipolar force, interaction force will be equal to zero. With  $n = 10$ , the distance between the particles will increase to  $r_{ij}/2a = 1.1$  when the ratio between the excluded volume forces and the dipolar force of two particles aligned with the field is  $\xi=10$ .

The excluded volume force is an important parameter for numerical simulation methods for preventing the overlapping between two neighboring particles. In the real space experiment this force can be excluded and the behavior of the system can be characterized by the ratio between viscous and magnetic force. The Stokes force on a sphere of radius  $a$  is  $\mathbf{F}_i^h = -\zeta(\mathbf{v}_i - \mathbf{v}_f)$ , where  $\mathbf{v}_i$  is the particle velocity,  $\mathbf{v}_f$  is the fluid velocity and assuming stick boundary conditions, the friction factor is  $\zeta = 6\pi\mu_0 a$ , with  $\mu_0$  the solvent viscosity. In steady shear the fluid velocity is  $\mathbf{v}_f = z\dot{\gamma}\hat{\mathbf{x}}$ .

The potential of interaction between two polarizable spherical particles  $i$  and  $j$ , in the point dipole approximation, is

$$V(r_{ij}) = -\alpha \left(\frac{d}{r_{ij}}\right)^3 (3\cos^2\theta_{ij} - 1), \quad (3.28)$$

$\theta_{ij}$  is an angle between center-to-center line of spheres  $i$  and  $j$  to the direction of the external magnetic field, with a center-to-center separation  $r_{ij}$ . Differentiating the above equation for potential one can find for the interaction force the following equation:

$$\mathbf{F}_i^m = -\frac{f_c}{2} \left( \frac{d}{r_{ij}} \right)^4 [(3c \cos^2 \theta_{ij} - 1) \widehat{\mathbf{r}}_{ij} + 2 \sin \theta_{ij} \widehat{\boldsymbol{\theta}}_{ij}], \quad (3.29)$$

where  $f_c = 3/2\pi \mu_0 \kappa_{\mu,c} a^2 \beta_\mu^2 H_0^2$  is the force at contact between two particles aligned with the field. From this equation follows that the radial component is attractive only when  $\theta \geq 54.7^\circ$ .  $\beta_\mu$  is the magnetic contrast factor or coupling parameter  $\beta_\mu = (\kappa_{\mu,p} - \kappa_{\mu,c}) / (\kappa_{\mu,p} + 2\kappa_{\mu,c})$ , where  $\kappa_{\mu,c}$  is the relative permeability (to the vacuum) of the continuous (liquid) phase,  $\kappa_{\mu,p}$  is the relative permeability of the particles, and  $\mu_0 = 4\pi * 10^{-7}$  H/m is the permeability of vacuum. Magnetic contrast factor  $\beta_\mu$  can be used as a parameter to define the type of MR fluids. For conventional (strong) MR fluids, the value for inverse ferrofluids (weak MR fluids) is  $0 < \beta_\mu < 1$  and for inverse ferrofluids (weak MR fluids) is  $-0.5 < \beta_\mu < 0$ . Derivation from non-dimensional Langevin equation, with respect to the distance and time, one can find a non-dimensional time  $\tau$ :

$$\tau = \frac{12^2 \eta}{\eta_0 \eta_s M^2}, \quad (3.30)$$

Multiplying  $\tau$  by the angular frequency of the external magnetic field  $\omega$  will give equation for Mason number:

$$Mn = \tau \omega = \frac{12^2 \eta \omega}{\eta_0 M^2}, \quad (3.31)$$

where  $M$  is the magnetization of the paramagnetic particles. James E. Martin [28] offered a different way to derive the Mason number from the non-dimensional Langevin equation. We will give here only the final step of this derivation. For steady shear, coupled Langevin equations can be expressed in terms of the dimensionless variables,

$$\frac{\partial \mathbf{r}'_i}{\partial t'_i} = 32Mn z'_i \hat{\mathbf{x}} + \sum_{j \neq i} \mathbf{f}_{hs}(r'_{ij}) + \sum_{j \neq i} \mathbf{f}_d(r'_{ij}) + \mathbf{f}_{bound}(z'_i) + J' \mathbf{R}_{\tau/\tau_1} \quad (3.32)$$

The Mason number is defined as  $Mn = \eta_0 \dot{\gamma} / 2 \mu_0 \kappa_{\mu,c} \beta_{\mu}^2 H_0^2$  for a suspension of magnetic particles. Normalization has been done in a way such that the particle diameter is unity,  $r' = \frac{r}{d}$ , and the time variable  $t' = \frac{t}{\tau_1}$  is normalized by the characteristic time  $\tau_1 = 32Mn/\dot{\gamma}$ . In this way characteristic time  $\tau_1$  is independent of particle size [28, 34, 37, 46].

From the definition of the Mason number one can find some very useful parameters. Melle et al. [46] find critical value of Mason number and thus they can predict critical length and mechanical stability of a dipolar chain. Concerning the behavior of particles in the chain, two time scales can be considered. Interplay between these times will define the behavior of the system. Time  $\tau$  can be considered as the time that is necessarily for one particle to move under the influence of another polarizable particle. Second time is the time  $\omega^{-1}$  that can be defined as the shearing time for a particle moving with angular frequency  $\omega$ . In the case when  $\tau > \omega^{-1}$  (which response to  $Mn > 1$ ) no stable chain will be formed [46].

### 3.5 Motion between particles in the fluid and simulation methods

When two spherical particles move toward each other, each of these particles will generate a velocity field, which will be transmitted through the fluid between them, and it will influence their motion. Thus the motion between them will be retarded. Also the fluid between the particles needs to be removed. There are two types of motion relative to the axes that connect the centers of these two spheres. Fluid can be squeezed out from the gap between two spheres or it can be sheared by rotation of the spheres. In the experimental work that is presented in Chapter 5.1 we use two types of simulation methods that depend on the separation between the particles. Numerical simulations have been performed by Steffen Schreiber and Prof. Dr. Walter Zimmermann from the University of Bayreuth. The first method is the method of reflection, which can be used for widely separated particles. This method uses the method of hydrodynamic interactions between point-like particles in the Rotne-Prager approximation. Rotne-

Prager approximation has been used in order to simulate the buckling motion of the particles in the chain. Second method is the fluid particle dynamics (FPD) method, for which the flow in the gap region between two particles is dominant, where the particles are treated as a part of the liquid of much larger viscosity for which the lubrication theory can be applied. This method has been used in order to simulate the curling motion of the particles in the chain. In the next chapters we will give a short overview of these methods and point to their importance in our work [21, 23, 82, 83, 88].

### 3.5.1 Method of reflection: the Rotne-Prager approximation

Method of reflection is an asymptotic method that can be used for the particles of arbitrary shape when they are widely separated (large  $R/a$ , where  $a$  particle size and  $R$  is particle-particle separation). Before we proceed with the Rotne-Prager approximation we will shortly define an expression for the stick boundary condition and Faxén theorems. The translational velocity  $\mathbf{v}_i$  and the angular velocity  $\boldsymbol{\Omega}_i$  of the  $i^{\text{th}}$  Brownian particles are related to the fluid flow velocity  $\mathbf{u}(\mathbf{r})$  for position  $\mathbf{r}$  on the surface of this particle by following equation:

$$\mathbf{u}(\mathbf{r}) = \mathbf{v}_i + \boldsymbol{\Omega}_i \times (\mathbf{r} - \mathbf{r}_i), \quad \mathbf{r} \in \partial V_i \quad (3.33)$$

where  $\partial V_i$  is the surface of the  $i^{\text{th}}$  Brownian particle and  $\mathbf{r}_i$  is the geometrical center of the  $i^{\text{th}}$  Brownian particle (position coordinate). Using the Green's function representation of the creeping flow equation for a multi sphere problem and making a summation of the integrals over the surface  $\partial V_j$ ,  $j = 1, \dots, N$  of the  $N$  spherical Brownian particles we can write

$$\mathbf{u}(\mathbf{r}) = \sum_{j=1}^N \oint_{\partial V_j} dS' \mathbf{T}(\mathbf{r} - \mathbf{r}') \mathbf{f}_j(\mathbf{r}'), \quad (3.34)$$

where matrix  $\mathbf{T}(\mathbf{r} - \mathbf{r}')$  is Oseen matrix, which connects a point force at a point  $\mathbf{r}'$  to the resulting fluid flow at a point  $\mathbf{r}$  and  $\mathbf{f}_j$  is the force per unit area exerted by surface element of Brownian particle  $j$  on the fluid. These two equations (3.33 and 3.34), for

the stick boundary conditions, must coincide with position  $\mathbf{r}$  on surface of the  $i^{\text{th}}$  Brownian particle. Combining 1 and 2 we obtain following equation

$$\mathbf{v}_i + \boldsymbol{\Omega}_i \times (\mathbf{r} - \mathbf{r}_i) = \sum_{j=1}^N \oint_{\partial V_j} dS' \mathbf{T}(\mathbf{r} - \mathbf{r}') \mathbf{f}_j(\mathbf{r}'), \quad \mathbf{r} \in \partial V_i, \quad (3.35)$$

For a single sphere ( $N=1$ ), Faxén's theorems can be derived from equation (3.35) by adding on the right hand-side the homogeneous solution  $\mathbf{u}_0(\mathbf{r})$  of the creeping flow equation:

$$\mathbf{v}_p + \boldsymbol{\Omega}_p \times (\mathbf{r} - \mathbf{r}_p) = \mathbf{u}_0(\mathbf{r}) + \oint_{\partial V} dS' \mathbf{T}(\mathbf{r} - \mathbf{r}') \mathbf{f}_j(\mathbf{r}'), \quad \mathbf{r} \in \partial V, \quad (3.36)$$

where  $\boldsymbol{\Omega}_p$  is rotational velocity,  $\mathbf{v}_p$  is translational velocity and  $\partial V$  is the surface of the sphere with its center at the  $\mathbf{r}_p$  and  $\mathbf{f}$  is the force per unit area exerted by the surface element of the sphere on the fluid after sphere was immersed in the fluid flow velocity field  $\mathbf{u}_0$ . Further transformation of the equation (3.36) (one can find more details in Ref. [88]) leads to the Faxén's theorems for translational motion as following:

$$\mathbf{v}_p = -\frac{1}{6\pi\eta_0 a} \mathbf{F}_p^h + \mathbf{u}_0(\mathbf{r}_p) + \frac{1}{6} a^2 \nabla_p^2 \mathbf{u}_0(\mathbf{r}_p), \quad (3.37)$$

where  $\mu^t = 1/6\pi\eta_0 a$ . Alternatively we can write (using notation from Ref. [83]):

$$\mathbf{v}_p = \mu^t \mathbf{F}_p + \mathcal{L}_F^t \mathbf{u}(\mathbf{r})|_{\mathbf{r}=\mathbf{r}_p} \quad \text{with} \quad \mathcal{L}_F^t = 1 + \frac{1}{6} a^2 \nabla^2, \quad (3.38)$$

If  $\mathbf{u}_0(\mathbf{r}) \equiv 0$  (or  $\mathbf{u} = 0$ ) we can obtain from equations (3.37) and (3.38) the well known Stokes friction law for translation.

From equation (3.36) one can derive (one can find more details in Ref. [88]) the Faxén's theorems for rotational motion as following:

$$\boldsymbol{\Omega}_p = -\frac{1}{8\pi\eta_0 a^3} \mathcal{J}_p^h + \frac{1}{2} \nabla_p \times \mathbf{u}_0(\mathbf{r}_p), \quad (3.39)$$

where  $\mu^r = 1/8\pi\eta_0 a^3$ . Alternatively we can write (using notation from Ref. [83]):

$$\boldsymbol{\omega}_p = \mu^r \mathbf{T}_p + \mathcal{L}_F^t \mathbf{u}(\mathbf{r})|_{r=r_p} \quad \text{with} \quad \mathcal{L}_F^t = \frac{1}{2} \nabla \times, \quad (3.40)$$

where  $\nabla \times$  represent tensor-like operator. The main idea that stands behind the method of reflection is based on the following assumptions: the ambient field that surrounds each particle consists of the original ambient field plus the disturbance field produced by another particle (or particles). Each correction of ambient field around exact particle will produce a new disturbance solution for that particle, which as a consequence changes the ambient field around another particle (or particles). The method of reflection is an iterative method, where each next iterative step will reduce the error i.e. level of accuracy increases with each step of iteration [82]. If we now consider particle  $i$  subjected to the external force  $\mathbf{F}_i$  and torque  $\mathbf{T}_i$ . In the zeroth order particle will move with velocity

$$\mathbf{v}_i^0 = \mu^t \mathbf{F}_i \quad \text{and} \quad \boldsymbol{\omega}_i^0 = \mu^r \mathbf{T}_i, \quad (3.41)$$

This motion will create a flow field  $\mathbf{u}^0(\mathbf{r})$  which will influence the motion of the neighboring particle  $j$ .  $\mathbf{u}^0(\mathbf{r})$  represent the fluid velocity field of sphere  $i$  in the absence of other particles i.e. in this case particle  $j$ . Now, following equation (3.38) and (3.40) velocities caused by flow field  $\mathbf{u}_0(\mathbf{r})$  we can write as following:

$$\mathbf{v}_j^1 = \mu^t \mathbf{F}_j + \mathcal{L}_F^t \mathbf{u}^0(\mathbf{r})|_{r=r_j}, \quad (3.42)$$

$$\boldsymbol{\omega}_j^1 = \mu^r \mathbf{T}_j + \mathcal{L}_F^t \mathbf{u}^0(\mathbf{r})|_{r=r_j}, \quad (3.43)$$

This motion will produce an additional flow field  $\mathbf{u}^1(\mathbf{r})$ . As aforementioned, the method of reflection is an iterative method and thus flow field is the result of a series of an expansion representation of the flow field  $\mathbf{u}(\mathbf{r})$  in powers of  $a/r_{ij}$ , where  $r_{ij}$  is the distance between the spheres. Thus we can write following equation:

$$\mathbf{u}(\mathbf{r}) = \mathbf{u}^0(\mathbf{r}) + \mathbf{u}^1(\mathbf{r}) + \mathbf{u}^2(\mathbf{r}) + \dots, \quad (3.44)$$

Each field  $\mathbf{u}^n(\mathbf{r})$  will satisfy the creeping flow equation. The calculation of the flow field  $\mathbf{u}(\mathbf{r})$  is solved by repeating the iterative procedure indefinitely, where convergence of resulting series expansion is assumed. Now following the Faxén's theorem as functions of the distance between two spheres we can obtain translational velocities as following:

$$v_i = v_i^0 + v_i^2 + v_i^4 + \dots \quad \text{and} \quad v_j = v_j^1 + v_j^3 + v_j^5 + \dots, \quad (3.45)$$

Following the same procedure for angular velocity we can write:

$$\omega_i = \omega_i^0 + \omega_i^2 + \omega_i^4 + \dots \quad \text{and} \quad \omega_j = \omega_j^1 + \omega_j^3 + \omega_j^5 + \dots, \quad (3.46)$$

The above presentation can be applied to the interaction between two spheres. If there are more than two particles in the system, we need to take into account interactions between all the particles which, as a consequence, leads to many-body interactions [83, 88].

The first step in an iterative process gives an expression for the mobilities that are exact up to the order  $(a/r_{ij})^3$ . This first step is known as the Rotne-Prager approximation:

$$\boldsymbol{\mu}_{ii}^{tt} = \mu^t \mathbf{1} + O(4), \quad (3.47a)$$

$$\boldsymbol{\mu}_{ij}^{tt} = \mu^t \left[ \frac{3}{4} \frac{a}{r_{ij}} (\mathbf{1} + \hat{\mathbf{r}}_{ij} \hat{\mathbf{r}}_{ij}) + \frac{1}{2} \left( \frac{a}{r_{ij}} \right)^3 (\mathbf{1} - 3\hat{\mathbf{r}}_{ij} \hat{\mathbf{r}}_{ij}) \right] + O(4), \quad (3.47b)$$

$$\boldsymbol{\mu}_{ii}^{rr} = \mu^r \mathbf{1} + O(4), \quad (3.47c)$$

$$\boldsymbol{\mu}_{ij}^{rr} = -\mu^r \frac{1}{2} \left( \frac{a}{r_{ij}} \right)^3 (\mathbf{1} - 3\hat{\mathbf{r}}_{ij} \hat{\mathbf{r}}_{ij}) + O(6), \quad (3.47d)$$

$$\boldsymbol{\mu}_{ii}^{tr} = 0 + O(7), \quad (3.47e)$$

$$\boldsymbol{\mu}_{ij}^{tr} = \mu_r a \left( \frac{a}{r_{ij}} \right)^2 \hat{\mathbf{r}}_{ij} \times + O(5), \quad (3.47e)$$

The above presented values are taken from Ref. [83, 84] (where one also can find more details). Here  $O(n)$  denotes correction of order  $(a/r_{ij})^n$ . Strictly speaking only the translational part (equations 3.47a and 3.47b) is referred to as the Rotne-Prager tensor (also known as Yamakawa tensor). But when we consider mobility in an Rotne-Prager approximation we mean on the whole equation 3.47a-3.47f. More information about Rotne-Prager tensors and a variational principle that minimizes energy dissipation which is originally used to derive the Rotne-Prager tensor can be found in Ref. [23].

### 3.5.2 Lubrication theory, shearing, squeezing and the fluid particle dynamics (FPD) method

As particle separation becomes smaller and smaller, the number of reflections of the higher order, necessary to describe the system, increases in order to get more accurate results for the hydrodynamic interaction. Thus the method of reflection is no longer feasible for the distances small or close to contact between two particles. To

describe the dynamics of two neighboring particles in relative motion, one can use so-called lubrication theory. In general there are two different type of relative motion that particles can perform, and thus generate the lubrication zone. A lubrication zone represents the gap between two particles in which strong velocity gradients exists. One is “shearing” motion (Figure 3.2 a)) and the other is “squeezing” motion (Figure 3.2 b)). Leading order terms in the lubrication equation for forces and torques are singular and depend on the small parameter  $\varepsilon$ , where  $\varepsilon = r_{ij}/a - 2 \ll 1$ , is the dimensionless gap parameter. From lubrication equation one can find that for “shearing” motion, were surfaces past each other by sliding motion, the leading-order term of the hydrodynamic friction coefficient is  $O(\ln \varepsilon^{-1})$  and for the “squeezing” motion, where the two rigid surfaces (particles) approach to each other along their line of centers, the leading-order term of the hydrodynamic friction coefficient is  $O(\varepsilon^{-1})$ , when  $\varepsilon \rightarrow 0$  [82, 83].

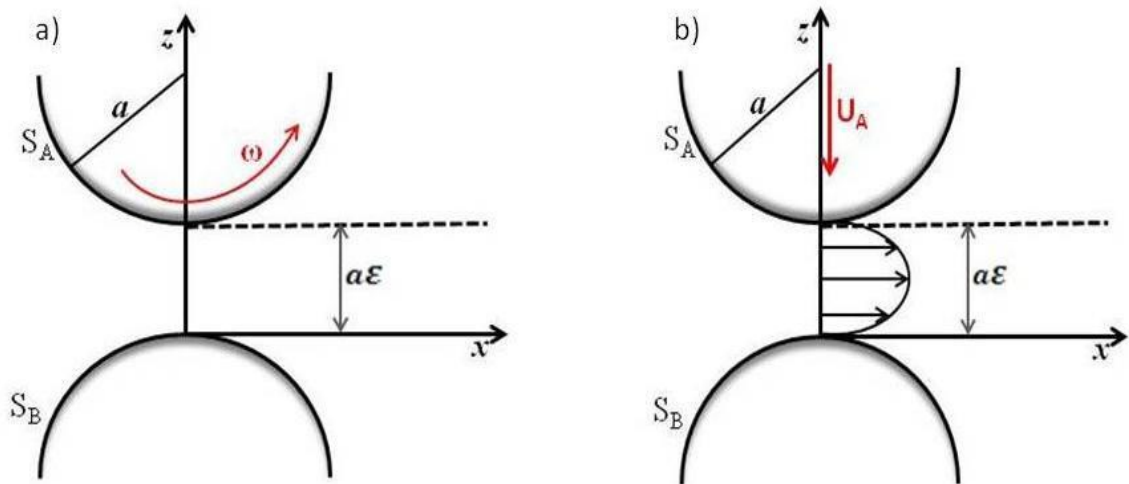


**Figure 3.2:** Scheme of the shear (a)) and the squeeze (b)) flow of two spheres of the same radius  $a$ . Here  $\varepsilon$  is the dimensionless gap parameter. This scheme has been redrawn from Ref. [82].

In Brownian dynamic simulations (and other simulation methods) colloidal suspensions are normally treated as a mixture of solid particles and a simple liquid. This approach can be very complicated and accompanied with singularity problems when squeezed flow is concerned. Tanaka H. and Araki T. demonstrate a new simulation method in which colloidal suspensions are treated as a mixture of viscous

undefomable fluid particles and nonviscous simple liquids. They named this model “fluid particle dynamics” (FPD) method. In this method they combine a lattice simulation for continuous fields and off-lattice simulation for particles. Colloidal mixture, in this method, was treated as a completely immiscible fluid mixture. When the ratio between  $\eta_c$  which is viscosity of particle (particle is undeformable, but viscous) and  $\eta_s$  which is viscosity of fluid component is equal to infinity i.e.  $\eta_c/\eta_s = \infty$  fluid particles can be regarded as solid ones. They define viscosity ratio  $R$  as  $R = \eta_c/\eta_s$  which is the measure of accuracy of the simulation method. For concentration field, the following equation can be written:

$$\phi_i(r) = [\tan h\{(a - |\mathbf{r} - \mathbf{r}_i|)/\xi\} + 1]/2, \quad (3.48)$$

where  $\mathbf{r}$  is the position for on-lattice site,  $\mathbf{r}_i$  is the off-lattice position of particles  $i$ ,  $a$  is the radius of the particles and  $\xi$  is the interface thickness. In this method complicated singularity problems associated with the squeezed flow are avoided due to the finiteness of  $\eta_c$ . FPD method can be used for colloidal particles of arbitrary shape. In our work we used lubrication theory and FPD method in order to simulate curling motion of the paramagnetic chain of particles [21].

## 3.6 Overdamped sine-Gordon and double sine-Gordon equation

In this chapter we will present basic equations that can explain the behavior of ribbons for different frequencies and eccentricity of a magnetic field. The equations that have been derived here are a part of simulation methods used to explain the behavior of ribbons presented in more details in section 5.2. Mathematical calculation and numerical simulations has been performed by Franz Mertens from the University of Bayreuth and Niurka R. Quintero and Renato Alvarez-Nodarse from the University of Seville, Spain. Their work was based on the following peer reviews [89-98], where one can find more details.

We are interested to explain different behaviors of the system depending on the frequency  $\omega$ . For this purpose we will first write partial differential equation for a certain potential function  $V$  and for a sufficiently large  $\omega$ ,

$$\frac{\partial^2 \phi}{\partial t^2} - \frac{\partial^2 \phi}{\partial x^2} + V'(\phi) = f - \gamma \frac{\partial \phi}{\partial t} + \epsilon_1 A(\phi) \cos \omega t + \epsilon_2 B(\phi) \sin \omega t, \quad (3.49)$$

where  $V(\phi)$  is normalized external potential,  $f$  is constant contribution of the driving force,  $\gamma$  is the normalized dissipative (damping) coefficient,  $A$  and  $B$  are normalized amplitudes of the periodic force and  $\omega$  is normalized frequency of the periodic force. Coefficients  $\epsilon_1$  and  $\epsilon_2$  will be explained latter. Now we want to transform this equation into the equation in which the driving force changes by an effective potential independent of time  $t$ . To do this we first need to discretize equation (3.49) [equation above] in  $x$  in the interval  $[0, L]$  where  $L$  is sufficiently large. We take the lattice  $x_n := x(n) := Ln/N$ ,  $n=0, 1, \dots, N$  and we let  $\phi_n(t) := \phi(x_n, t)$ ,  $K = (N/L)^2$ . Now we can write equation (3.49) in the following form

$$\frac{\partial^2 \phi}{\partial t^2} - \Delta_n \phi_n + V'(\phi) = f - \gamma \frac{\partial \phi}{\partial t} + \epsilon_1 A(\phi) \cos \omega t + \epsilon_2 B(\phi) \sin \omega t, \quad (3.50)$$

where  $\Delta_n \phi_n = K(\phi_{n+1} - 2\phi_n + \phi_{n-1})$  is the discrete one-dimensional Laplace function Here  $K$  represents coupling between particles in the chain.

Now following idea of Kapitza and Kivshar [90-93, 114, 115] we will split the function  $\phi_n(t)$  into two components. The first component is a slowly varying component  $\Phi_n(t)$  and the second component is a fast varying component  $\zeta_n(t)$ . With the help of these two components we can describe the slow and fast evolution. The function  $\zeta_n(t)$  has zero mean value and describes the small (and fast) oscillation around slowly varying function  $\Phi_n(t)$ . If we write that  $\phi_n(t) = \Phi_n(t) + \zeta_n(t)$  and assuming that  $\zeta_n$  is small enough and using Taylor series, we can rewrite equation (3.50) as following

$$\begin{aligned} & -\Delta_n \Phi_n - \Delta_n \zeta_n + V'(\Phi_n) + V''(\Phi_n) \zeta_n + V'''(\Phi_n) \frac{\zeta_n^2}{2} + \dots \\ & = f - \gamma \frac{\partial \Phi_n}{\partial t} - \gamma \frac{\partial \zeta_n}{\partial t} + \epsilon_1 (A(\Phi_n) + A'(\Phi_n) \zeta_n \\ & + \dots) \cos \omega t + \epsilon_2 (B(\Phi_n) + B'(\Phi_n) \zeta_n + \dots) \sin \omega t \end{aligned} \quad (3.51)$$

### 3 Theoretical concepts and simulation methods

---

If we again collect the leading fast varying terms in  $\zeta_n$  and if we assume that  $\Delta_n \zeta_n = 0$  and if we put that  $\omega_0^2 = V''(\Phi_n)$  we can write following equation

$$\gamma \frac{\partial \zeta_n}{\partial t} + \omega_0^2 \zeta_n = \epsilon_1 A(\Phi_n) \cos \omega t + \epsilon_2 B(\Phi_n) \sin \omega t$$

where  $\omega_0$  is eigen frequency. After transient time  $t \gg \gamma/\omega_0^2$  we get the solution to the equation (above eq.) as following

$$\zeta_n(t) = \epsilon_1 A \frac{\omega \gamma \sin(\omega t) + \omega_0^2 \cos(\omega t)}{\omega^2 \gamma^2 + \omega_0^2} - \epsilon_2 B \frac{\omega \gamma \cos(\omega t) - \omega_0^2 \sin(\omega t)}{\omega^2 \gamma^2 + \omega_0^2} \quad (3.52)$$

If we input equation (3.51) into (3.52) and take the average  $\langle \cdot \rangle := 1/T \int_0^T dT$ ,  $T = 2\pi/\omega$  we can obtain following effective equation

$$\begin{aligned} \gamma \frac{\partial \zeta_n}{\partial t} - \Delta_n \Phi_n + V'(\Phi_n) + \frac{\epsilon_1^2 A^2(\Phi_n) + \epsilon_2^2 B^2(\Phi_n)}{4(\omega_0^4 + \omega^2 \gamma^2)} V''''(\Phi_n) \\ = f + \epsilon_1 A'(\Phi_n) \frac{\epsilon_1 A(\Phi_n) \omega_0^2 - \epsilon_2 B(\Phi_n) \gamma \omega}{2(\omega_0^4 + \omega^2 \gamma^2)} \\ + \epsilon_2 B'(\Phi_n) \frac{\epsilon_1 A(\Phi_n) \gamma \omega + \epsilon_2 B(\Phi_n) \omega_0^2}{2(\omega_0^4 + \omega^2 \gamma^2)}, \end{aligned} \quad (3.53)$$

If we compare equation (3.51) and (3.53) we can write following expressions

$$\langle V''(\Phi_n) \zeta_n \rangle = 0, \quad \langle \zeta_n^2 \rangle = \frac{\epsilon_1^2 A^2(\Phi_n) + \epsilon_2^2 B^2(\Phi_n)}{2(\omega_0^4 + \omega^2 \gamma^2)},$$

$$\langle \zeta_n \cos(\omega t) \rangle = \frac{\epsilon_1 A(\Phi_n) \omega_0^2 - \epsilon_2 B(\Phi_n) \gamma \omega}{2(\omega_0^4 + \omega^2 \gamma^2)},$$

$$\langle \zeta_n \sin(\omega t) \rangle = \frac{\epsilon_1 A(\Phi_n) \gamma \omega + \epsilon_2 B(\Phi_n) \omega_0^2}{2(\omega_0^4 + \omega^2 \gamma^2)},$$

If we choose for potential following expression  $V(\phi) = (1 - \epsilon_3)(1 - \cos \phi) + |\sin(\phi/2)|$ ,  $A = \sin \phi$ ,  $B = -\cos \phi$ , and assuming that  $\psi = 2\phi$ ,  $\tau = 4t$ ,  $y = 2x$ ,  $\omega = \Omega/2$  we can write equation (3.50) as follows

$$\begin{aligned} \frac{\partial \psi}{\partial \tau} - \frac{\partial^2 \psi}{\partial y^2} + \left| \sin \frac{\psi}{2} \right|' \\ = \epsilon_1 \sin \psi \cos \omega t + \epsilon_3 \sin \psi - \epsilon_2 \cos \psi \sin \omega t - \gamma \frac{\partial \psi}{\partial \tau}, \end{aligned} \quad (3.54)$$

If we choose now that  $f = 0$  and we take for  $\epsilon_1 = \tilde{h}_+^2 + \tilde{h}_-^2$ ,  $\epsilon_2 = \tilde{h}_+^2 - \tilde{h}_-^2$  and for  $\epsilon_3 = 2\tilde{h}_+ \tilde{h}_-$ , where  $\tilde{h}_+$  and  $\tilde{h}_-$  are rescaled left and right circularly polarized magnetic field amplitudes we can write following expression

$$\begin{aligned} \frac{\partial \psi}{\partial \tau} - \frac{\partial^2 \psi}{\partial y^2} + \left| \sin \frac{\psi}{2} \right|' \\ = \tilde{h}_+^2 + \tilde{h}_-^2 \sin \psi \cos \omega t + 2\tilde{h}_+ \tilde{h}_- \sin \psi - \tilde{h}_+^2 \\ - \tilde{h}_-^2 \cos \psi \sin \omega t - \gamma \frac{\partial \psi}{\partial \tau}, \end{aligned} \quad (3.55)$$

From this equation we obtain the following expression for effective potential

$$V_{eff} = 2\tilde{h}_+ \tilde{h}_- \cos \psi + \left| \sin \frac{\psi}{2} \right| - \frac{\tilde{h}_+^2 \tilde{h}_-^2}{2\omega^2} \cos 2\psi, \quad (3.56)$$

If we now take for  $\psi/2 = \phi_b$ ,  $\omega = \Omega/2$ , and  $h_{\pm} = \sqrt{\Delta \chi} \tilde{h}_{\pm}$  we obtain the same equation as equation 5.11

$$V_{eff}(\phi_b) = 2\Delta\chi h_+ h_- \cos 2\phi_b + |\sin \phi_b| - 2 \frac{\Delta\chi^2 h_+^2 h_-^2}{\Omega^2} \cos 4\phi_b, \quad (3.57)$$

Using this equation we can explain the different behavior of our system depending on the following conditions:

- A)** If  $\Omega \gg 1$  and  $2\Delta\chi h_+ h_- \gg 1$  first term in equation (3.57) will dominate i.e.  $V_{eff}(\phi_b) = 2\Delta\chi h_+ h_- \cos 2\phi_b$  and the minima of potential energy will appear at  $\pi/2, 3\pi/2$ . That means that the  $\pi$ -kink will connect two standing positions of the ribbon. In Figure 5.2.3 (Chapter 5.2) this region is represented on the bottom of the graph for field frequency of  $\nu = 30$  Hz i.e.  $\omega/2\pi = \Omega = 30$  Hz

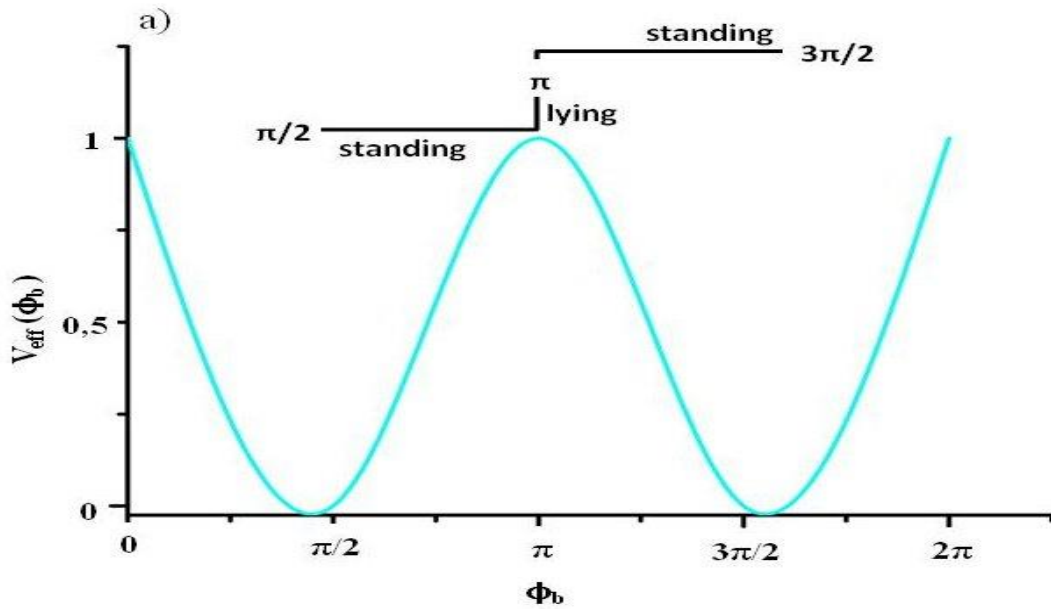


*Figure 3.3: here we show the dependence of effective potential for condition show in A). The kink will connect two standing positions. The small scheme above shows a characteristic kink profile.*

- B)** When the prefactor in the last term dominates i.e.  $2\Delta\chi h_+ h_- \gg \Omega^2$  i.e.  $V_{eff}(\phi_b) \approx -\cos 4\phi_b$ , the minima of the potentials are in  $0, \pi/2, \pi$  etc. and we can obtain  $\pi/2$ -kinks. In Figure 5.2.3 (Chapter 5.2) this region is represented in the middle of the graph for field frequency of  $\nu = 20$  Hz i.e.  $\omega/2\pi = \Omega = 20$  Hz.

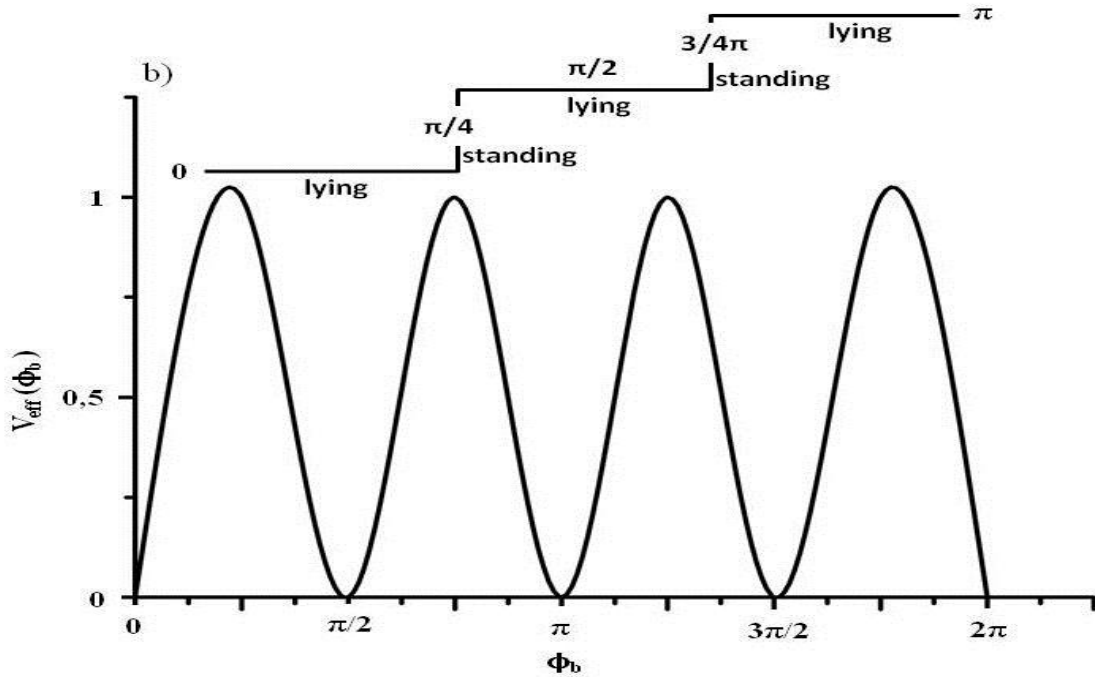


**Figure 3.4:** here we show the dependence of effective potential for the condition shown in B). For the condition shown in B) we have now minima both at  $\pi/2$  and  $\pi$  at the same time.

**C)** If  $\Delta\chi = 0$  i.e.  $V_{eff}(\phi_b) \sim |\sin \phi_b|$ , the minima will appear at  $0, \pi, 2\pi$  etc. and therefore we obtain  $\pi$ -kinks. In Figure 5.2.3 (Chapter 5.2) this region is represented on the top of the graph for field frequency of  $\nu = 11$  Hz i.e.  $\omega/2\pi = \Omega = 11$  Hz.

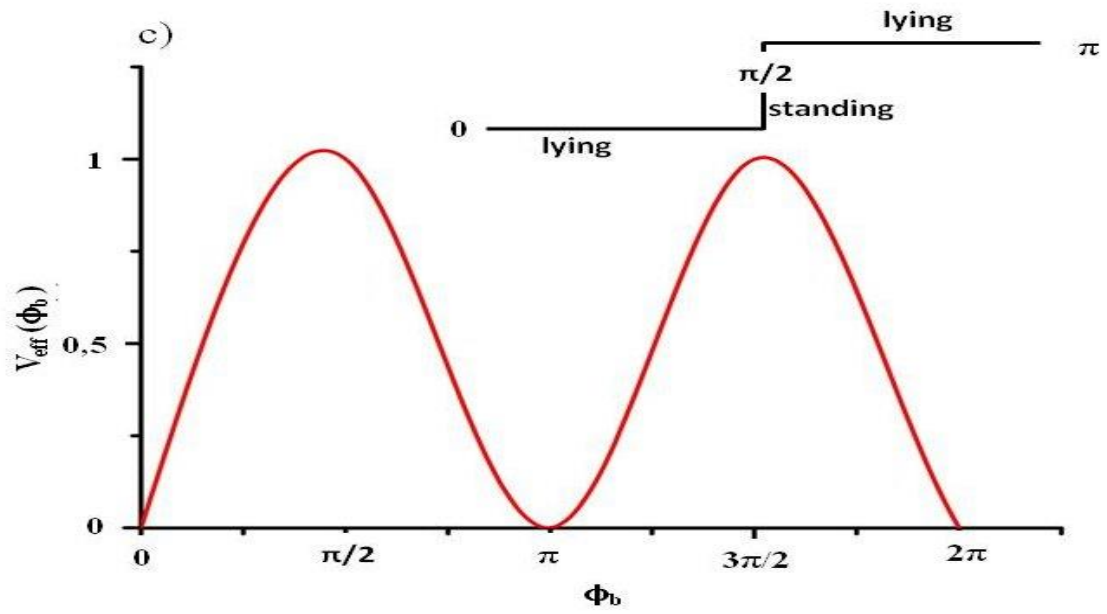


*Figure 3.5: here we show the dependence of effective potential for the condition shown in C). The kink will connect two lying positions. The small scheme above shows a characteristic kink profile.*

# 4 Experimental setup

In this chapter we will outline the most important parameters of experimental setup and configuration of the external magnetic field used in experiments presented in Chapter 5. In Chapter 2 one can find experimental results from several groups that were used as motivation for this thesis. In our experimental work we follow the basic idea and organization of experiments as performed by this group. In our experiment we make some change comparing to them. These changes have been outlined in this chapter and in more details, concerning the materials and methods used in our experiment, in Chapter 6 (materials and methods). This chapter will be organized in the same way as Chapter 6 i.e. in the way that reader can easily find all necessary information for fully understanding of the experimental results.

## 4.1 Friction-controlled bending solitons as folding pathway toward colloidal clusters

Superparamagnetic particles were added to the Petri dish and due to gravity they were sedimented at the bottom. Due to interplay between gravity and repulsion with the glass surface, particles stay mobile and levitate above the glass surface at the few nanometers distance. Applying dynamic magnetic field ( $\mathbf{H}(t) = H e_x$ ) in the direction of the x-axis particles will organize in the chains parallel to the lines of the magnetic field. When chains reach certain length ( $\geq 25$  particles) we apply the dynamic magnetic field in the direction of the y-axis with phase difference of  $90^\circ$ , creating the rotating magnetic field in x-y plane ( $\mathbf{H}(t) = H(\cos \omega t e_x + \sin \omega t e_y)$ ). In Figure 4.1 we outline the schematic representation of the rotating magnetic field and the sketch of the magnetic coils configuration. More details one can find in the Chapter 5.3.1 and in the Chapter 6.2.1. All experiments were visualized with the polarization microscope Leica DM 2500P using a 100x oil immersion objective and 0,55x C-mount. Videos were recorded with the help of the digital color camera Basler A311fc at 30 frames per second. More details can be found in Chapter 6.1.3

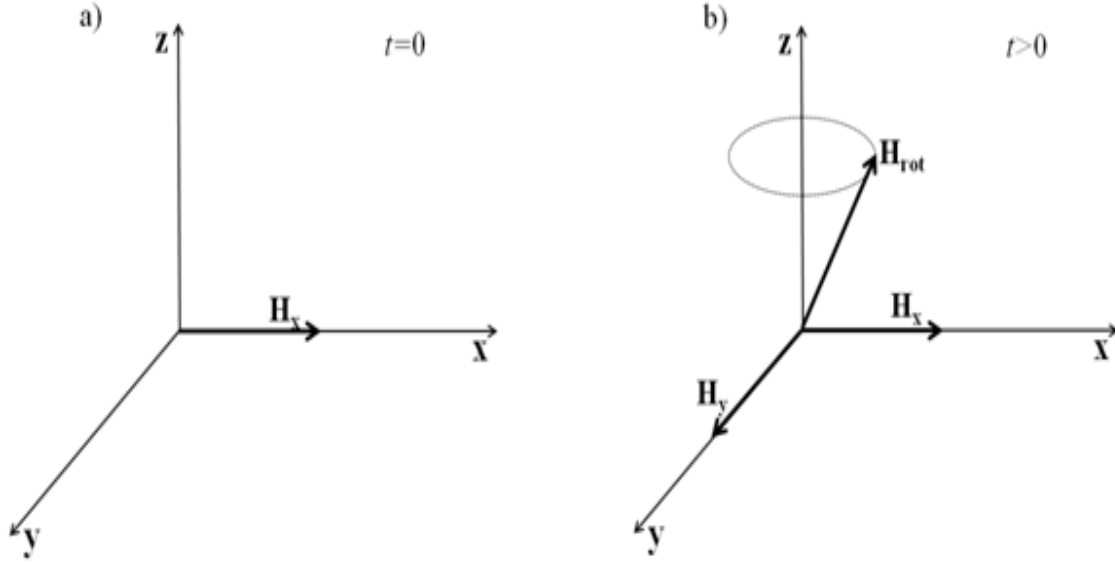


*Fig 4.1: a) Schematic representation of the arrangement of the three perpendicularly orientated solenoid coils with the soft iron core and b) initial position of the chain of the paramagnetic particles and the combined rotating magnetic field  $H$  parallel to the  $x$ - $y$  plane*

## 4.2 Dynamic conformations of self-assembled helical ribbons

Superparamagnetic particles were added to the Petri dish and due to the gravity they were sedimented at the bottom. Due to interplay between gravity and repulsion with the glass surface, particles stay mobile and levitate above the glass surface at the few nanometers distance. Applying time varying magnetic field  $H$  in the direction of the  $x$ -axis particles will organize in the chains parallel to the lines of the magnetic field. When chains reach certain length ( $\geq 40$  particles) we apply the dynamic magnetic field in the direction of the  $y$ -axis with a phase difference of  $90^\circ$ , creating the dynamic magnetic field that will induce attractive force between the chains in the direction of  $y$ -axis. Thus we are able to create structures that consist of two chains in direct connection (further for this structure we use the name ribbon). Naturally this process can lead to the structures that have a nucleation seed of chains in third and fourth layer. The methods of healing of these structures are discussed in more details in the Chapter 5.3.3. When the ribbon is created, we apply the dynamic magnetic field in the direction of  $z$ -axis creating rotating magnetic field in  $y$ - $z$  plane. A time dependent magnetic field that drive our system is  $\mathbf{H}(t) = \hat{H}(\cos \theta_{ext} \mathbf{e}_x + \sin \theta_{ext} \sqrt{2(1-\epsilon)} \mathbf{e}_y \cos(\Omega t) + \sin \theta_{ext} \sqrt{2(1+\epsilon)} \mathbf{e}_z \sin(\Omega t))$ , where  $\theta_{ext}$  is the average precession angle and  $\epsilon$  is the

eccentricity that moves around the director along the x-axes. Depending on the frequency of the magnetic field we vary the eccentricity of the magnetic field in the direction of the z-axis. More details can be found in Chapter 5.3.2 and in Chapter 6.2.2. In Figure 4.2 we outline the schematic representation of the circularly polarized magnetic field (4.2a) and elliptically polarized magnetic field (4.2b)). The sketch of the magnetic coils configuration is the same as presented in Figure 4.1a). All experiments were visualized with the polarization microscope Leica DM 2500P using a 50x oil immersion objective and 0,75x C-mount. Videos were recorded with the help of a digital color camera Basler A311fc at 30 frames per second. More details can be found in Chapter 5.1.3

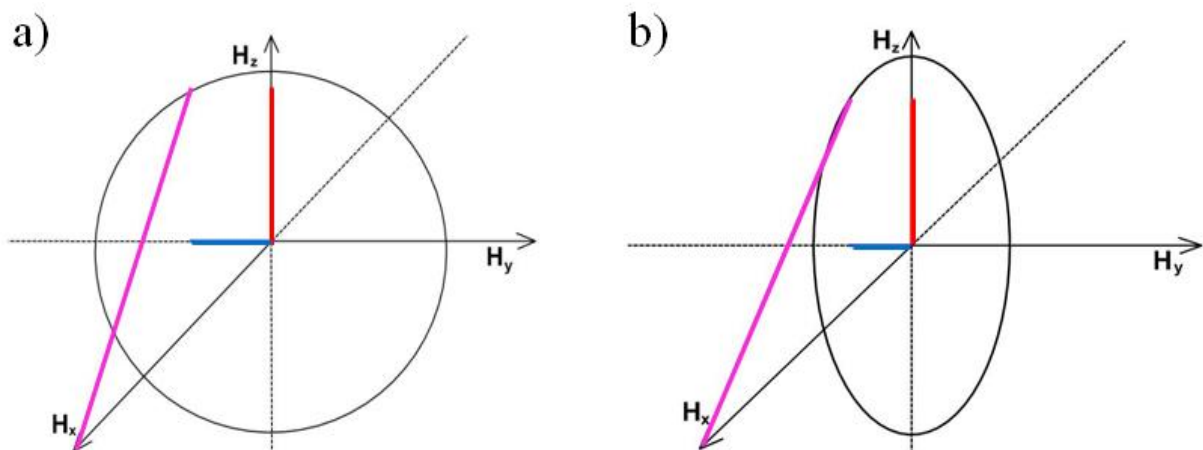


*Fig 4.2: a) schematic representation of the circularly polarized magnetic field is marked with the pink line, red lines represent field modulation in the direction of z-axis and blue lines represent field modulation in the direction of the y-axis and b) schematic representation of the elliptically polarized magnetic field is marked with the pink line, the red line represents field modulation in the direction of the z-axis and the blue line represent field modulation in the direction of y-axis.*

### 4.3 Healing of the ribbons, frequency and eccentricity dependent colloidal structures

We repeat the similar procedure as it was described in Chapter 4.2. One difference compared to the previous method is the elliptical field in the direction of the y-axis. In Figure 4.3 we outline the schematic representation of the elliptically polarized magnetic field in the direction of the y-axis. All experiments were visualized with the polarization microscope Leica DM 2500P using a 50x oil immersion objective

#### 4 Experimental setup

---

and 0,75x C-mount. Videos were recorded with the help of a digital color camera Basler A311fc at 30 frames per second. More details can be found in Chapter 5.1.3

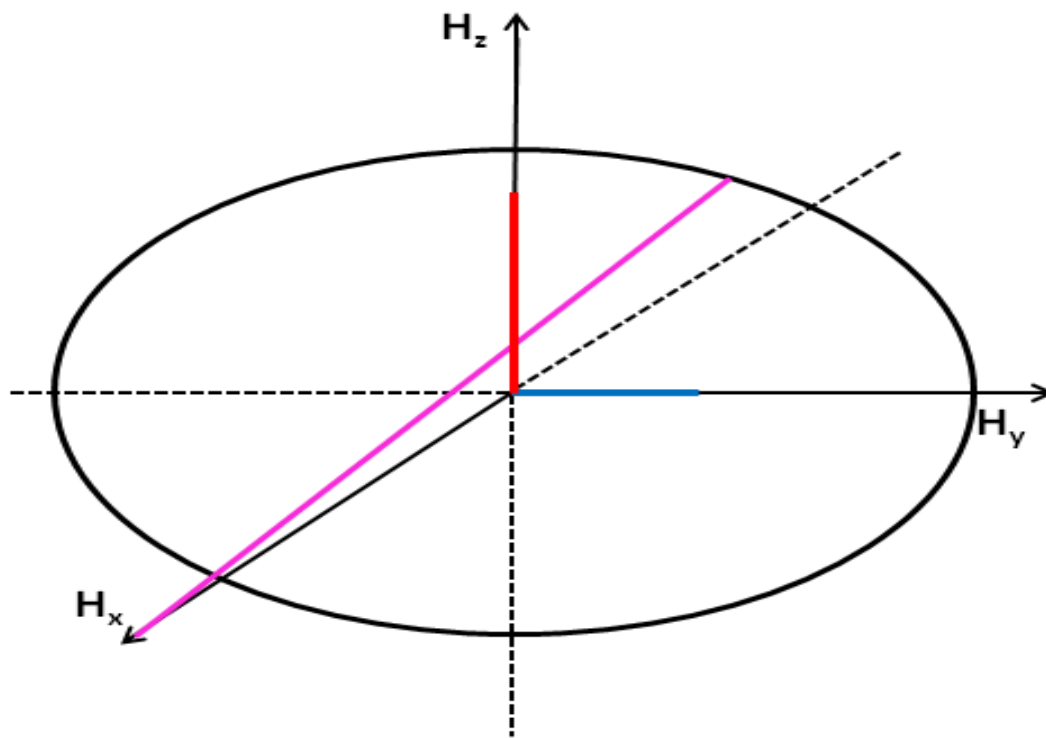


*Fig 4.3: schematic representation of the elliptically polarized magnetic field is marked with the pink line, the red line represents field modulation in the direction of the z-axis and the blue line represents field modulation in the direction of the y-axis.*

# 5 Experimental results

## 5.1 Friction-controlled bending solitons as folding pathway toward colloidal clusters

In this chapter we will present different conformational transitions of an ensemble of magnetic particles from a linear chain to a compact cluster when subjected to modulations of an external magnetic field. We show that the transient dynamics induced by switching the field from static to rotating are governed by the relative friction of adjacent particles in the chain. In this chapter we show that difference in relative friction results in different pathways. As we mention in Chapter 2.3.3, solid particles show bending solitons counter-propagating along the chain while buckling of the chain is the mechanism preferred by ferrofluid droplets. By combining real-space experiments with numerical simulations we unveil the underlying mechanism of folding pathways in driven colloidal systems. By combining two different experiments with numerical simulations, we clearly show that the chosen pathway depends on the differences in relative friction. The results presented in this chapter have been published in the journal *Europhysics Letters* (*N. Casic et al. 2010 EPL 90 58001*)

### 5.1.1 Introduction

Folding pathways in conformational space are crucial to understanding protein folding [1-5]. The pathway of a protein from its unfolded to the biological relevant folded conformation has been described as a statistical path through the multi-dimensional energy landscape in conformational space. Rate-determining regions of such paths are the saddle points in the energy landscape passed by the folding pathway [6]. More than one saddle point generically leads to a multi-exponential relaxation process. Cross correlations of stochastic forces occurring due to the collision of solvent molecules with the protein give rise to hydrodynamic frictional forces which could affect the chosen pathway. Hydrodynamic friction may thus play an important role in polymer [7] and protein [8] folding by speeding up the folding process. Colloidal suspensions are mesoscopic systems, where complex structures and dynamics resulting from simple and tunable interactions between individual particles can be studied in real space. Thus they have been used as models for crystalline assemblies [9], glasses [10],

van der Waals crystals [11], phononic crystals [12] and dipolar chains [13]. Colloidal chains might, however, also serve as a model system for folding pathways.

As mentioned previously (in Chapter 2.3.1 and 2.3.2), in an external magnetic field, chains of paramagnetic particles can rotate synchronously with magnetic field, with a phase lag angle, or they can break into shorter chains which then rotate synchronously with the field. In our experiment we also notice breaking of long chains into shorter ones. Further increases in frequency will lead to a novel type of behavior in which chain will curl into a cluster. In Figure 5.1.1 this behavior is present in the regions marked with red circles. Black squares mark the areas where the magnetic field is not strong enough to induce rotation of the chain. This is the area where  $\lambda > \lambda_c$  (equation 3.23) and chains are formed but thermal fluctuations of the particles in the chain still exist. Areas marked with blue triangles show the area in which chains will break again but rotation is not synchronous with the field. This is the region of chaotic behavior of the system, in which particles will collide with each other then rotate. In our experiment we make detailed observations and investigations of the area where chains curl into clusters (marked with red circles). We show that for paramagnetic colloidal chains interacting via time-averaged dipolar interactions not only the speed of folding [3, 4], but also the selection of the folding pathway are controlled by the complexity of the friction between the particles during the conformational transition.

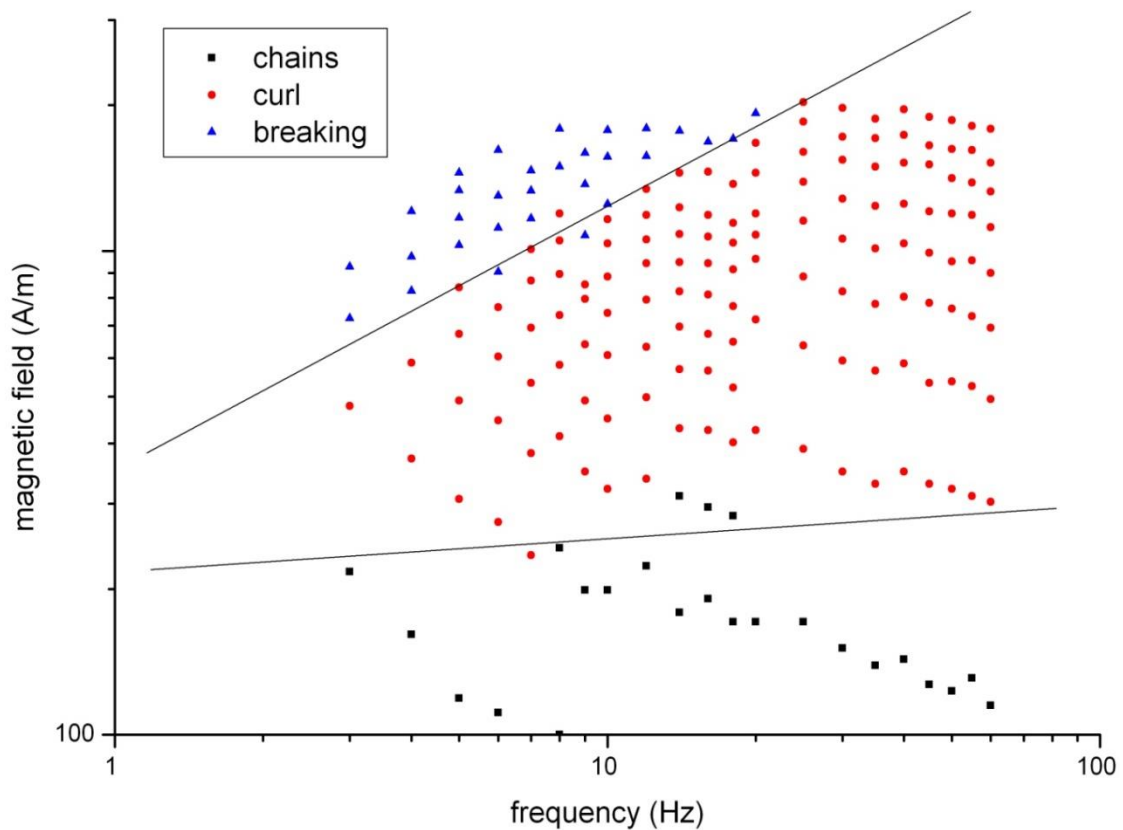


*Fig 5.1.1: Experimental observation of the system for different value of frequency and magnetic field. Red circles show the area for which curling is observed. Area with blue triangles shows breaking of the chains when submitted to high magnetic field. In this area chains will break into doublets due to chaotic movement of the particles. Black squares show area in which no curling or rotation of the chain is observed in experimental time.*

Here we will present the conformational change of a 1D assembly of magnetic particles from a pearl chain to a cluster. We realize a 1D chain by applying a static magnetic field (for the preparation of the chain, see Chapter 6.2.1) and force the particles into a 2D compact cluster by suddenly switching from a static to a rotating field. At high rotation frequencies, the pearl chain curls up into two spirals wrapping the chain into a cluster. We show that the dynamics of the curling-up of the pearl chain can be understood by two localized bending solitons moving from both ends of the pearl chain toward the center. The longer folding pathway via the bending solitons is preferred over the shortest pathway consisting of a buckling of the chain, the latter being suppressed by the friction between adjacent particles.

### 5.1.2 Results and discussion

We apply an external magnetic field using two coils perpendicular to each other ( $\mathbf{e}_x$ ,  $\mathbf{e}_y$  directions), mounted on an optical microscope (More details can be found in Chapter 4.1 and Chapter 6) [14, 15]. In a rotating magnetic field of angular frequency  $\omega$ ,  $\mathbf{H} = H(\cos\omega t\mathbf{e}_x + \sin\omega t\mathbf{e}_y)$ , the particles acquire a magnetic moment  $\mathbf{m}(\omega) = V \chi_{eff}(\omega) \cdot \mathbf{H}(\omega)$  proportional to the field, with  $V = (4/3)\pi a^3$  being the particle volume and where  $\chi_{eff}(\omega) = 3(\mu_p - \mu_s) / (\mu_p + 2\mu_s)$  is the effective dynamic magnetic susceptibility. Here  $\mu_s$  and  $\mu_p$  are the permeabilities of the solvent and the particle, respectively [24].

The dipolar interaction energy between the induced moments of two equal particles located at  $\mathbf{r}_1(t)$  and  $\mathbf{r}_2(t)$  is

$$W = \frac{\mu_0}{4\pi} \mathbf{m}(\mathbf{r}_1(t)) \mathbf{m}(\mathbf{r}_2(t)) : \frac{3\mathbf{r}(t)\mathbf{r}(t) - r^2\mathbf{1}}{r^5}, \quad (5.1)$$

where  $\mathbf{r}(t) = \mathbf{r}_1(t) - \mathbf{r}_2(t)$  is the separation of the dipoles. Such interaction results in a relative particle motion at a typical shear rate of magnitude  $\Omega$ . The dipolar interaction energy will have a minimum value when the two dipoles are aligned with  $\mathbf{r}$  and maximum when they are perpendicular. As a consequence of this behavior preferential aggregation of particles into chains will be in the direction of the field. The dimensionless Mason number  $Mn = \eta\omega/\mu_0\chi^2H^2$  characterizes the ratio of viscous vs. magnetic interactions [16], where  $\eta = 10^{-3} \text{ Nsm}^{-2}$  denotes the water viscosity (For more details about the Mason number, see Chapter 3.4). The viscous dissipated power  $P_{visc} \propto r^3\eta\Omega^2$  cannot exceed the driving magnetic power  $P_{magn} \propto ra^2\mu_0\chi^2H^2\Omega$  such that the shear rates must be always smaller than

$$\frac{\Omega}{\omega} < \frac{a^2}{r^2} Mn - 1 \quad (5.2)$$

If  $Mn$  is low, Eq. (5.2) can be satisfied at shear rates  $\Omega = \omega$  for conformations with particle separations  $r < aMn^{-1/2}$  and the motion is synchronous with the magnetic field. Hence for  $Mn < 1$ , the time-dependent dipolar energy,

$$W = -2 \frac{\mu_0}{4\pi} m^2 P_2 \frac{\cos \varphi(t)}{r(t)^3}, \quad (5.3)$$

can be minimized by an instantaneous minimal conformation  $\varphi(t) = \varphi_0$  of the particles that synchronously rotate with the field and the magnetic moment. Here  $\varphi(t)$  denotes the angle between the magnetic field and the particle separation and  $P_2(\cos \varphi)$  is the second-order Legendre polynomial. Instantaneous minimal conformations are pearl chains oriented parallel to the field. Increasing  $Mn$  (i.e.,  $\omega$ ) the synchronous rotation is possible only for clusters with smaller size, while larger assemblies fragment into smaller assemblies. The shapes of synchronously rotating assemblies and their fragmentation upon adiabatic increase of  $Mn$  have been studied in detail in the literature [17-19] (more detail about Mason number one can find in Chapter 3.4). Here we are interested in the dynamics when suddenly switching to very large  $Mn$ , where even the smallest fragments cannot follow the field. If  $Mn$  is very large,  $Mn > M_c \approx 1$ , synchronous shear rates can no longer be supported and the time scale of the motion of the particles separates from the time scale of the magnetic field,

$$\frac{\Omega}{\omega} = 1 - \sqrt{1 - \left(\frac{M_c}{Mn}\right)^2}, \quad (5.4)$$

At high  $Mn$  the magnetic dipole interaction between the particles can be averaged over a period of the magnetic field rotation at essentially fixed particle positions,

$$\overline{W} = -\frac{\mu_0}{4\pi} \overline{\mathbf{m}(\mathbf{r}_1(t))\mathbf{m}(\mathbf{r}_2(t))} : \frac{3\mathbf{r}(t)\mathbf{r}(t) - r^2(t)\mathbf{1}}{r^5(t)} \quad (5.5)$$

where the bar denotes the time average over one period. Conformations at high  $Mn$  hence minimize the time averaged dipole interaction in Eq. (5.5). For a magnetic field rotating around the z-axis the time-averaged outer vector product of the magnetic

moments is  $\overline{\mathbf{m}(\mathbf{r}_1(t))\mathbf{m}(\mathbf{r}_2(t))} = m^2(\mathbf{e}_x\mathbf{e}_x + \mathbf{e}_y\mathbf{e}_y)/2$  and the dipole energy between the particles reads:

$$\overline{W} = \mu_0 4\pi m^2 P_2(\cos \vartheta)/r^3(t), \quad (5.6)$$

with  $\vartheta$  being the angle between the particle separation vector and the axis of rotation. Minimal dipole energy conformations therefore correspond to clusters in the plane of rotation  $\vartheta = \pi/2$ . Note that the structure of eq. (5.3) and eq. (5.6) only differ in sign and a factor of 2, as well as in the meaning of the angle in the second-order Legendre polynomial.

Thus, a field rotating at high frequency compared to a static magnetic field just reverses the role of attraction and repulsion. The static dipole interaction is attractive along the principal axis (defined by the magnetic field) and repulsive in the plane perpendicular to it. The time-averaged dipolar interaction is repulsive along the principal axis (defined by the rotation axis) and attractive in the plane perpendicular to it.

To assemble particles into a compact cluster, we suddenly switch the magnetic field from a static to a rotating in-plane field,

$$\mathbf{H}(t) \begin{cases} H\mathbf{e}_x, & \text{for } t < 0, \\ H(\cos \omega t \mathbf{e}_x + \sin \omega t \mathbf{e}_y), & \text{for } t > 0, \end{cases} \quad (5.7)$$

where the electronic switching time ( $\sim 20$  ms) of our wave generator is much faster than the Brownian self-diffusion time ( $56$  s)<sup>2</sup>.

We observe two different transient scenarios for the paramagnetic colloids, depending on the value of  $Mn$ . As we already mention in Chapters 2.3.1 and 3.2.2, at low  $Mn$ , when switching to the rotating field, the pearl chains fragment into small

---

<sup>2</sup> The paramagnetic colloids have self-diffusion coefficient  $D=0.14 \mu\text{m}^2 \text{s}^{-1}$  and the time to diffuse double of their size  $d$  is  $\tau = d^2/D$ .

rotating assemblies. These small clusters with particle separations  $r < aMn^{-1/2}$  synchronously rotate with the external field and attract each other to reassemble into a larger circular cluster. For  $Mn \gg 1$  no fragmentation of the pearl chains is observed. Instead, the chains start to bend in opposite directions on their two ends until the extremes of the chain form two equilateral triangles with the two adjacent particles (Figure 5.1.2,  $t = 1$  s). These equilateral triangles are the nucleation seeds of two 2D clusters that start to grow at the expense of the pearl chain by rolling up the chain from two sides (Figure 5.1.2,  $t > 1$  s). After formation of this triangles process of folding is irreversible i.e. the particles cannot be returned to the 1D chain configuration. We describe the chain dynamics in terms of the curve  $\kappa(s, t)$ , where  $s$  denotes the arc length along the curling chain. The curvature  $\kappa(s, t) = |\partial^2 x / \partial s^2|$  measures the shape of the curved chain and the bending rate  $\dot{\kappa}(s, t) = \partial \kappa / \partial t$  measures the change in shape upon bending. We use video-microscopy and particle tracking routines to obtain the individual particle position and extract  $\kappa(s, t)$ . The bending rate along the chain as a function of time is shown in Fig. 5.1.2. Initially the bending rate peaks with opposite signs at the two ends of the chain.

Then the two peaks move with constant speed  $v = 7.6 \mu\text{ms}^{-1}$  (the step-like features in the peaks are due to the discreteness of the colloids) into the middle of the chain. When the bending soliton passes over a particular position in the chain this position is absorbed into the rolling 2D cluster. From the contour plot of the bending rate it follows that the pearl chain is subject to weak bending fluctuations which rattle the pearl chain before it is absorbed into one of the two rolling clusters where the bending fluctuations cease. Moreover, the 2D cluster shows an increased rigidity with respect to the pearl chain.

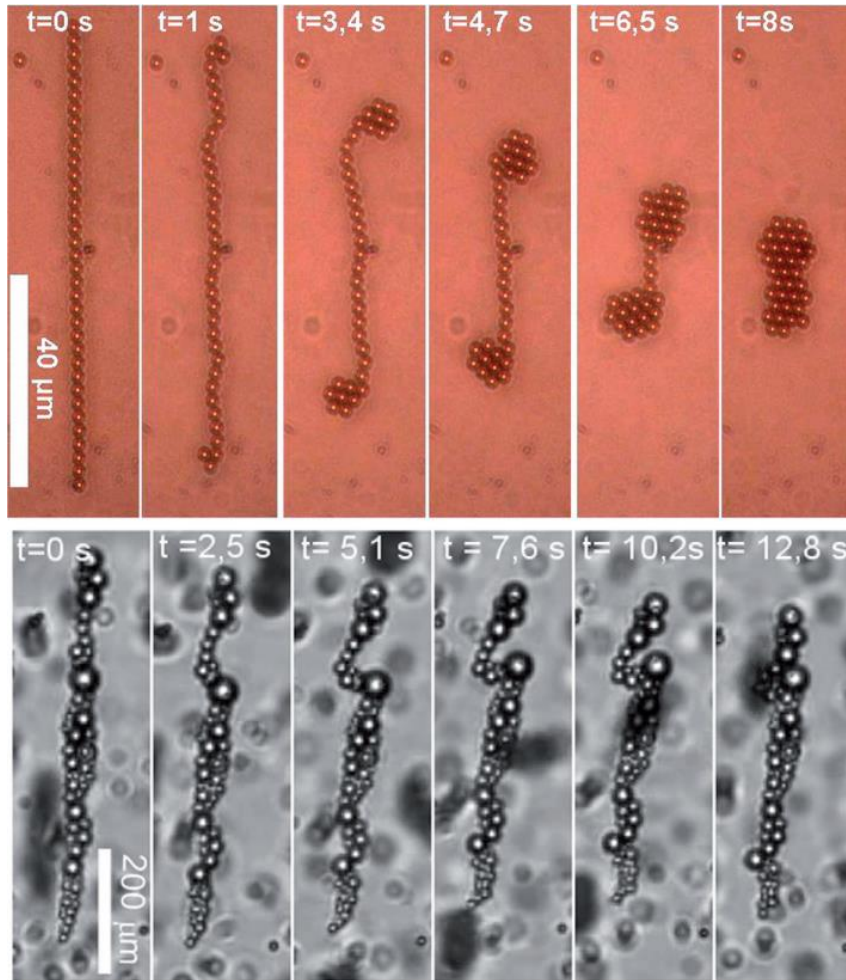


**Fig. 5.1.2:** Top: conformation of a pearl chain of 35 paramagnetic particles as a function of time in a rotating magnetic field ( $H = 900\text{A/m}$ ,  $\omega = 113\text{ s}^{-1}$ ). Bottom: conformation of a pearl chain of ferrofluid droplets as a function of time ( $H = 1600\text{A/m}$ ,  $\omega = 113\text{ s}^{-1}$ ). In both experiments the rotating field is switched on at  $t = 0\text{ s}$ . The folding is irreversible and a switching back from the rotating to the static magnetic field results in different conformational changes.

As one can see from the last sequence frame ( $t=8\text{ s}$ ) in the top part of Figure 5.1.2, the 2D rolling cluster will, at the end, form one big cluster. This cluster will continue to rotate in the magnetic field with a frequency lower than the frequency of magnetic field. This is due to the characteristics of equation (5.6) in which attractive force will now act in the plane perpendicular to the principal axis (defined by the rotation axis) causing attraction between the neighboring particles. In the work of Tierno et al. it was shown that only particles located at the border of cluster will experience significant dipolar force, while for the particles in cluster interior, the dipolar interaction force arising from neighboring particles will cancel each other. Compared to the larger cluster, which are 2D assemblies' doublets and chains are 1D

## 5.1 Friction-controlled bending solitons as folding pathway toward colloidal clusters

---

assemblies that cannot be shear deformed. Cluster rotation at high precession frequencies is caused by dissipative shear deformation, traveling around the cluster with the frequency of the precessing magnetic field. Due to internal relaxation processes that manifest themselves as peaks in  $\omega \propto \chi''_{\text{eff}}(\Omega - \omega)$ , the cluster will rotate. Here  $\chi''_{\text{eff}}$  is the effective dynamic magnetic susceptibility tensor [14].

In Fig. 5.1.3 we plot the speed  $v$  of the bending soliton vs. the field amplitude  $H$  for different field frequencies  $\nu = \omega/2\pi$ . The soliton speed scales like

$$v \propto \omega^0 H^{-3/2}, \quad (5.8)$$

and is thus independent of  $\omega$ , showing a scaling exponent with  $H$  smaller than the exponent 2 occurring in the dipolar interaction (equation (5.3)). We measure the length of the pathway in conformational space as the average of the path lengths of the individual particles, e.g.:

$$\mathcal{L} = \frac{1}{L} \int_0^L ds \int |\dot{x}(s, t)| dt \quad (5.9)$$

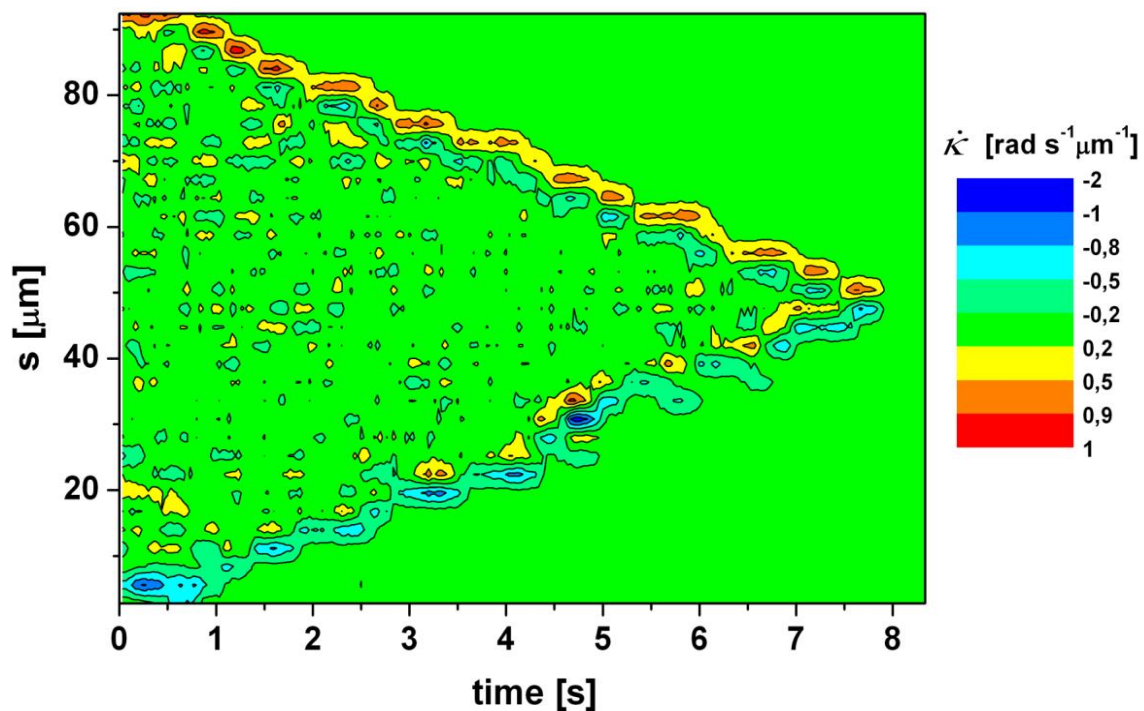


Fig. 5.1.3: Contour plot of the bending rate  $\dot{\kappa}(s, t)$  as a function of the arc-length  $s$  along the chain of paramagnetic colloids and the time  $t$ .

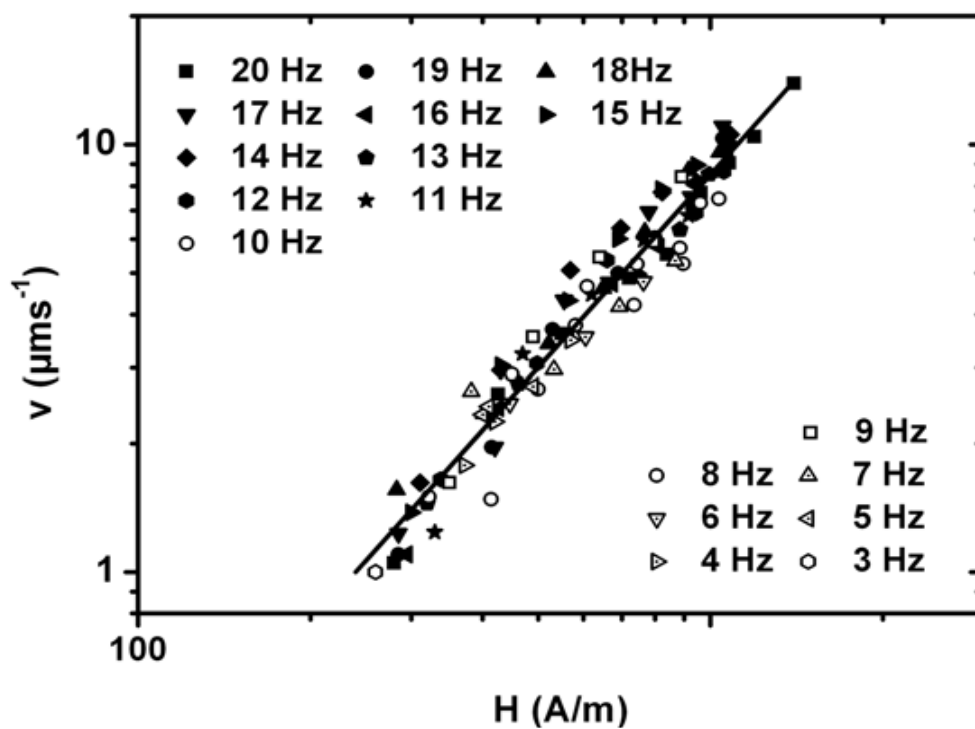
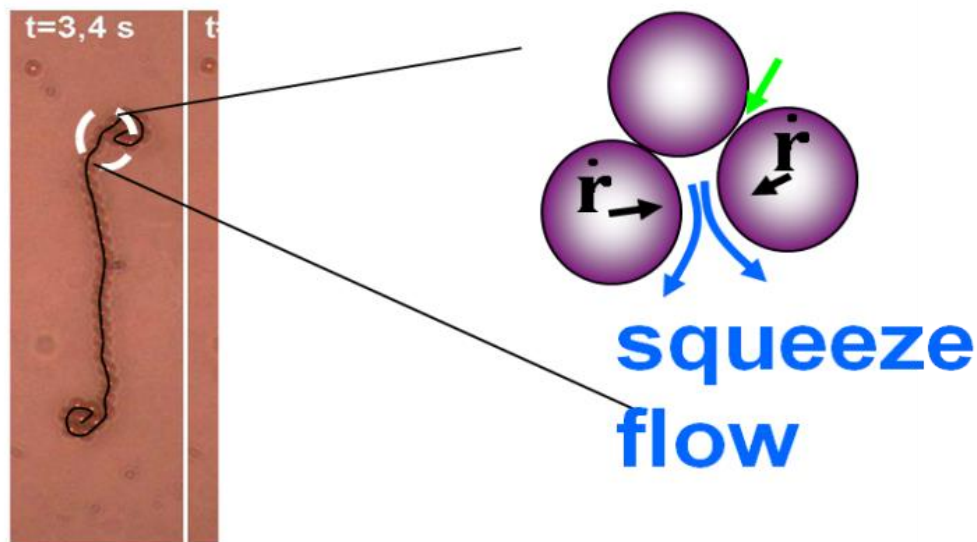


Fig. 5.1.4: Bending soliton velocity  $v$  as a function of the magnetic field strength  $H$  for different frequencies  $\nu = \omega/2\pi$  of the field rotation. The solid line is a fit according to eq. (5.8).

## 5.1 Friction-controlled bending solitons as folding pathway toward colloidal clusters

The pathway chosen by the particle chain is not the shortest path from a chain toward a cluster. In Fig. 5.1.6 we plot the dipolar internal energy  $U$  of an  $N$ -particle system along two different pathways. The first pathway of length  $\mathcal{L}_{sol} = 40 \mu\text{m}$  corresponds to the transition of the particle chain to the cluster via the bending solitons. The second pathway of length  $\mathcal{L}_{buck} = 25 \mu\text{m}$  is a transition of the chain to the cluster via a buckling of the chain. Both pathways end up in equivalent clusters and the dipolar energy monotonously decreases with the path length. Although the buckling takes a shorter path with larger driving force ( $F = -\partial U/\partial \mathcal{L} = 17 \text{ fN}$ ) than for the bending soliton ( $F = 10 \text{ fN}$ ), the particle chain takes the pathway of the bending soliton. The chosen pathway and the behavior of the bending solitons can be understood when considering the hydrodynamic friction arising along the different pathways.



*Fig. 5.1.5: Schematic draw of the area of the squeezing flow. One can see here that collapsing particles will squeeze out fluid remain between three interacting particles. Green arrow indicates Debye length ( $\sim 10 \text{ nm}$ ) pointing that there is small gap between two particles.*

Buckling of the chain requires shear flow in the gap region between all consecutive paramagnetic particles. The particles following the bending soliton pathway can avoid relative motion between the surfaces of adjacent particles by rolling on each other. Only at the position of the bending soliton, where the particle chain is wrapped onto the cluster significant shear flow is produced by pumping out the fluid between the chain and the cluster (Figure 5.1.5). The gap region between two adjacent particles is dictated by the balance of magnetic dipolar attractions and electrostatic double-layer repulsion, thus it is of the order of the Debye length ( $\sim 10 \text{ nm}$ ) and much

smaller than the radius  $a$  of the particles. The hydrodynamic friction in such a region diverges with vanishing gap width and therefore dominates over the hydrodynamic friction that the particles have with the free water. This explains why the speed of the soliton does not change while moving along the particle chain. The driving force is roughly constant and the geometry near the bending soliton does not change. Hence the friction of the squeeze flow near the bending soliton remains similar. The friction with the free water that increases with the size of the cluster can be neglected. It would result in a decreasing soliton velocity. Higher magnetic fields increase the attraction between the particles and narrow the gaps between the particles. A smaller gap increases the friction for the relative particle motion and hence the friction coefficient  $\zeta$  increases with the magnetic field. The speed of the bending soliton  $v = F/\zeta$  is the ratio of the driving dipolar force  $F \propto H^2$  and the friction coefficient. A friction coefficient scaling like  $\zeta \propto H^{1/2}$  is consistent with the experimental scaling in equation (5.8) for the bending soliton velocity. The buckling and folding processes were, until now, noticed only in aforementioned work presented in Ref. [18]. In the limit  $Mn \rightarrow \infty$  (which is an approximation that we can also use), the magnetic rotation is faster than the chain response. They have found that chain will buckle when the viscous force exceeds the elastic force and for this condition the chain will both compress and bend. The response of the chain to this thrust of buckling is to fold onto itself and rotate synchronously as a folded structure. Both types of behavior are due to the effect that decreased length minimizes the drag torque. For explaining the mechanism of folding and buckling they consider magnetic interaction forces between segments in the chain that will interact in these processes. Large compression forces the chain in a way such that segments of the chain come closer to each other causing magnetic interaction between folded segments.

We could not directly visualize the rolling of the beads on top of each other. However, indirect evidence is obtained by comparing the folding of solid colloids to that of liquid droplets. The buckling pathway does not require extensive shear flow if we replace the rigid magnetic particles with ferrofluid droplets. Such droplets can be considered to have a free droplet surface when their size  $a_{drop}$  exceeds the viscous length scale  $a_{drop} > \eta_s/\eta \approx 1 \mu\text{m}$ , where  $\eta_s$  denotes the surface shear viscosity of the droplet [20]. Convection rolls inside the magnetic droplets reduce the friction between the adjacent surfaces of the droplets. Figure 5.1.2 (bottom) shows the transition from a polydisperse pearl chain of ferrofluid droplets towards a cluster. Contrary to the rigid particles the ferrofluid droplets follow the shorter buckling pathway. We have performed also experiments with bidisperse particles to check

## 5.1 Friction-controlled bending solitons as folding pathway toward colloidal clusters

whether polydispersity could affect the chosen pathway since the ferrofluid droplets are polydisperse, but we observe no difference with the monodisperse case.

We support the experimental results with fluid particle simulations where the particles are treated as a part of a liquid of much larger viscosity [21, 22]. We also simulated the dynamics of „slippery” beads by using the method of hydrodynamic interactions between point-like particles in the Rotne-Prager approximation [23]. These simulations (More details can be found in Chapter 3.5) confirm the importance of friction for the choice of the folding pathway.

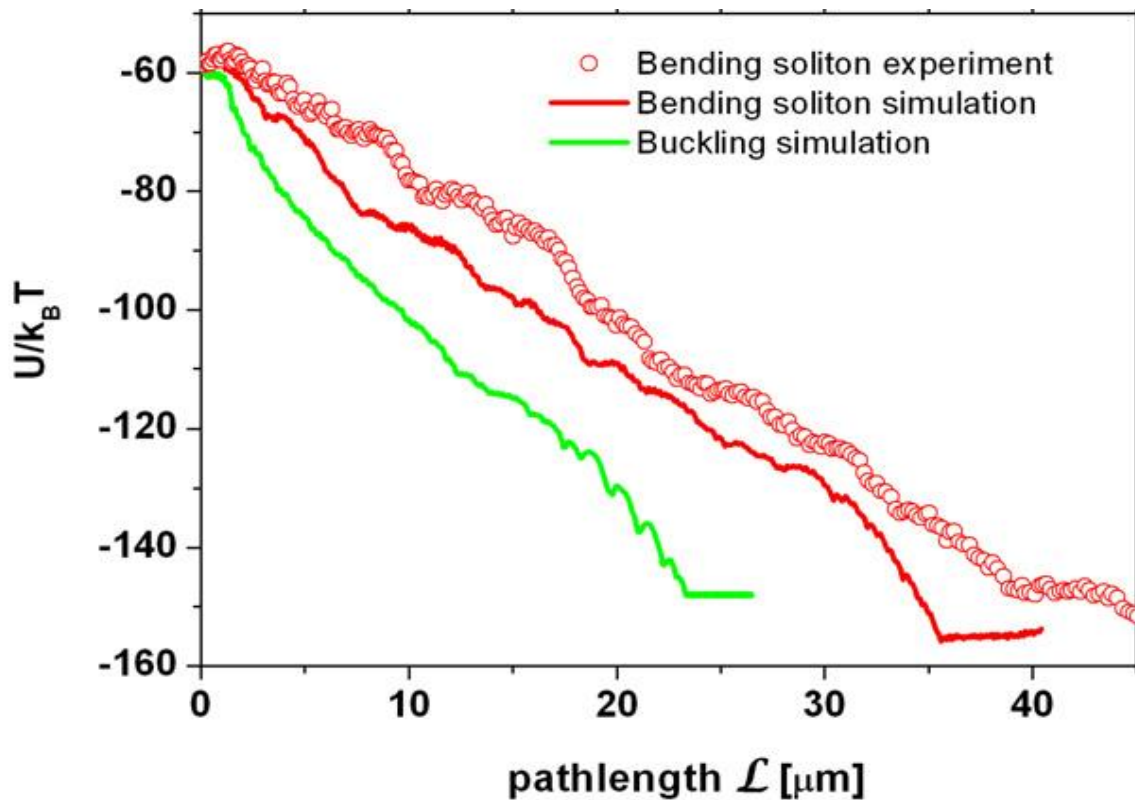


*Fig. 5.1.6: Time-averaged dipolar energy of a 35-particle assembly changing from an extended chain to a cluster along two different pathways. The simulations (solid lines) are computed assuming pairwise additivity of the dipole interaction. The pathway of the steepest descent corresponds to a buckling of the chain. The experimentally observed pathway (circles) of the bending soliton is longer and corresponds to a smaller driving force. The longer pathway is preferred because of the rolling friction between the particles is lower than the sliding friction.*

### 5.1.3 Conclusion

In conclusion we have shown that in our colloidal system the kinetics of folding is dominated by the different friction arising along the slopes of the energy landscape rather than by transition rates over flat saddle points. The short pathway from a pearl chain toward a cluster via the buckling of the chain is suppressed by the friction of relative motion between the adjacent surfaces of the particles and not by presence of barriers in the energy landscape. The system therefore avoids the pathway of the steepest descent and chooses an alternative longer pathway via the bending soliton that minimizes the friction. We confirm these findings by two experiments with different systems. In the system of solid spheres the system follows the lower friction pathway (not the shortest pathway). In the system of ferrofluid droplets the system chooses the lower energy pathway. These findings were supported with agreeable numerical simulations which were able to confirm experimental results. In this way we confirm our results both theoretically and experimentally.

## 5.2 Dynamic conformations of self-assembled helical ribbons

In Chapter 5.1 we have studied the behavior of a 1D chain of paramagnetic particles in an external rotating magnetic field. This magnetic field was applied in the x-y plane. Now we want to study the dynamics of self-assembled and propelled ribbon (which consists of two paramagnetic chains in direct connection and aligned with the direction of the static magnetic field) formed from paramagnetic colloids in a dynamic magnetic field (Chapter 4.2 and 6.2.2). The sedimented ribbon assembles due to time-averaged dipolar interactions between the beads. After the ribbon was assembled we applied the rotating magnetic field in y-z plane. The time dependence of the dipolar interactions together with hydrodynamic interactions causes a twisted ribbon conformation. Domain walls of high twist connect domains of nearly constant orientation and negligible twist and travel through the ribbon. The particular form of the domain walls can be controlled via the frequency and the eccentricity of the modulation. The flux of twist walls - a true ribbon property absent in slender bodies - provides the thrust onto the surrounding liquid that propels this biomimetic flagellum into the opposite direction. The propulsion efficiency increases with frequency and ceases abruptly at a critical frequency where the conformation changes discontinuously to a flat standing ribbon conformation. The results presented in this chapter have been published in the journal *Physical Review Letters* (*PRL 110*, 168302 (2013)).

### 5.2.1 Introduction

The coupling of hydrodynamics to the conformation of a flexible object embedded into a viscous fluid is a question of interest for understanding the mechanism of self-propulsion of biological [99, 100] as well as biomimetic [60] micromotors. Finding the conformational path of the flexible object to induce efficient propulsion [101-104] guides one to the most intelligent design [105] of the motor that leads to optimal performance. Once understood one is able to artificially produce [106] and rebuild [60, 107] biomimetic motors. These propel according to commands by enforcing desired conformational transitions from one to another shape. For a slender motor propelled by surface waves the most efficient motor shape is a helix winding at an angle of  $45^\circ$  around the helix axis with amplitude comparable to the wavelength [108].

Top-down [109] and bottom-up concepts are two ways in achieving the desired conformational path. Following the first concept one stiffens the motor at places where no movement should occur and builds in joints where conformation changes are desired. Bibette and coworkers [60] have used paramagnetic colloidal beads. Joints between the beads were built from DNA linkages between the beads. The top-down built in joints provided bending rigidity to the swimmer. When the bending rigidity was such that this low Reynolds number swimmer behaved semiflexible in a viscous fluid, then nonreciprocal conformation changes of the neutral line of the colloidal chain gave the necessary thrust for a directed motion. Slender body hydrodynamics, i.e. treating the swimmer as a one dimensional curve, was sufficient to explain the propulsion of this swimmer. The sperm number measuring the ratio of elastic bending versus viscous torques is the relevant quantity deciding on the efficiency of the propulsion of Bibette's swimmer. The cross section of the colloidal chain and its torsional rigidity on the other hand were irrelevant for understanding the propulsion.

Alternatively one might exploit the coupling of hydrodynamics and the attractive interactions between building blocks of the deformable object to dynamically self-assemble the desired shape in a bottom up manner. Snezhko and Grzybowski [72, 110] created self assembled snakes and highly organized rings that resulted in an efficient propulsion of both structures. Since their swimmers propelled at high Reynolds numbers, non-reciprocity of the motion is not a requirement and the motion of these swimmers is much more efficient than that of low Reynolds number swimmers.

In our work we follow the bottom-up approach of Snezhko [72] using the same magnetic beads as Bibette [60] that propels at low Reynolds number because of its finite cross section. In our experiment an external magnetic field drives the dynamic nonlinear self-assembly of paramagnetic colloids to a biomimetic at or chirally twisted magnetic colloidal ribbon. In contrast to Bibette's top down swimmer our low Reynolds number bottom up swimmer is fully self assembled. No DNA-links are used and in principle the colloids are free to attain any conformation. Here the interaction of the ribbon with the surrounding fluid provides a feedback mechanism that stabilizes or destabilizes the ribbon conformation that is responsible for the motion.

### 5.2.2 Results and discussion

Mathematically a ribbon differs from a one dimensional curve since it additionally has a one dimensional cross section. While a curve can bend and wind a ribbon can additionally twist. The conformation of a ribbon can be described by its twist and its writhe. Calugareanu theorem [111] states that the sum of the twist - a local ribbon property - and writhe - a global conformation property of the neutral line and thus a curve property - add up to a conserved quantity, the link number of the ribbon. As beating cilia or flagella can be well described by one dimensional curves. They propel entirely by changes in writhe. In our ribbons writhe is not important. In fact the neutral line of our ribbon remains essentially a straight line and does not undergo conformation changes. What matters in our swimmers is the orientation of the ribbon cross section. The ribbon does not propel along its major axis in the flat conformation, but propels in the twisted conformation. Since twist is a local ribbon property we can define the twist density as well as a flux of twist. Open ends of the ribbons allow a steady flux of twist through the ribbon. A parametrically modulated magnetic torque acting on the colloidal ribbon serves as a control parameter for the dynamically self-assembled shape. Shape transition occurs in the forms of  $\pi$ - or  $\pi/2$ -walls that travel along the ribbon. The relevant number to describe the propulsion of our ribbon is the ratio of twist- and viscous torques and not the sperm number as for Bibette's swimmer. Hence our swimmer is propelled by an entirely different ribbon specific mechanism.

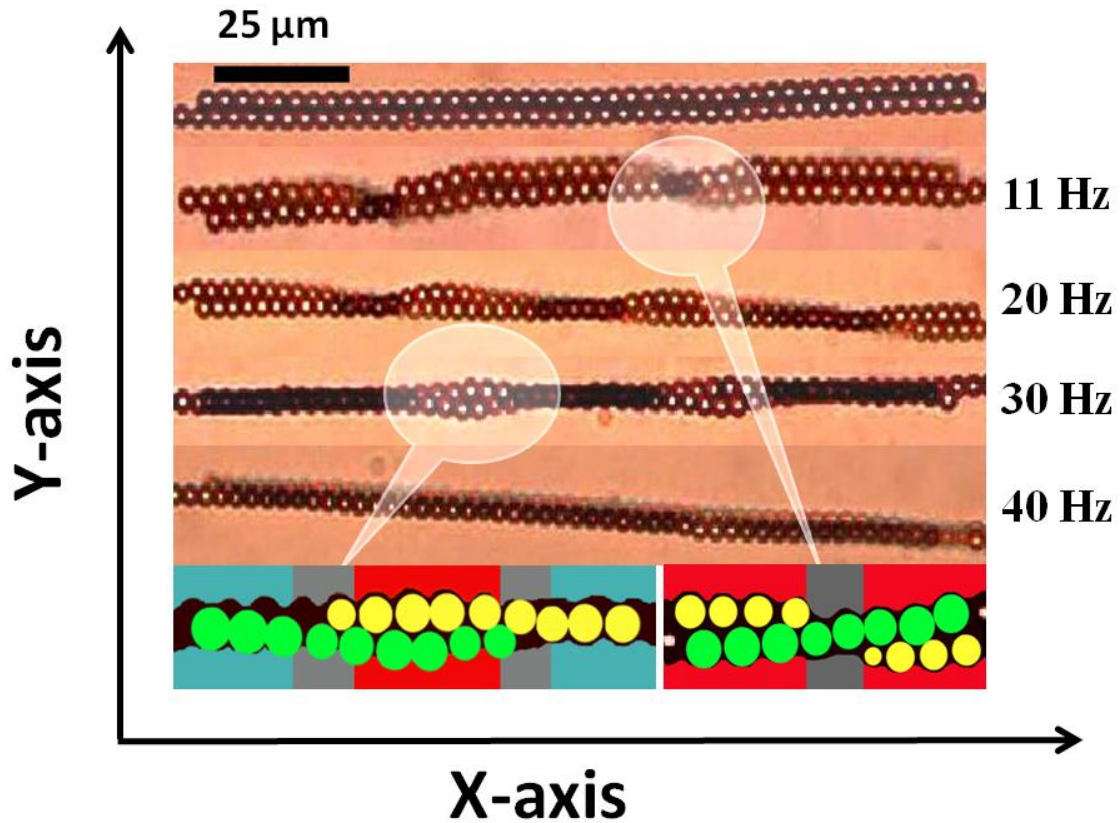


*Fig. 5.2.1: Top: Microscopy image (top view) of a healed colloidal ribbon on a glass surface. The ribbon prepared at a frequency of  $\Omega/2\pi < 18\text{Hz}$  and  $\epsilon \approx -0,05$  lies in an untwisted conformation.  $\Omega/2\pi = 11 - 40\text{Hz}$ : Microscopy images (top view) of the conformation of the ribbon for different frequencies and an eccentricity of  $\epsilon \approx +0,05$ . At the highest frequency  $\Omega/2\pi = 40\text{Hz}$  the ribbon is standing on the glass surface with an angle of  $\phi_b(x) = 2\pi$ . At low frequencies lying domains (sketched in red in the scheme at the bottom) are separated by  $\pi$ -walls (sketched in gray) that when approaching  $\Omega/2\pi < 40\text{Hz}$  split into  $\pi/2$ -walls separating lying from standing (cyan in the sketch) domains.*

The magnetic field  $\mathbf{H}(t)$  induces excess magnetic moments  $m(t) = \eta_0 V \chi H(t)$  in the particle ensemble. Here  $\eta_0$  denotes the permeability of vacuum,  $V$  the volume of the ensemble and  $\chi$  the effective susceptibility. The magnetic moments of the beads hence interact via dipolar interactions. The dimensionless Mason number  $Mn = \eta \Omega / \eta_0 \chi^2 H^2$  characterizes the ratio of viscous vs. magnetic interactions, where  $\eta = 10^{-3} \text{Nsm}^{-2}$  denotes the water viscosity, and the modulation frequency at which the direction of the magnetic field changes. The viscous dissipated power  $P_{visc} \propto \eta r^3 \omega^2$  of a bead moving at a rate  $\omega$  and distance  $r$  around another bead cannot exceed the driving magnetic power  $P_{magn} \propto r a^2 \eta_0 \chi^2 H^2 \Omega$  of the beads of radius  $a$  such that the shear rates  $\omega$  must be always smaller than  $\Omega a / r Mn^{1/2}$ . At the conditions used here the Mason number is large  $Mn > 1$  and the motion of the beads is with a lower rate  $\omega < \Omega$

than that of the magnetic field for any separation  $r > a$  of the beads. This rate  $\omega < \Omega$  of the beads occurs because viscous forces are too strong to allow for a synchronous ( $\omega = \Omega$ ) motion. In fact, the Mason number must be chosen large enough to ensure the integrity of our ribbon. Angular frequencies larger than  $\Omega/2\pi > 11\text{Hz}$  were necessary to prevent disintegration of the chains in the ribbon. Above this lower bound the intra particle dynamics is slow compared to the modulation of the external field. The separation of time scales allows us to also separate dynamic conformational variables of the particle assembly into larger slow and smaller fast components.

Our system is driven by a time dependent magnetic field  $\mathbf{H}(t) = \hat{H}(\cos \theta_{ext}\mathbf{e}_x + \sin \theta_{ext}\sqrt{2(1-\epsilon)}\mathbf{e}_y \cos(\Omega t) + \sin \theta_{ext}\sqrt{2(1+\epsilon)}\mathbf{e}_z \sin(\Omega t))$  of the average precession angle  $\theta_{ext}$  and eccentricity  $\epsilon$  that moves around the director along the x-axes. In this external field we consider a pair of paramagnetic beads separated by the bond vector  $\mathbf{r}_b = r_b(\cos \theta_b, \sin \theta_b \cos \phi_b, \sin \theta_b \sin \phi_b)$ , where  $\theta_b$ , and  $\phi_b$  are the polar and azimuthal angle of the bond vector (figure 5.2.2). The dipolar energy of this pair is then given by  $W(t) = -\frac{\eta_0 V^2 \chi_{bead}^2 H^2(t)}{4\pi r_b^3} P_2(\cos \gamma(t))$ , where  $\gamma(t)$  denotes the time dependent angle between the magnetic field and the bond vector. The time averaging of this interaction can be done most easily by measuring both the orientation of the magnetic field and the bond vector with respect to the director. We find the time averaged dipolar interaction between two beads to be well described by

$$\bar{W} = -\frac{\eta_0 V^2 \chi_{bead}^2 \hat{H}^2(t)}{4\pi r_b^3} \times (P_2(\cos \theta_{ext})P_2(\cos \theta_b) - \epsilon P_2^2(\cos \theta_{ext})P_2^2(\cos \theta_b) \cos(2\phi_b)) \quad (5.10)$$

where  $P_2$  and  $P_2^2$  are Legendre polynomials of degree 2 and associated Legendre polynomials of degree 2 and order 2. We started our experiments with a magnetic field of  $\hat{H} = 2200\text{A/m}$ , a precession angle of  $\theta_{ext} = \pi/6$  and negative eccentricities  $\epsilon \approx -0,05$ . Under such circumstances the time averaged dipole interactions are attractive for a pair of beads separated along the x-direction ( $\theta_b = 0$ ), weakly attractive to indifferent along the y-direction ( $\theta_b = \pi/2, \phi_b = 0$ ), and repulsive along the z-direction ( $\theta_b = \pi/2, \phi_b = \pi/2$ ). Since the interaction is weak along the y direction collective demagnetization effects involving three or more beads play a role along this direction.

Yan et al [112] used those collective effects in magnetic Janus particles to form hollow tubes. Here these collective effects lead to weak attraction in the  $y$ -direction between single chains, but to repulsion in the  $y$ -direction between a ribbon and a third chain or additional bead. At these conditions we can create ribbons of typical length of up to 50 beads per chain. Defects in the form of vacancies on the ribbon or adsorbed beads starting a third chain can be eliminated by using distinct frequencies of modulation and an annealing procedure described in Chapter 5.3. The top part in Figure 5.2.1 shows a microscopy image of such a ribbon.

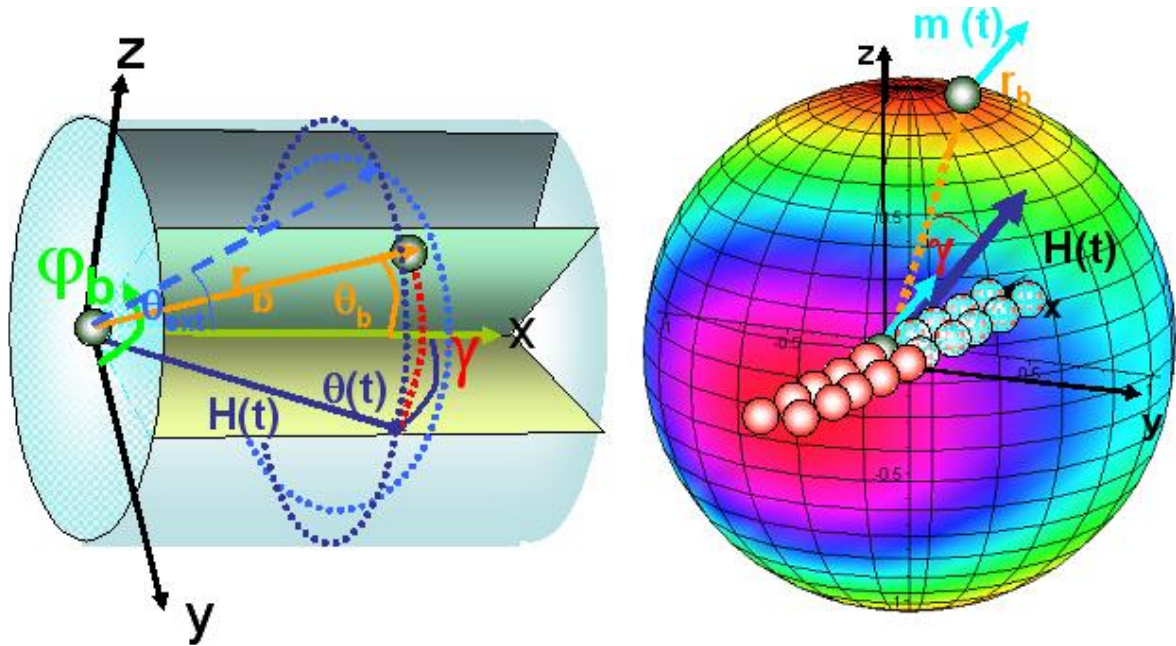


*Fig. 5.2.2: left scheme showing the definitions of angles defined between the director (green), the magnetic field and the bond vector. The magnetic field precesses on an ellipse (purple) that deviates from a circle (blue) but on average encloses the same angle  $\theta_{ext}$  as the average blue field vector with the director. The right image shows a color coded graph of the averaged dipole interaction of a pair of dipoles in various directions for negative eccentricity. Dipoles in this field form bonds in the attractive (purple) direction and avoid bonds in the repulsive (red) direction. Along the cyan direction the averaged dipole interaction is indifferent, and the formation of bonds or no bonds is decided by collective higher order effects.*

Once the ribbon is healed of defects we switch to a modulation with positive eccentricity  $0 < \epsilon \ll 1$ . Positive eccentricity turns the y direction repulsive and the z direction attractive favoring an orientation of the ribbon in an upright position. Due to the spontaneous symmetry breaking twisting of the ribbon can happen at the beginning, at the end or at the beginning and at the end of the ribbon synchronously. If the twist of the ribbon, which will produce the domain wall, happened synchronously at beginning and at the end of the chain, domain wall will travel towards each other as a kink and anti-kink. When kink and anti-kink meet each other they will annihilate. This meeting point where annihilation occurs is, in the most of the circumstances, at the center or close to the center of the ribbon. After some period of the time system will stabilize. This will lead to the case where only kink or anti-kink will appear which is presented on the Fig. 5.2.1 and further discussed in this chapter. Appearance of the kink and anti-kink can be very good indicator for the spontaneous symmetry breaking and denies the influence of other factors such as field gradient in the system.

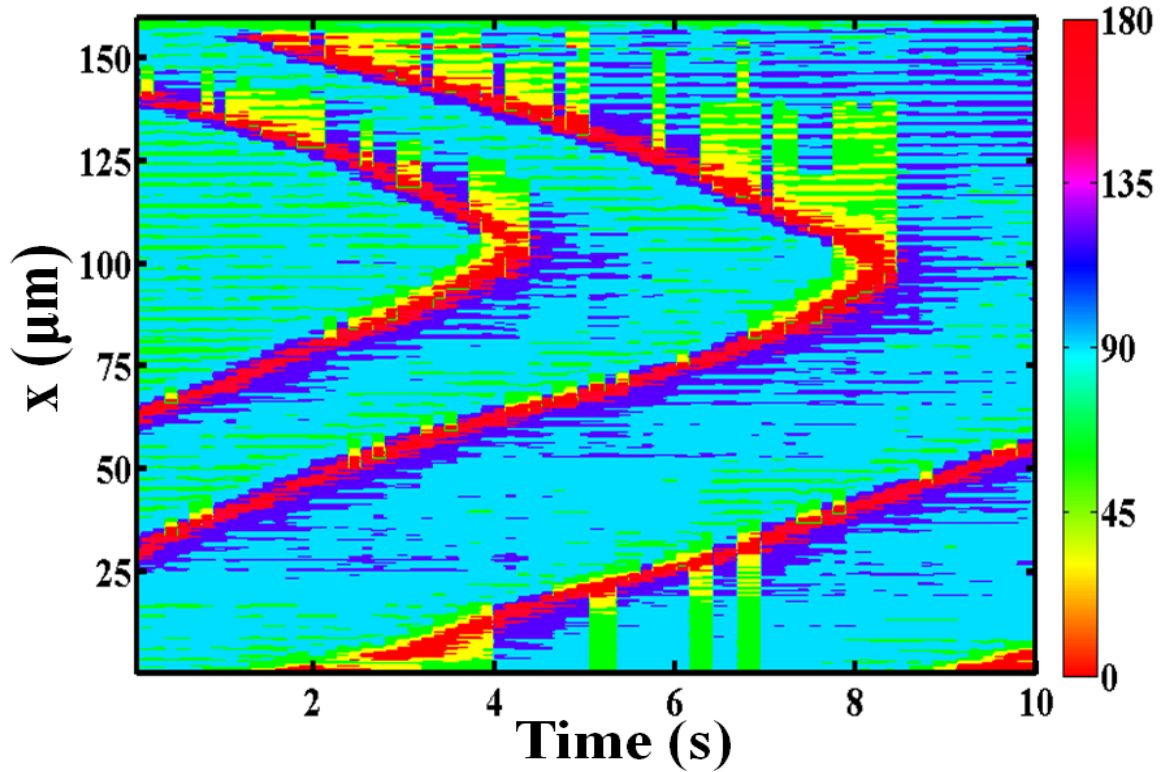


*Fig. 5.2.3: Space time plot of the orientation angle  $\phi_b(x,t)$  for a frequency  $\Omega=2 \pi \times 27$  Hz. Spontaneously broken symmetry will lead to formation of the domain walls at the beginning and at the end of the ribbon. Domain walls created on this way will travel towards each other as a kink and anti-kink and annihilate at the center or close to the center of the ribbon.*

Figure 5.2.1 (40Hz) shows the conformation of the ribbon for positive eccentricity  $\epsilon \approx 0,05$  at a frequency of 40 Hz and a magnetic field of  $\hat{H}= 2200\text{A/m}$  sufficiently strong as to force the ribbon against gravity into an upright conformation. The frequency is high and the separation of the field modulation frequency from the rate of rotation of the ribbon is strong enough as to wipe out all dynamic effects of the modulation onto the ribbon. This is no longer the case if we decrease the modulation frequency. Dynamic torques arising due to dipolar interactions may now distort the conformation described by the tangent vector to the neutral line of the ribbon and the normal to the ribbon plane. The tangent vector of the neutral line of the ribbon remains along the x-axis and the structure is entirely described by the angle  $\phi_b(x)$  the normal vector to the ribbon plane encloses with the z-direction. For frequencies below a full separation of time scales twist walls between subsequent quasi-stable orientations travel in the form of solitons with a speed  $v_{wall}$  through the ribbon. For low frequencies  $11\text{Hz} < \Omega/2\pi < 18\text{Hz}$  such walls are  $\pi$ -walls connecting a lying ribbon section with another lying ribbon section. For frequencies  $18\text{Hz} < \Omega/2\pi < 28\text{Hz}$  these  $\pi$ -walls split into two  $\pi/2$ -walls, the first connecting a lying section of the ribbon with a

standing section and the second connecting a standing section with a lying section twisted by  $\pi$  with respect to the first lying section. For frequencies  $28\text{Hz} < \Omega/2\pi < 40\text{Hz}$  the  $\pi/2$ -walls merge again to  $\pi$ -walls that, contrary to the low frequency regime, connect two standing segments of the ribbon. Finally, above  $\Omega/2\pi > 40\text{Hz}$  a standing at ribbon remains.

In Figure 5.2.4 we show space time plots of the angle  $\phi_b(x,t)$  extracted from the videos of the ribbons for various frequencies. These space time plots show both the behavior of the twist walls traveling at relatively large velocities as well as the forward propulsion of the ribbon with a much smaller propulsion velocity opposing the motion of the kinks. A spatially more resolved version of the propulsion is shown in the inset of the top figure where the behavior around one end of the ribbon is shown. The space time plots span the range  $x_b(t) < x < x_e(t)$ , where  $x_{b,e}(t) = x_{b,e}^0 + v_{prop}t$  denote the propelling beginning and end of the ribbon. The color coding of the plot encodes the angle  $\phi_b$ , red colors correspond to a lying ( $\phi_b=0$ ) section and cyan colors to standing ( $\phi_b=\pi/2$ ). The dominating color of the plot shows whether the ribbon is mainly lying or standing. Abrupt changes in color occur within the twist walls.  $\pi$ -walls connect regions of similar color while the color changes from red to cyan when passing a  $\pi/2$ -wall. From the space time plots it is evident that the conformation, wall and propulsion kinetics critically depends on the driving frequency. Twist walls are produced in a frequency range of  $11\text{Hz} < \Omega/2\pi < 40\text{Hz}$ . Only in this frequency range propulsion along the x direction is observed.

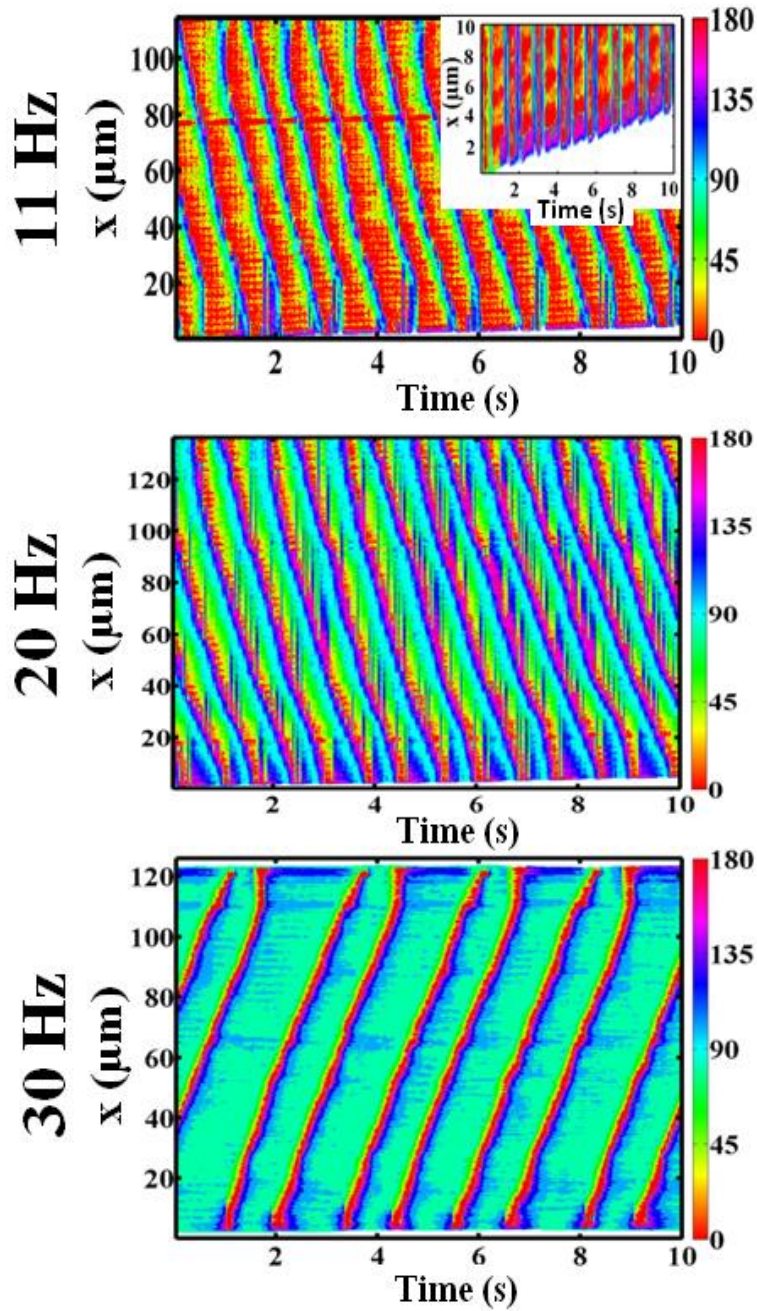


**FIG. 5.2.4:** Three space time plots of the orientation angle  $\phi_b(x,t)$  for different frequencies  $\Omega=2\pi \times 11(20,30)\text{Hz}$ . Top: Lying domains (red) are separated by  $\pi$ -walls traveling along the ribbon (mathematical formulas explaining this kind of behavior one can find in Chapter 3.6 C). The inset magnifies the region of one end of the ribbon that counter propagates the  $\pi$ -walls with much lower speed. Middle: standing (cyan) domains are separated from lying domains (red) by  $\pi/2$ -walls (mathematical formulas explaining this kind of behavior one can find in Chapter 3.6 B). Bottom: standing domains (cyan) are separated by  $\pi$ -walls (mathematical formulas explaining this kind of behavior can be found in Chapter 3.6 A).

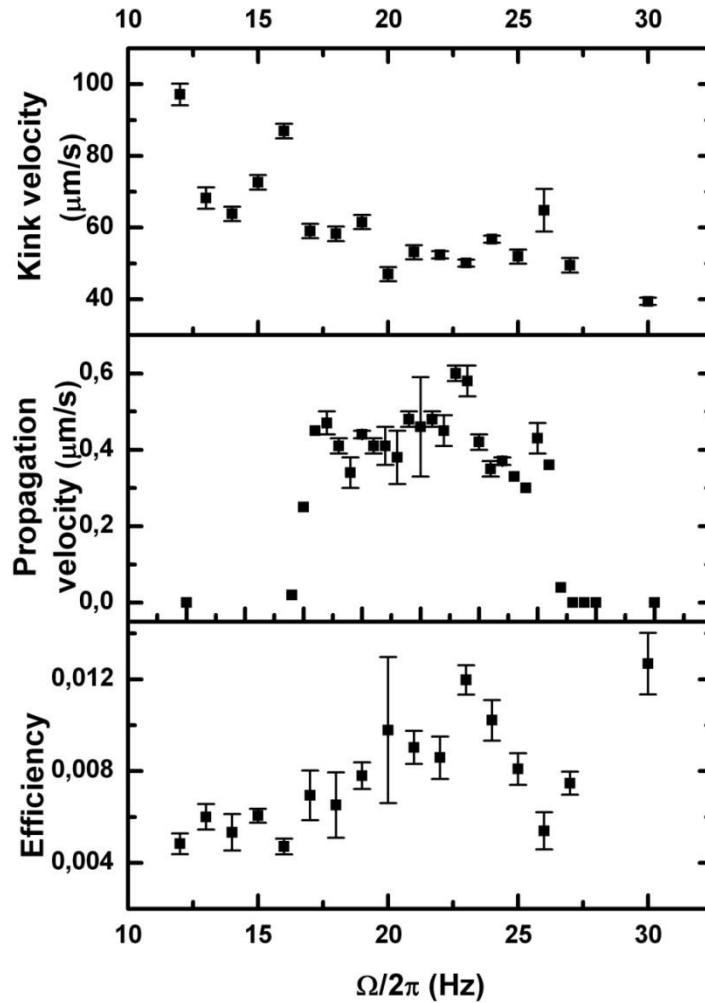


*Fig. 5.2.5: Plot of the domain-wall velocity, propagation velocity, and the geometric propulsion efficiency  $e$  versus modulation frequency  $\Omega/2\pi$ .*

In Figure 5.2.5 we plot the domain wall speed and the propulsion speed as a function of the modulation frequency. Domain walls exist only in the frequency band  $11\text{Hz} < \Omega/2\pi < 40\text{Hz}$  and it is only in this regime where propulsion along the  $x$ -direction is observed. We define a geometric propulsion efficiency  $e = v_{prop}/v_{wall}$  analogue to the one defined in [113] that differs from the power efficiency defined by [101]. It measures the distance a ribbon propels during the motion of one domain wall by the wavelength of the structure. The third graph in Figure 5.2.5 plots this geometric efficiency versus modulation frequency. The efficiency increases with frequency. We may reformulate the efficiency in terms of the frequency  $f$  of rotation of the ribbon and the density of walls  $n = L/\lambda$  as  $e = n \times v_{prop}/Lf$  where  $L$  is the length of the ribbon and  $\lambda$  the wave length of the solitary wave. Since both the propulsion velocity and

rotation frequency of the ribbon are fairly independent of the modulation frequency the efficiency increases as the density of domain walls increases. It requires a relatively soft ribbon to achieve high densities of walls.

We can understand the behavior of the ribbon by a damped relaxation equation  $\partial^2 \phi_b / \partial t^2 + \gamma \partial \phi_b / \partial t = -\delta F / \delta \phi_b(x)$  where  $F = \int dx \{U_{grav}(\phi_b) + \Delta\chi U_{magn}(\phi_b, t) + (\partial \phi_b / \partial x)^2 / 2\}$  is a rescaled functional of the field  $\phi_b(x, t)$  with  $U_{grav}(\phi_b) = |\sin \phi_b|$  the gravitational potential,  $U_{magn}(\phi_b, t) = h_+^2 \cos(2\phi_b - 2\Omega t) + 2h_+ h_- \cos(2\phi_b) + h_-^2 \cos(2\phi_b + 2\Omega t)$  the magnetic potential arising due to the magnetic torque density acting onto the anisotropic cross section of the two chains in a ribbon.  $h_+$  and  $h_-$  are rescaled left and right circularly polarized magnetic field amplitudes. The prefactor  $\Delta\chi$  in front of the magnetic potential denotes the anisotropy (the difference between the two eigenvalues) of the effective susceptibility of the cross section of the ribbon and  $h_+$  and  $h_-$  are rescaled magnetic fields. The last term in the functional denotes the torsional rigidity term. Following the ideas of Kapitza [91, 114, 115], we decompose the local orientation into a fast and a slow component  $\phi_b = \phi_s + \phi_f$ , expand in terms of the fast component and equate the resulting terms of the fast components and the time averaged slow components. This results in a time averaged equation of the slow component of the form  $\partial \phi_s / \partial t - \partial^2 \phi_s / \partial x^2 = -dU_{eff} / d\phi_s$  with an effective potential of the form  $U_{eff} = |\sin \phi_s| + \Delta\chi(2h_+ h_- \cos(2\phi_s) - h_+^2 h_-^2 \cos(4\phi_s)) / 4\Omega$ . The slow component tends to stay within the minima of the effective potential, while the fast component will algebraically vanish with increasing frequency, reducing fluctuations around the average orientation at large frequencies.

Fluctuations render the time averaged cross section more isotropic. We hence expect the effective anisotropy to increase with frequency. The anisotropy of the susceptibility also results self-consistently from depolarization fields of neighboring cross sections in the ribbon. When applying an elliptical external magnetic field with the major axis normal to the plane, then the eccentricity of the magnetic moment will be enhanced for an upright orientation of the ribbon and reduced for a horizontal orientation. Both effects lead to a self-consistent stabilization of the upright orientation at high frequencies respectively to a stabilization of the lying orientation at lower frequencies. This behavior can be modelled by anisotropy of the susceptibility that increases with frequency, which shifts the global minima from  $\phi_b = 0$  toward  $\phi_b = \pi/2$  with frequency. Whether the effective potential exhibits minima at one or at both locations decides whether the domain walls are  $\pi$ -walls respectively  $\pi/2$ -walls. For

very high frequencies the effective force and the fluctuations around the minima are too weak to overcome the barrier between two minima separated by  $\pi$  and the ribbon is forced into the fully upright conformation, where no propulsion is possible.

We have, beside the propulsion of the ribbon, noticed one very interesting features that occurs in our system. For the system of long ribbons, twist will generate domain walls, where domain walls will appear with certain and stable wave length depending on the frequency of the external magnetic field (black squares in Fig. 5.2.6). Here the wave length of the twisted ribbons is defined as the distance between two domain walls traveling through the ribbon. As one can see from Figure 5.2.6 (black squares) wave length will slightly decrease with increase in the frequency of the external magnetic field. Exceptions of this behavior are the wave lengths for the ribbons at frequency of 12 and 13 Hz where the wave length is higher than the wave lengths for the higher frequencies. Partially this will occur for wave lengths at 28 and 30 Hz but in this case wave length is in the boundaries of the average wave length in the range from 14 Hz until 28 Hz. Besides this stable propulsion we have noticed interesting behavior for the frequencies in the range between 14 Hz and 25 Hz (red circles and blue triangles in the Fig. 5.2.6) which is very pronounced for the frequency between 19 HZ and 25 Hz. These behaviors consist of periodical oscillations of the domain walls. After the stabilization period, in which domain walls can be generated from both side of the ribbon, each new generated wall will appear with different (lower or higher) wave length comparing to the previous one. This wave lengths appear in the regular way, i.e. each domain wall with longer wave length will be followed by the domain wall with shorter wave length as one can see in Figure 5.2.7.

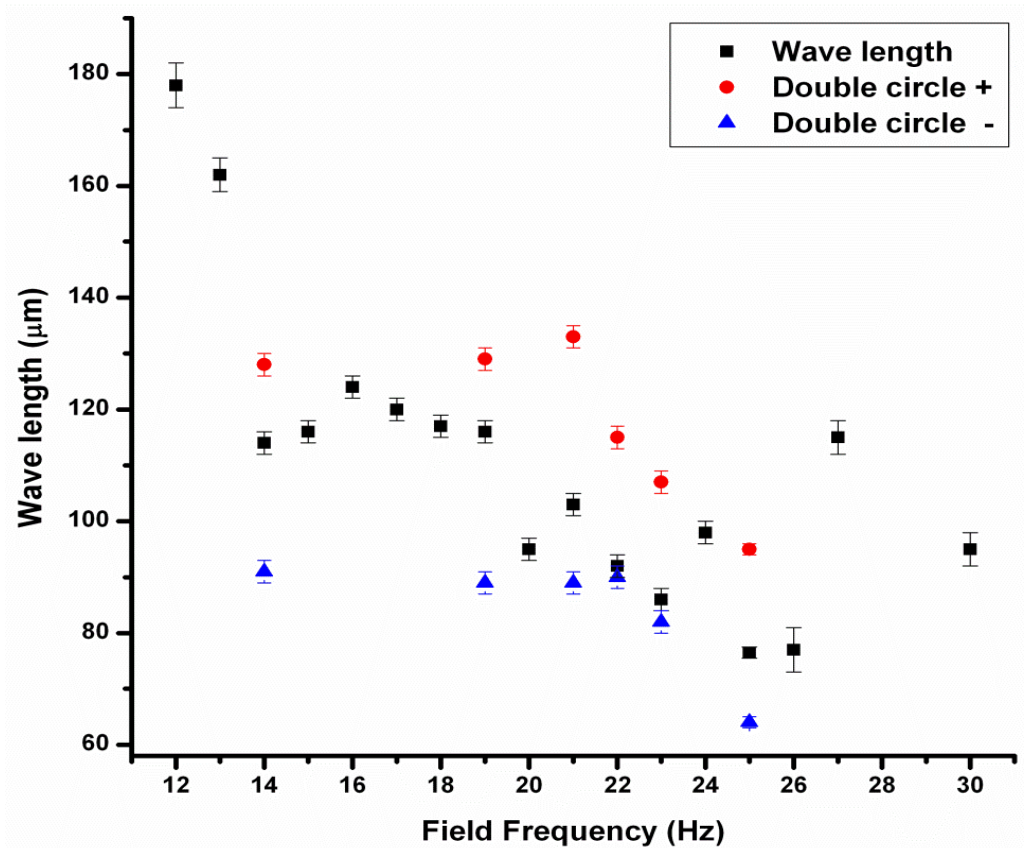


*FIG. 5.2.6:* shows the two different regimes were the wave length between two domains walls depend of the frequency of the external magnetic field. Black squares represent the “normal regime” in which wave length between two domain walls does not change for a given frequency. Blue triangles (shorter wave length) and red circles (shorter wave length) represent the oscillating behavior of the system in which wave length will periodically oscillate around the wave length observed in “normal regime”.

In the Figure 5.2.7 one can see very high regularity in appearance of the domain wall. Following the gray line (which is artificially placed here as a guide for the eye) one can see that always shorter wave length is accompanied with longer wave length. In the Figure 5.2.7 we show the space time plot of the orientation angle  $\phi_b(x,t)$  for a frequency  $\Omega=2\pi \times 27$  Hz. Here one can also see that kinks always come in pairs.

This system is also highly resistive to external perturbation and disturbance. When the system is disturbed, for any reason, in the way that the wave length (shorter or longer) show the deviation from a wave length for a given frequency, the system will experience transformation which will provide the fastest path toward the equilibrium behavior.

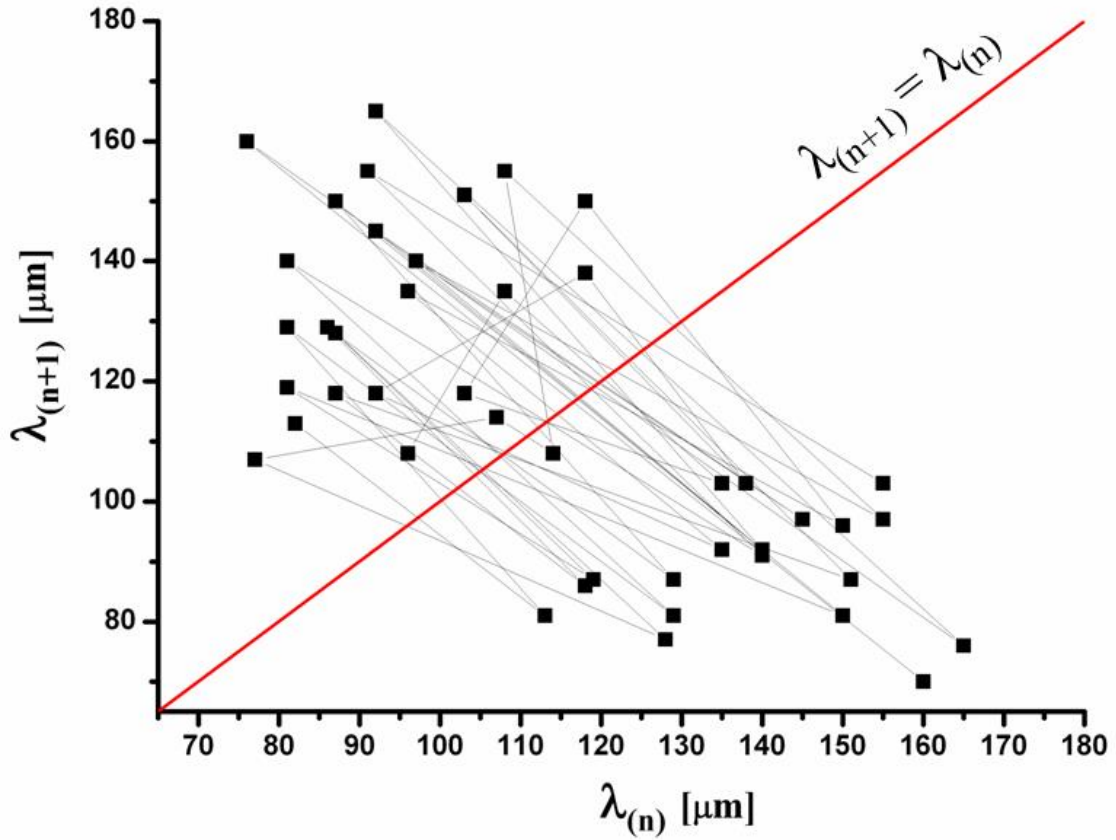


*Fig. 5.2.7: each domain wall with longer wave length will be followed by the domain wall with shorter wave length. Red line and the gray connecting lines serve only as the guide for the eye. Red line divides the areas with the higher concentration of domain walls with the longer wave lengths and areas with the higher concentration of domain walls with the shorter wave lengths.*

When this kind of behavior occurs system will try, in next few cycles (few generated domain walls), to accommodate and return to the “normal” oscillating regime. This change can manifest in producing additional domain wall with very small wave length or by “skipping” one domain wall. The general tendency of the system is to find the fastest way to avoid any disturbance and to return to the normal oscillating regime.

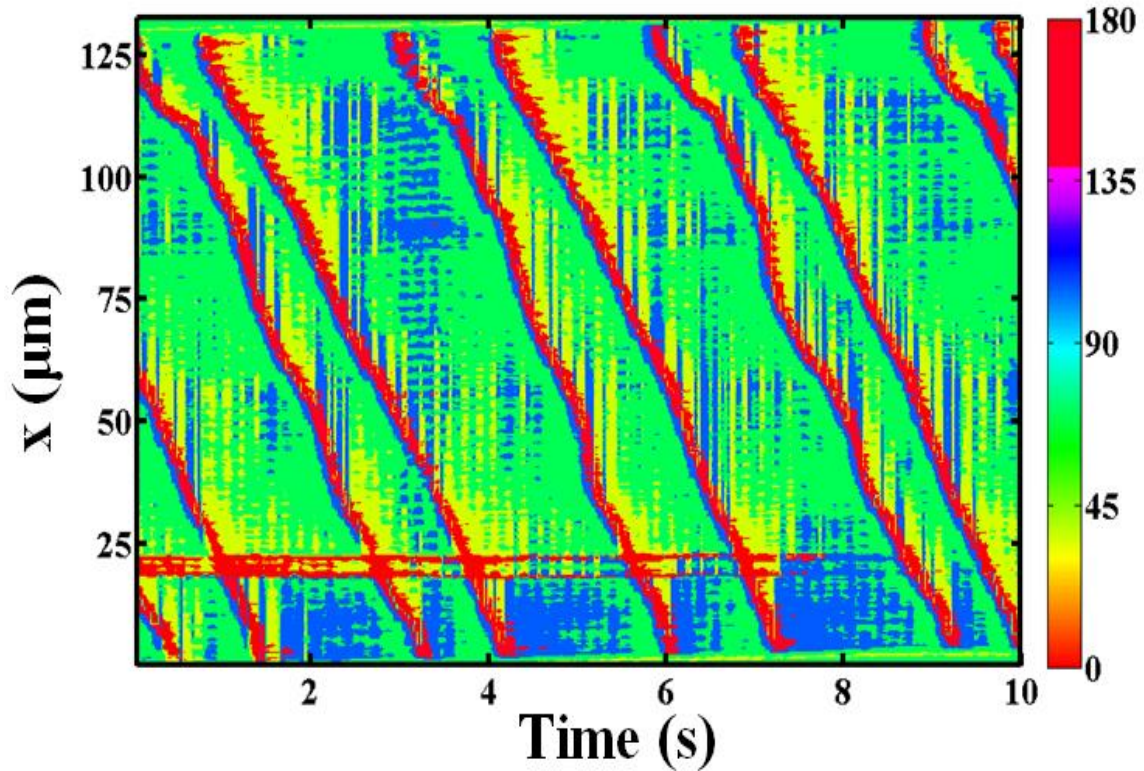
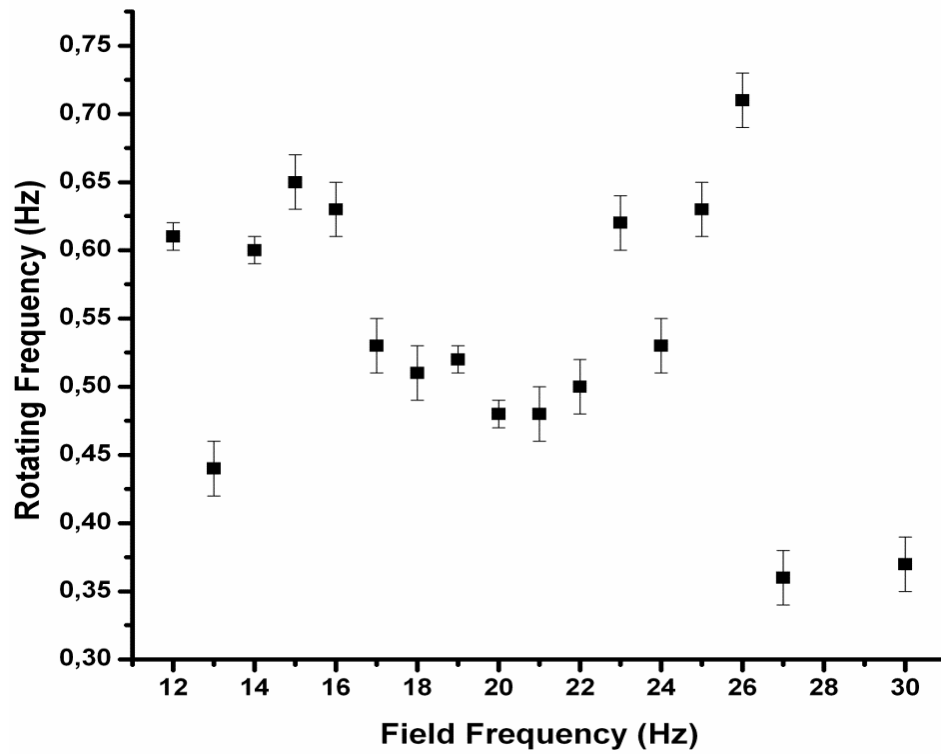


Fig. 5.2.8: space time plot of the orientation angle  $\phi_b(x,t)$  for a frequency  $\Omega=2\pi \times 27$  Hz.

In Figure 5.2.9 we plot frequency of the rotation of the domain walls versus frequency of the rotating magnetic field. One can see a very pronounced U-shape in the same range of the frequency where the oscillating domain walls appear. We do not have a proper theoretical explanation for this very interesting behavior of our experimental system. On the other hand comparing the “normal” and the “oscillation” regime we can propose some empirical conclusions and call for more detailed experimental and theoretical work. We have noticed that in the circumstances when the ribbon is shorter than two wave lengths of the “normal” regime (by “normal” regime we consider traveling domain walls represented by black squares in Fig 5.2.6) system have a high probability of showing “oscillatory” behavior. From the experimental point of view, it looks like the system is trying to generate the domain walls that will travel with the same wavelength, but instead start to generate domain walls which have wavelength smaller and larger than the wavelength in the “normal” regime. These conclusions are purely empirical and demand further experimental measurement and computer simulations.



*Fig. 5.2.9:* we have plotted a dependence of the frequency of the rotation of the domain walls versus frequency of the external magnetic field. One can see very good agreement in the range were U-shape appears and the frequencies where the “oscillating” behavior has observed.

### 5.2.3 Conclusion

In conclusion the interplay between dipolar interactions created by external magnetic fields and gravity forces an ensemble of paramagnetic beads into a ribbon. The twist of the ribbon is a mathematical property of the finite cross section of the ribbon that is absent in slender bodies. It can be controlled by the frequency and the eccentricity of the applied precessing field. The ribbon changes from a flat lying ribbon via travelling twist domain walls toward a standing ribbon. In the frequency regime where domain walls are formed, the ribbon is propelled along its axis. The geometrical efficiency of propulsion scales with the domain wall density. Beside the propulsion efficiency we have shown that for the certain frequency and experimental conditions the system will experience “oscillatory” behavior. The domain walls with alternating wavelengths will travel through the ribbon. Few do not have a proper theoretical explanation for this “oscillatory” behavior, but from experimental observation, we strongly believe that the length of the ribbon has a crucial role which will generate oscillating domain walls traveling through the ribbon. For more detailed and theoretically sustained explanation there is a need to perform further experimental measurements and computer simulations.

## 5.3 Healing of the ribbons, frequency and eccentricity dependent colloidal structures

In Chapter 5.1 we have studied the behavior of 1D chains of paramagnetic particles in an external rotating magnetic field. We show that a sudden switch from low to high Mason number will increase the elasticity of the chain and prevent degradation of the chain. In Chapter 5.2 we extended this approach to a ribbon that can perform propelled motion in a rotating magnetic field perpendicular to the x-y plane. In this chapter we will show methods that were used in the process of the ribbon healing. Also we will show that depending on the field frequency and eccentricity of the field, one can realize different structures that scale from single chain up to compact tubes and clusters. We apply a circular magnetic field normal to the y-z plane and vary eccentricity of the field in the z direction. More detail about the experimental setup can be found in Chapters 4.3 and 6.2.3.

This chapter is divided in two parts. In the first part we will present methods of the healing of the ribbons which are later used in the experiments presented in Chapter 5.2. In the second part we will show how we can manipulate self-assembly of the paramagnetic particles by simple change in the frequency and eccentricity. In this second part we will show how the system can be expanded and compressed between two different states. The results presented in this chapter are still in preparation and will be submitted soon.

### 5.3.1 Introduction

Self-assembly offers an elegant way to assemble, disassemble, move and change particle interactions in order to obtain full control over different experimental arrangements. Movement of bacterial flagellae where hydrodynamic friction converts rotational motion of the helix into propulsion along its axis [75] has been a motivation to realize different systems which accomplish efficient propulsion. One of the ways in which to realize systems that can perform propulsion motion is linking DNA particles together [60] by polymer linkage [18], connecting the particles with different diameter by DNA [78] etc. These systems show very nice results but the main disadvantage is that they cannot be changed or adjusted depending on the requirements of the desired systems. Once assembled the systems cannot be changed. Almost all systems in nature demand adaptability and changeability depending on the experimental tasks. This

feature is especially pronounced for the processes taking place in the biological systems and living organisms.

Using bottom-up concepts we are able to achieve the desired conformation of the system by simple change in the field frequency and eccentricity. We are able to realize a system which can be fully controlled externally in a predictable way. We show that the transient dynamics induced by switching the field frequency and eccentricity enable the ribbon to compress and expand between two equilibrium states. This behavior is governed by interaction between the viscous and magnetic torque.

### 5.3.2 Assembling and healing of colloidal ribbon

Preparation of the samples used in this experiment consists of adding the samples to a Petri dish, sedimentation of particles, and application of a field of particular strength. Specific configurations are described in Chapter 6.2.3. When particles were sedimented above a glass surface an external static magnetic field was applied in the x-axis direction. Due to the induced dipole moment, particles were organized into chains of paramagnetic particles parallel to the lines of the magnetic field (direction of x-axes). To organize chains into the ribbons and more complex structures we applied a dynamic magnetic field with field lines parallel to the direction of the y-axis. Application of the magnetic field parallel to the direction of the y-axis will result in attraction between different chains and single particles. As a consequence single chains will attract each other laterally. This lateral attraction will lead to the formation of two or more chains ribbons. In our experiments we are interested only in ribbons that consist only two connected single chains. We develop a technique which allows us to heal ribbons that have particles in three and four chains. After healing, we apply a magnetic field in the direction of z-axes, creating a rotating magnetic field in the y-z plane (Chapter 5.2). For the sake of clarity, a description of the healing process will be divided into four consecutive steps. In all of these four steps we use a time-dependent magnetic field  $(t) = \widehat{H}(\cos \theta_{ext}e_x + \sin \theta_{ext}\sqrt{2(1 - \epsilon)}e_y \cos(\Omega t) + \sin \theta_{ext}\sqrt{2(1 + \epsilon)}e_z \sin(\Omega t))$ , characterized by the four parameters of field strength  $\widehat{H}$ , the precession angle  $\theta_{ext}$ , the eccentricity  $\epsilon$  and the angular frequency  $\Omega$ . The circular modulation corresponds to  $(\theta_{ext} = 26^0, \epsilon = 0)$  and the elliptic modulation to  $\theta_{ext} = 26^0, \epsilon = 0.5$ . The formation and healing happened in four steps:

**STEP 1: CHAIN FORMATION**

The first step is the assembly of colloidal chains in a static field along the  $x$ -direction. We used  $\hat{H} = 2000$  A/m,  $\theta_{ext} = 0$ ,  $\epsilon = 0$  and  $\Omega/2\pi = 0$ . Figure 5.3.1 show formation of 1D particle chains. Formation of these one dimensional chains is a well-known and widely explored topic and more details can be found in Chapter 2. Area in the pictures that are marked with red ellipses point to the characteristic events. In Frame a) the red ellipse points to the chains and particles that will form longer chains in the next frame (Frame b)). The same principle is than applied for all other frames, from b) till f).

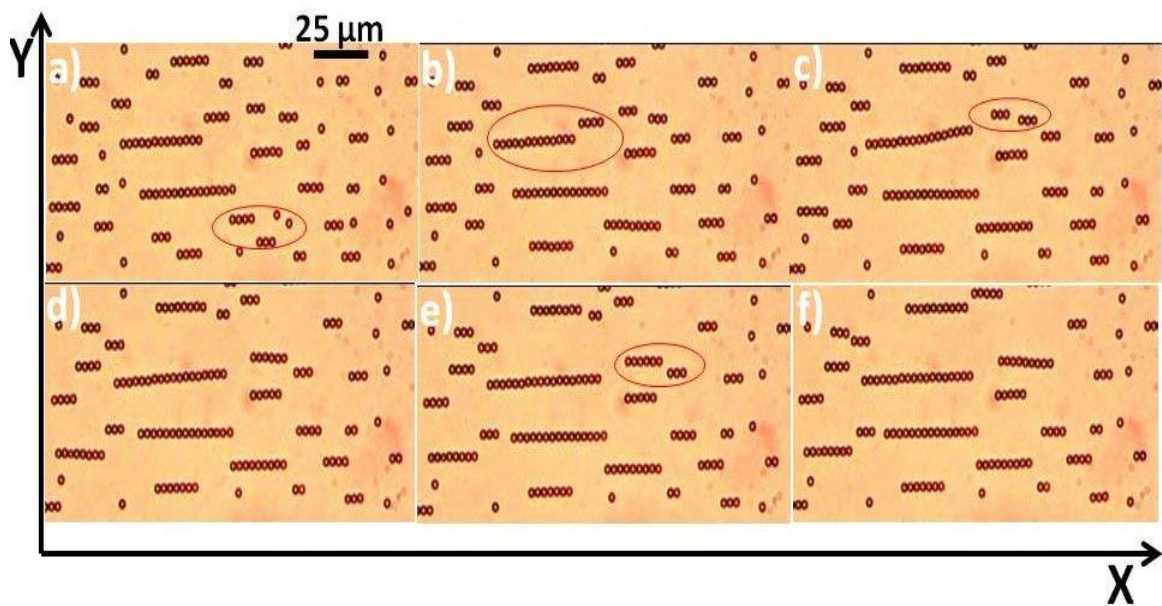


*Fig 5.3.1: Formation of 1D chain of particles in the direction parallel to the direction of the external static magnetic field ( $x$ -axes). Area in the pictures, that are marked with red ellipse, point to the characteristic events were shorter chains and particles will rejoin and form the longer chain.*

**STEP 2: RIBBON FORMATION**

The second step is the assembly of a ribbon with defects from the chains. Ribbons can be formed using two alternative methods or combinations of them. Which methods are used depends of the local concentration of the particles. The local concentration of particles is defined as the concentration of the particles in the field of view of the CCD camera. Figure 5.3.1 shows the situation in which we have high concentration of the particles. One can see that particles are relatively close to each other and densely packed.

## 5 Experimental results

If the local concentration is high enough we use  $\hat{H} = 2200 \text{ A/m}$ ,  $\theta_{ext} = 26^\circ$ ,  $\epsilon = -1$  and  $\Omega/2\pi = 15 \text{ Hz}$ . This modulation leads to an attraction of the librating chains and ribbons are formed. In Figure 5.3.2, frames a) and b), one can see the librating chains ends. Frame c) shows diffusion of shorter chains toward longer one. In the frame d) the chain that is marked with a red ellipse shows the characteristic event. In the next frame (frame e)) this chain will rejoin a longer chain and it will form a ribbon at the end of the chain. The same principle is applied for frame e). In frame e) the chain that is marked with green ellipse began to diffuse toward a longer chain and would have formed a ribbon in a longer experiment. In contrast to this chain, the two chains marked with black ellipses are too far apart from the longer chain and were not attracted toward the longer chain. In this case we apply the same procedure, as we use for low local concentration of the particles which is described below.

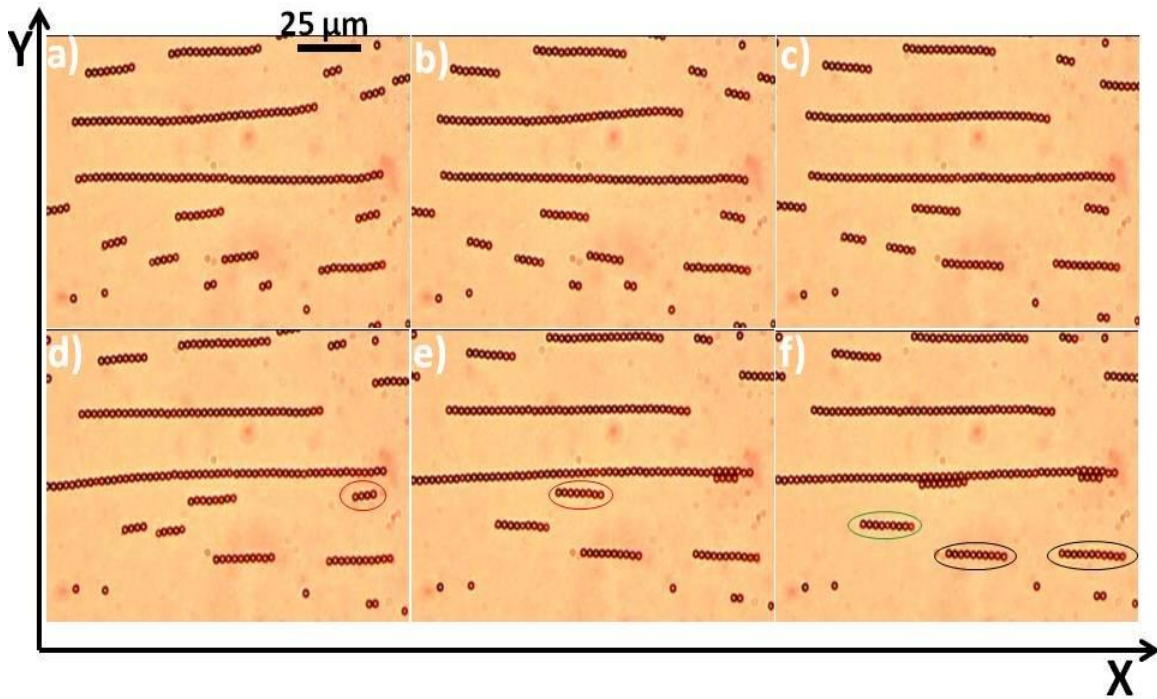


*Fig 5.3.2: Preparation of the ribbon at  $\hat{H} = 2200 \text{ A/m}$ ,  $\theta_{ext} = 26^\circ$ ,  $\epsilon = -1$  and  $\Omega/2\pi = 15 \text{ Hz}$ . Frame a) and b) show librating of the chains ends. The chains marked with red ellipse will rejoin with longer chain next frame (frame e)) and it will form ribbon at the end of the chain. The same principle is applied for the frame e). Chain marked with green ellipse can diffuse toward longer chain and form a ribbon. This time exceed the time of our experiment. Two chains marked with black ellipse are too far apart from the longer chain and they will not be attracted toward the longer chain.*

This precessing field lets the chains roll in the y-direction. The speed of rolling is higher for shorter chains than for longer chains such that shorter chains catch

up with the longer chains. First using a precessing field ( $\epsilon = 0$ ) two chains roll at different speeds and come into the range of attraction after which we switch to  $\epsilon = -1$  and the librating chains attract and form a ribbon. After step 2 we obtain ribbons consisting of several chains with lots of defects.

### **STEP 3: RIBBON FRAGMENTATION AND SEGMENT HEALING**

In the Figure 2.2.2.3, frame a), the area marked with red ellipse shows one of the ribbons that needs to be healed in order to obtain a ribbon that consists only of two chains. To fragment the ribbon we use a field with  $\hat{H} = 2370$  A/m,  $\theta_{ext} = 32.5^\circ$ ,  $\epsilon = 0.38$  and  $\Omega/2\pi = 15$ Hz. Fragmentation of the ribbon is shown in Figure 5.3.3 in the frames b)-f). The ribbon fragments into separate segments along the x-direction that periodically realign. During this process individual segments heal into short, mainly two chained ribbons.

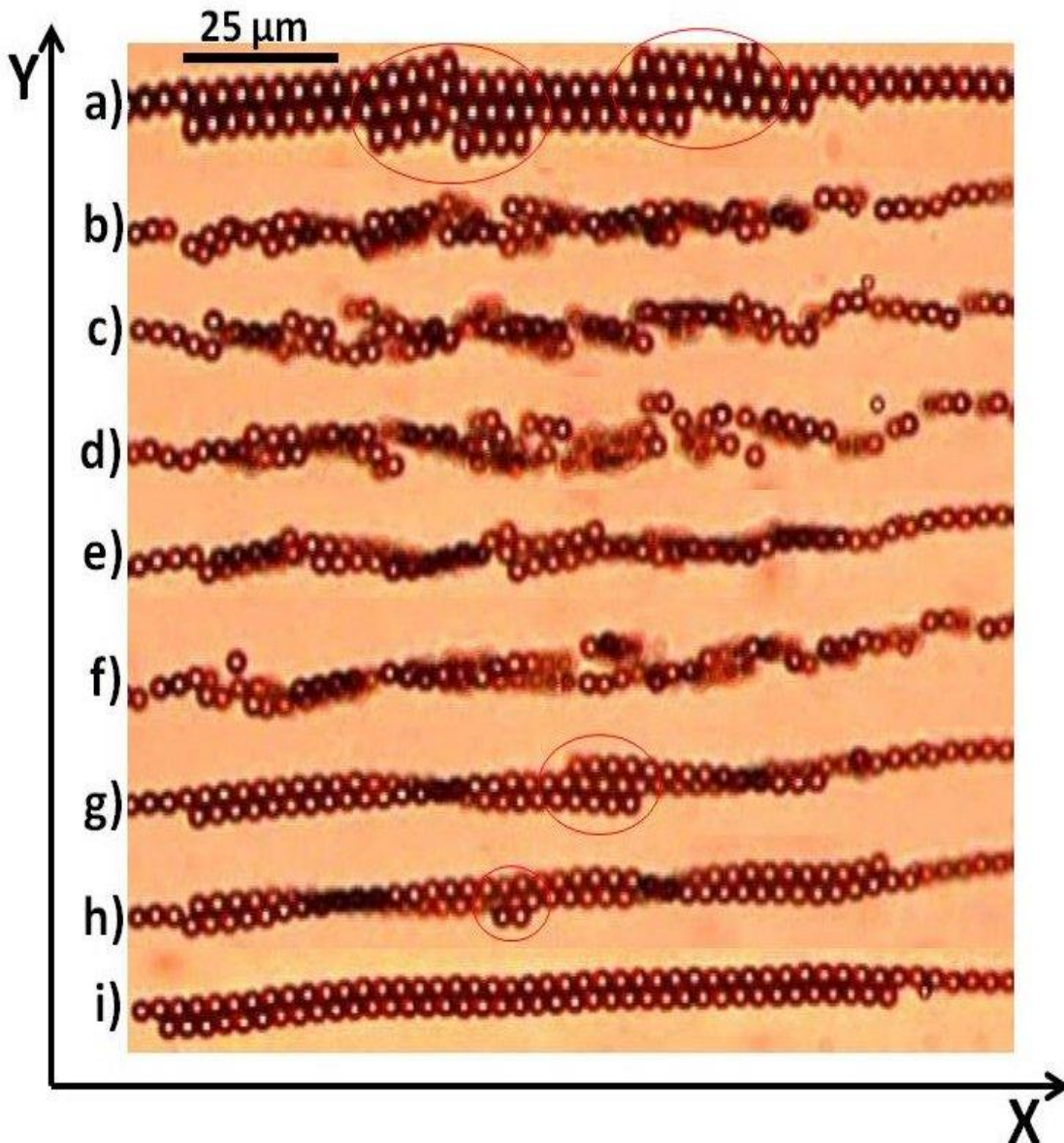


*Fig 5.3.3: Frames from b) until f) show the fragmentation of different defect ribbons into segments of two chained ribbon segments. Frames g) and h) show ribbons with the smaller defects than the ribbon in frame a). A completely healed ribbon is shown in frame i).*

#### **STEP 4: SEGMENT COALESCENCE**

To coalesce two chained segments into a long two chained ribbon we use a field with  $\hat{H} = 2200$  A/m,  $\theta_{ext} = 26^\circ$ ,  $\epsilon = 0$  and  $\Omega/2\pi = 15$  Hz. In this field the two chain segments rebind to form a longer ribbon. On most occasions the coalescence of two chain segments does not create defects. In Figure 5.3.3, frames g) and h) show ribbons with smaller defects than the ribbon in frame a). To heal these defects we repeat steps 3 and 4. A completely healed ribbon is shown in frame i).

The healing process is recommendable for magnetic field frequencies between  $11 \text{ Hz} < \Omega/2\pi < 18 \text{ Hz}$ , where fragmentation is possible. Above 18 Hz clusters form instead of ribbons. For frequencies between  $18\text{Hz} < \Omega/2\pi < 30 \text{ Hz}$  formation and healing of the ribbons is also possible. Contrary to the process that takes place in the frequency range below 18 Hz, healing of ribbons above 18Hz can experience many difficulties which we will explain in more detail in Chapter 5.3.3.

### 5.3.3 Compression and expansion with self-assembled paramagnetic particles structures

To assemble the chains and ribbons we repeat the procedure presented in steps 1 and 2 described in Chapter 5.3.2. In all of the steps performed and described in this chapter we use the same time dependent magnetic field given as:  $\mathbf{H}(t) = \widehat{H}(\cos \theta_{ext} e_x + \sin \theta_{ext} \sqrt{2(1-\epsilon)} e_y \cos(\Omega t) + \sin \theta_{ext} \sqrt{2(1+\epsilon)} e_z \sin(\Omega t))$ . The applied field is characterized by the four parameters of field strength  $\widehat{H}$ , the precession angle  $\theta_{ext}$ , the eccentricity  $\epsilon$  and the angular frequency  $\Omega$ . The circular modulation corresponds to  $(\theta_{ext} = 26^\circ, \epsilon = 0)$  and the elliptic modulation to  $\theta_{ext} = 26^\circ, \epsilon = 0.5$ .

For frequencies below  $\Omega/2\pi = 18 \text{ Hz}$  (Fig 5.3.4 shows the ribbon assembled at the frequency  $\Omega/2\pi = 15 \text{ Hz}$ ), which is the frequency used for the healing of the ribbons, we were able, by changing the eccentricity of the magnetic field in direction of z-axis ( $0.3 < \epsilon < 0.5$ ), to achieve a transition from a ribbon that consists of particles in the third and fourth row (Fig 5.3.4 a)) to a single chain (Fig 5.3.4 j)) by simply changing the eccentricity of the magnetic field. In Fig 5.3.4 frame a) shows the unhealed ribbon with particles in the third and fourth row. Here we have a similar situation as we had in Chapter 5.3.2 where we showed how to heal the ribbon.

Frames from b) until d) show the behavior of the chain for a value of the eccentricity of  $\epsilon = 0.3$  slightly above 0.3. For these experimental conditions one can see that almost all the chains from the third and fourth row are healed. Frames from e) until h) show the behavior of the chain for the value of the eccentricity of  $\epsilon = 0.5$ . Here ribbon will break in to a smaller ribbons, but this smaller ribbons will not diffuse far from chain and by reducing  $\epsilon$  from  $\epsilon = 0.5$  to  $\epsilon = 0.3$  smaller ribbons will again rejoin to a long ribbon. Breaking of the long ribbon and rotation of this smaller part will allow the particles to reorganize their positions in the ribbon. In this way particles will prefer to align with the field in the direction of x-axis rather that with the field in the direction of y-axis.

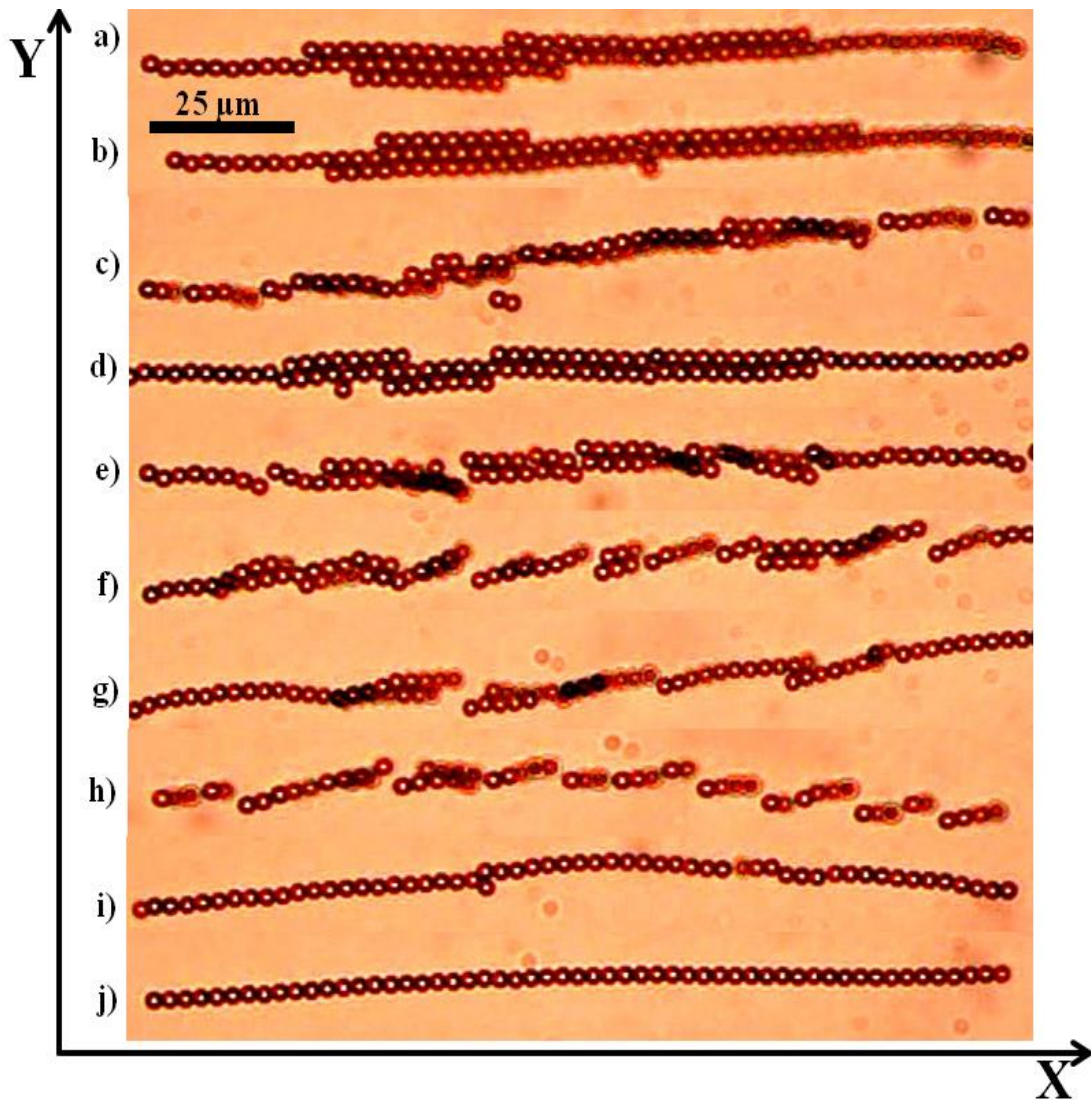


*Fig. 5.3.4:* Shows the ribbon assembled at the frequency  $\Omega/2\pi = 15$  Hz. Frame a) show the unhealed ribbon with particles in the third and fourth row. Frames from b) until d) show the behavior of the chain for the value of the eccentricity of  $e = 0.3$  slightly above 0.3. Frames from e) until h) show the behavior of the chain for the value of the eccentricity of  $e = 0.5$ . Here ribbon will break in to a smaller ribbons, but this smaller ribbons will not diffuse far from chain and by reducing  $e$  from  $e = 0.3$  to  $e = 0.5$  smaller ribbons will again rejoin to a long ribbon. Frame i) shows the single chain with only one particle in the second row. Frame j) shows the single chain completely cleaned from any defects.

This behavior will result in migration of the particles and dissolution of the ribbon into single chains of particles. After some time all particles will be only in the form of single chains which are parallel with the direction of the x-axis. In the case when eccentricity is higher than  $e = 0.5$  ribbons can be destroyed completely where the particle can move from the position of the ribbon permanently. In this situation any reductions in eccentricity lower than  $e = 0.3$  cannot return these particles to the initial long ribbon. In this case particles will continue to move as independent objects. Frame

i) shows the single chain with only one particle in the second row. Frame j) shows the single chain completely cleaned from any defects.

Contrary to the behavior of the system for the frequency  $\Omega/2\pi = 18$  Hz where unhealed ribbons will dissolve into two chain ribbons and further to single chains, for the frequency above  $\Omega/2\pi = 18$  Hz (up to  $\Omega/2\pi = 30$  Hz which was the limit of our measurement) unhealed ribbons will cluster. This behavior can be seen on the two consecutive figures (Fig 5.3.5 and Fig 5.3.6) which present the transition of the ribbon assembled at the frequency  $\Omega/2\pi = 28$  Hz. Frame a) shows the unhealed ribbon with only one particle in the third row. Frames b) to e) show the behavior of the chain for values of the eccentricity from  $\epsilon = 0.3$  to  $\epsilon = 0.5$ . Ribbons will perform rotational motion and particles will reorganize into the direction of the y-axis. During this motion particles form the chains in the third and the fourth chain. Further rearrangement of the particles always happened in the direction of the populating and healing the impurities in the third, fourth and consecutive rows. For example if there is an empty space between the particles in the third row (in order that 2-4 particles are missing to complete the third row), particles will first try to reorganize and heal this impurity before starting to form a new row. By increasing the eccentricity of the system to the value of  $\epsilon = 0.5$  we can more quickly rearrange the particles in the ribbon. Frames from f) until j) show the further clustering of the particles for the eccentricity  $\epsilon = 0.5$  until they reach a stable conformation. In this system this stable conformation is a cylinder or tube which consists of 4-5 single chains. This cylinder will perform very stable propulsion motion for eccentricities between  $\epsilon = 0.2$  and  $\epsilon = 0.5$  without any new reorganization in the existing cylinder. Reorganization can occur only in the parts of the ribbon outside the cylinder. The next figure (Fig 5.3.5) is a continuation of the same movie. Frame k) shows the cylinder that performed rotation motion in the Fig. 5.3.5 g) until Fig. 5.3.5 j) when  $\epsilon = 0.5$ . If we increase the eccentricity of the field from  $\epsilon = 0.65$  to  $\epsilon = 0.75$  we are able to break the cylinder. Now the particles will detach from the cylinder and try to reorganize in the direction parallel to the x-axis. This behavior can be seen in frames l) to n). Frames o) to r) show consecutive steps of the cylinder reorganization. For these frames we reduced  $\epsilon$  from  $\epsilon = 0.65$  to  $\epsilon = 0.55$ .

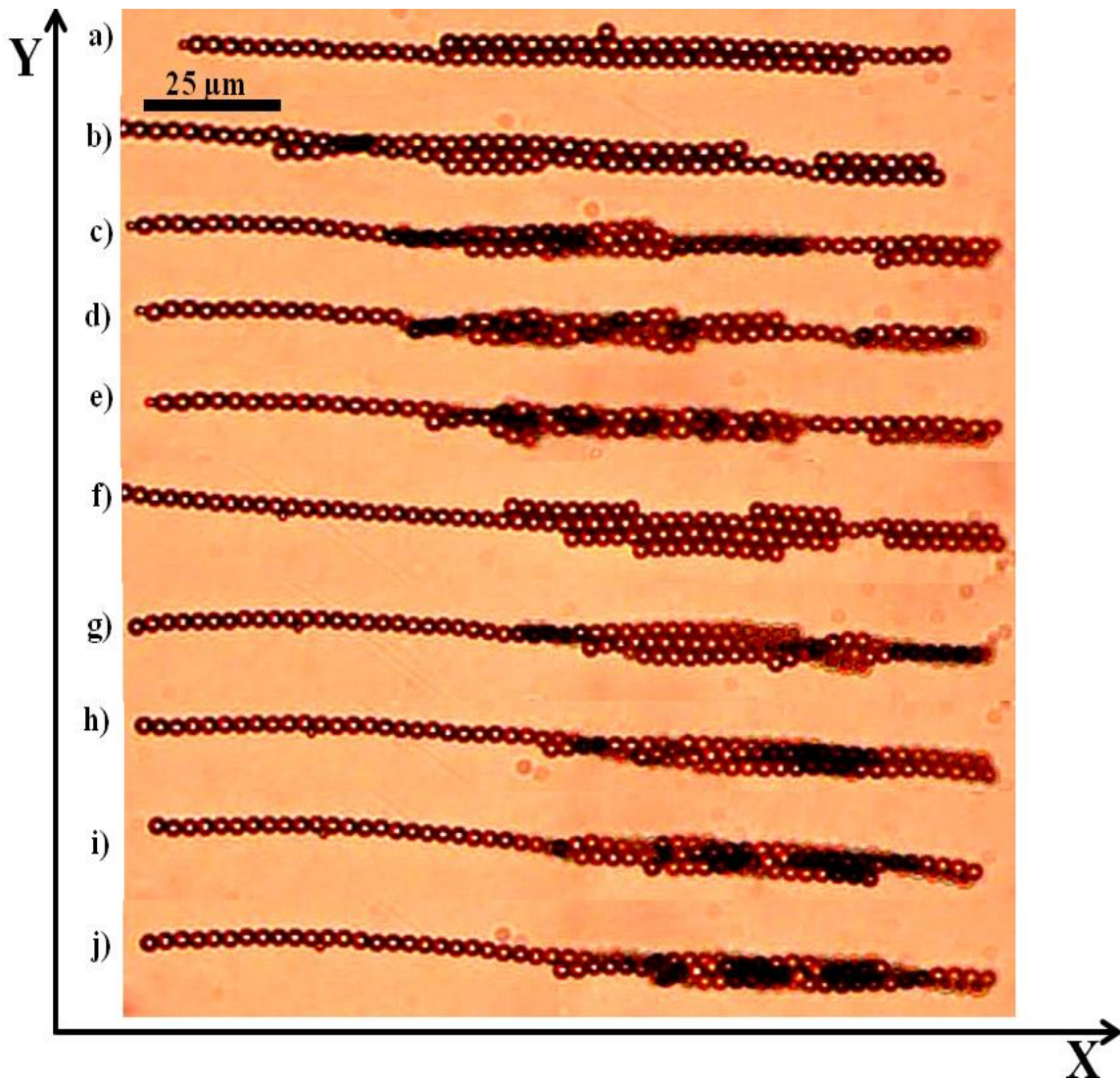


*Fig. 5.3.5:* Shows the ribbon assembled at the frequency  $\Omega/2\pi = 28$  Hz. Frame a) show the unhealed ribbon with only one particle in the third row. Frames from b) until e) show the behavior of the chain for the value of the eccentricity from  $\epsilon = 0.3$  until  $\epsilon = 0.5$ . Frames from f) until j) show the further clustering of the particles until they reach stable conformation and the value of the eccentricity was  $\epsilon \approx 0.5$ . In this system this stable conformation is a cylinder or tube which consists out of 4-5 single chains. This cylinder will perform very stable propulsion motion without any new reorganization in the existing cylinder. The next figure (Fig 5.3.5) is a continuation of the same movie.

Each step between these frames was realized with eccentricity from  $\epsilon = 0.65$  to  $\epsilon = 0.75$ . Frame r) shows the almost healed ribbon which performs propelling motion. Frame s) shows the almost healed ribbon with only two particles in the third row.

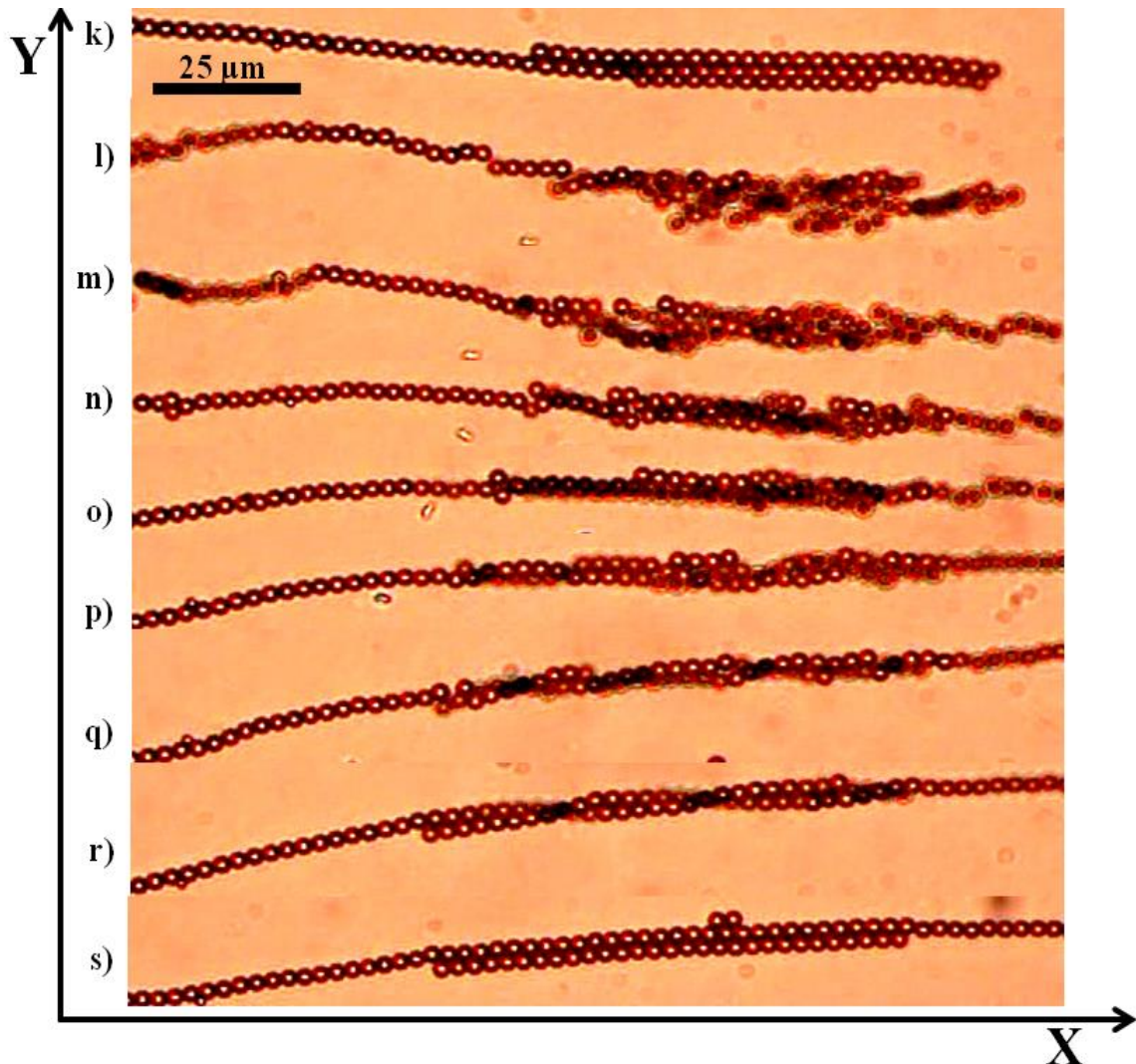


*Fig. 5.3.6:* Shows the ribbon assembled at the frequency  $\Omega/2\pi = 28\text{Hz}$ . Frame k) show the cylinder that performed rotation motion in the Fig. 5.3.5 g) until Fig. 5.3.5 j) when  $\epsilon = 0.5$ . Frames from l) until n) show the behavior of the chain for the value of the eccentricity of  $\epsilon = 0.75$  were cylinder start to break and particles start to reorganize. Frames from o) until r) show consecutive steps of the cylinder reorganization. For this frames we reduce  $\epsilon$  from  $\epsilon = 0.65$  to  $\epsilon = 0.55$ . Each step between this frames was realize with eccentricity = 0.75. Frame r) shows the almost healed ribbon which performs propelling motion. Frame s) shows the almost healed ribbon with only two particles in the third row.

As mentioned previously, ribbons can also be healed at frequencies above  $\Omega/2\pi = 18\text{ Hz}$  as shown in Fig 5.3.5 and Fig 5.3.6. Nevertheless, the healing procedure for this range of frequency has several difficulties. The system is very unstable for all eccentricity bellow  $\epsilon = 0.2$  and especially when eccentricity is reduced to  $\epsilon = 0$ . In this range the system starts to cluster very quickly and switching to  $\epsilon = 0$  can result in destruction of already healed ribbons and defects in the third and fourth row. Compared to the healing process performed for frequency below  $\Omega/2\pi = 18\text{ Hz}$  this system is much

harder to control and direct. Also this system can more easily cause the destruction of the whole structure of the system below  $\Omega/2\pi = 18$  Hz. This behavior can be explained in the following way. Forming the chains in third, fourth and higher rows particles are further from the line that goes through the center of the structure. By applying high eccentricity of the field in the direction of the z-axis particles can be easily pushed out of the imaginary phase space and reducing the eccentricity will not bring them back into the ribbon structure. Instead of rejoining with the primary structure these particles will reorganize and form a completely new structure. For this reason, we recommend that healing procedures are performed at frequencies lower than  $\Omega/2\pi = 18$  Hz.

### 5.3.4 Conclusion

In conclusion we have shown that our colloidal system can perform different types of behavior depending on the frequency and eccentricity of the external magnetic field. We have shown how we can successfully heal the system and remove all defects from the system. By changing the eccentricity of the field we were able to reorganize the unhealed ribbons into the healed ones. By further changing the eccentricity we were able to transform the system from the ribbon into the single chain and into the cluster by simple change in the field frequency and eccentricity. By changing these parameters we could expand and compress the ribbon. By expansion and compression we can draw the system from single chain to the cylinder which can perform very stable rotational motion. This process is reversible and can be completely controlled externally, which makes this system a very good candidate for further research in the field of dynamic self-assembly.

# 6 Materials and Methods

In Chapter 6, we will give an overview of all materials and methods that has been used in all experiments performed during the work on this thesis which are described in Chapter 5. Here we will extend the short overview of experimental setup presented in the Chapter 4. In particular we will present a short description of all instruments that have been used such as polarization microscope, wave generator, etc., scheme of the experimental setup with parameters that have been used to achieve experimental results. Some of the steps involved in the preparation are common to more than one experiment and these steps will be outlined specially. We have also outlined some of the imaging techniques used to extract results.

## 6.1 Materials

### 6.1.1 Paramagnetic colloidal particles and ferrofluid droplets

Paramagnetic colloidal particles, also called superparamagnetic particles, used in this work were 2.8  $\mu\text{m}$  negatively charged polymer “dynabeads”. All paramagnetic particles used in the experiments performed during the work presented in this thesis were purchased from Dynal Invitrogen (Invitrogen Dynal Oslo, Norway) (The name of the company lends the common name of dynabeads for these particles). These particles are highly monodisperse with mean diameter of 2.8  $\mu\text{m}$  and concentration of  $2.8 \cdot 10^9$  beads/ml. The core of the particle contain a small grain of magnetite (5-10 nm in size) coated with polymer shell. The surface of the particles is functionalized with carboxylate groups, which dissociate in water and cause a negative surface charge on the particles. This dissociation will cause repelling force between particles which prevent the aggregation of the beads.

Due to randomness of orientation of small iron grain inside of particles, in the absence of external magnetic field resulting magnetic moment will be equal to zero. When external magnetic field is applied particles will acquire an induced magnetic moment and they will behave as superparamagnetic particles. This means that particles will show no hysteresis or magnetic remanence i.e. for low field strengths, their magnetization is completely reversible and is proportional to the external field through

$\chi_{\text{eff}}$ .  $\chi_{\text{eff}}$  is the effective magnetic susceptibility. In our experiments all field strengths are low enough to be in linear regime of the magnetization curve [25, 33].

To prevent aggregation and to provide additional monodispersity of particles, SDS (Sodium dodecyl sulfate) was added to the original solution. Because of the small iron core these particles will gain an induced dipole moment when they are subjected to an external magnetic field and they will behave like a paramagnet. Consequently, individual particles in an external magnetic field interact via magnetic dipole-dipole interactions.

To be able to create polydisperse liquid droplets (see Chapter 5.1 for detailed experimental use) we used oil based ferrofluid APG-820 from Ferrotec. Ferrofluids are a unique class of material. Ferrofluids are stable colloidal suspension of sub-domain magnetic nano particles (an average size of about 10 nm) in a liquid carrier, coated with a stabilizing dispersing agent (surfactant) which prevents particle agglomeration even when a strong magnetic field gradient is applied to the ferrofluid.

### 6.1.2 Magnetic Field

To create the magnetic field necessary for investigating a wide range of magnetic properties we use a system consisting of three independent custom made coils. These coils are made of 0,5 mm Cu-wire with 950 winding and have a soft iron core or simply an air core depending on the experimental requirements. A system of coils was mounted on an aluminium plate and arranged normal to each other (see Figure 6.1 for details). Two of the coils (x and y coil) create the field horizontal to the x-y plane while the third coil creates a magnetic field perpendicular to the x-y plane. We use static and rotating magnetic field varying directions of fields depending on the experimental requirement. A static magnetic field was realized using DC generator (ET Systems electronic GmbH) LAB/SL 230 AI/LT, 0-30 VDC. A rotating magnetic field was realized with the help of a wave generator (TTi TGA 1244) with a phase difference of  $\pi/2$  between outputs. Voltage and current were controlled and measured using an oscilloscope (Tektronix TDS 2014B). A circularly polarized magnetic field rotating in the x-y plane or the y-z plane (depending of performed experiment) was accomplished by supplying the two amplifiers with the same voltage but with phase difference of  $\pi/2$  between them. Varying the input voltage magnetic field can be made elliptically polarized. The impedance of coils was matched with the impedance of the amplifier (OMNITRONIC €-200).

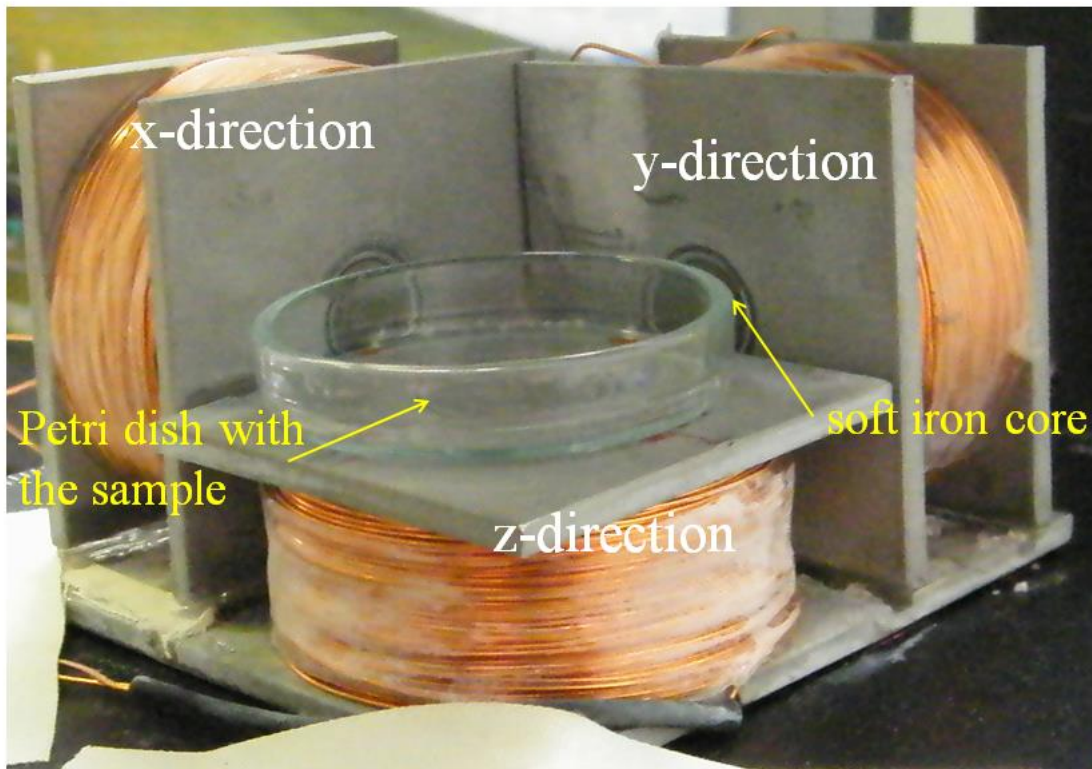


*Fig 6.1: a) Picture of the arrangement of the three perpendicularly orientated solenoid coils with the soft iron core and*

### 6.1.3 Optical Microscopy and video analysis

We used a Leica DM 2500P polarization microscope with polarizer and analyzer (see Figure 6.2 for more details). All videos were recorded with Basler camera (Basler A311fc) on PC. Because real time image analyzing using a PC is not possible in most cases (due to high frame rate of recorded videos). Therefore all videos recorded during experiment are stored in real time on the hard disc of the computer. Videos are analyzed at the end of experiments using frame by frame method with help of software program MatLab. We wrote our custom made algorithm in MatLab to extract all necessary data from the recorded videos. Before processing the data with MatLab, the videos are filtered and treated with other programs for image manipulation such as ImageJ [116], Ulead Video Editor 8 etc. By setting a threshold value we were able to set particles as black points against a white background. A MatLab program is then used to label all connected black areas and determine the center of mass and size.

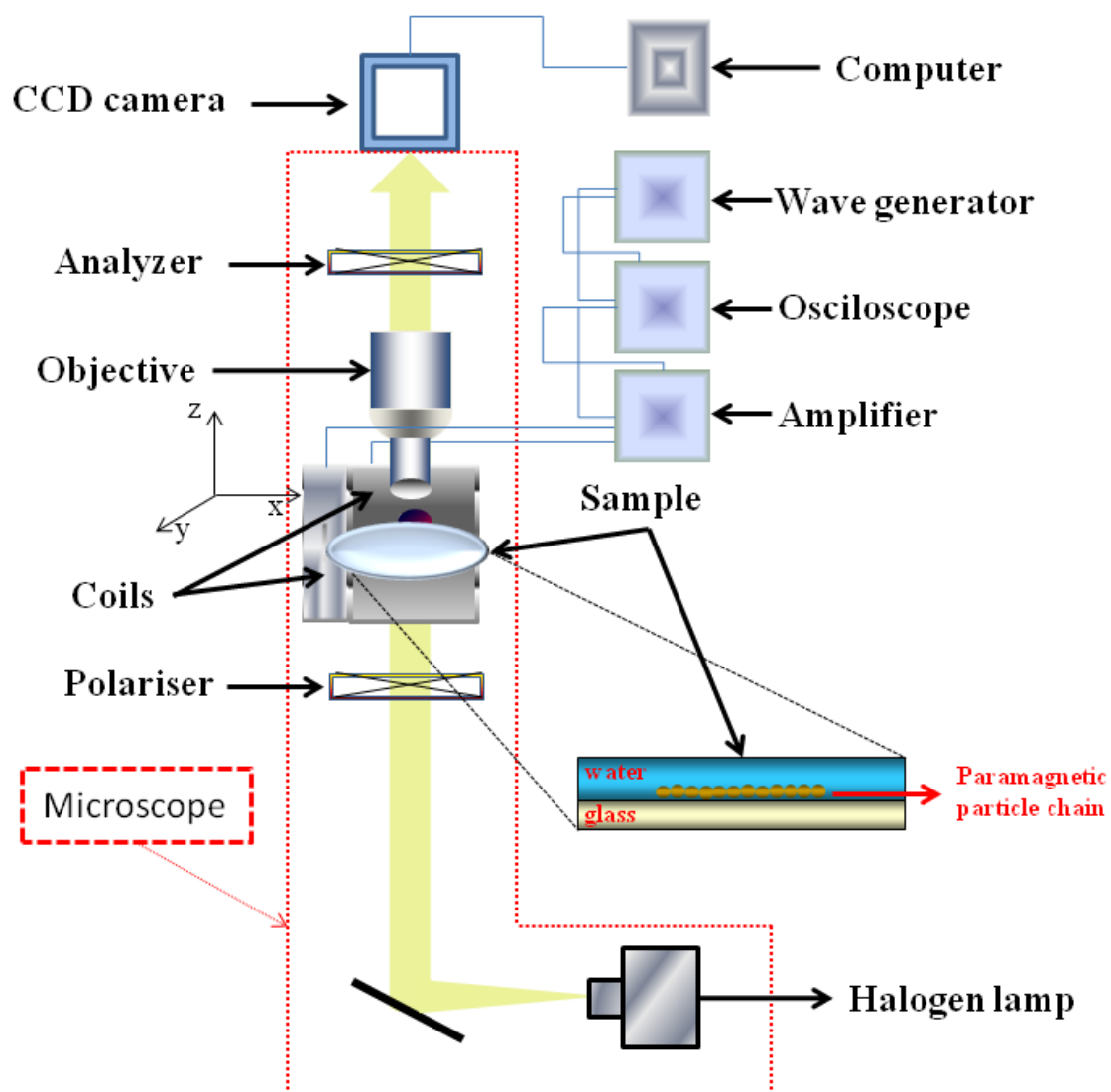


*Fig 6.2: Schematic representation of the experimental set*

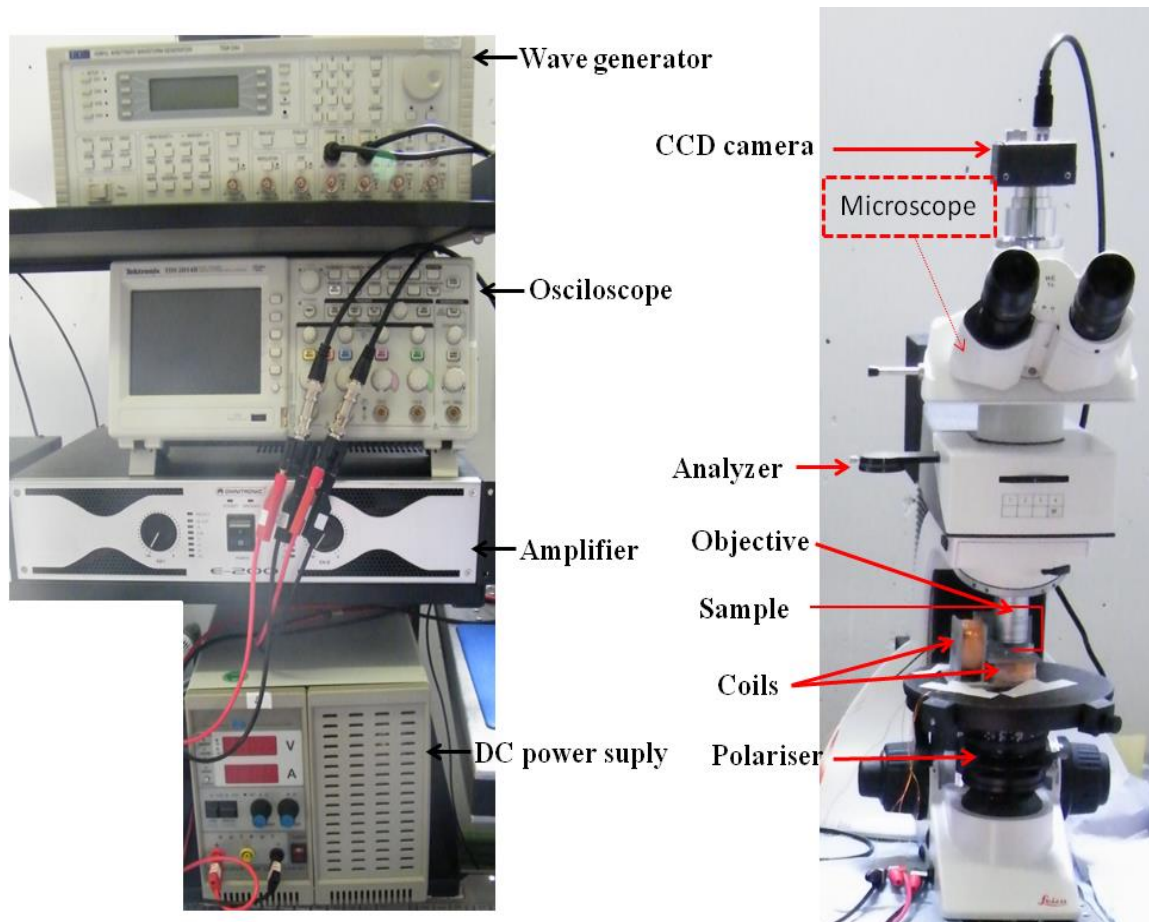


*Fig 6.3: Picture of experimental set up*

## 6.2 Methods

### 6.2.1 Friction-controlled bending solitons as folding pathway toward colloidal clusters

In this chapter we will explain basic experimental procedures used for realizing the experiment presented in Chapter 5.1.

*Sample preparation:* our experiment employs two types of water-dispersed magnetic particles confined by gravity on a solid substrate: paramagnetic colloidal particles (Dynabeads M-270, radius  $a=1.4 \mu\text{m}$ ) (which collapse to the cluster via curling motion) and SDS stabilized ferrofluid droplets (APG-820 Ferrofluid) (which collapse to the cluster via buckling motion). The paramagnetic colloids were diluted in Millipore water ( $5 \cdot 10^{-6}$  beads/ml) while the ferrofluid emulsion was prepared by dispersing 6% by w. of APG into a water solution containing 1.6% by w. of SDS. Using a pipette, a solution of paramagnetic particles ( $\sim 100 \mu\text{l}$ ) was placed in Petri dish previously filled with Millipore water. Particles were, due to gravity, sediment on the bottom of the Petri dish. The glass surface was pretreated with SPP (coating glass surface with PSS was described in details in section 6.2.5). Sedimentation velocity can be calculated from following formula [32]:

$$U_s = \frac{MgD_0}{k_B T (1 - \rho/\rho_p)}, \quad (6.1)$$

where  $M$  is the mass of the particles,  $D_0$  is the particle's diffusion coefficient in water,  $\rho$  is water density and  $\rho_p$  is the density of particles. For the complete sedimentation and equilibrium of particles average waiting time was approximately 15-20 min. In the absence of a magnetic field the lateral arrangement of the particles is a random distribution.

*External magnetic field and optical microscopy:* After sedimentation of particles we apply an external magnetic field in direction of x-axis. Particles acquire induced dipole moment and form chains in the direction parallel to the magnetic field. Formation of the chains is out of crucial importance for our experiment. Necessarily time for the formation of the chains can be express following formula [38]:

$$T_0 \sim \frac{\eta}{\mu_0 M_V^2} \phi^{-5/3}, \quad (6.2)$$

where  $M$  is the particle volume magnetization,  $\phi$  is the volume fraction,  $\mu_0$  is permeability of vacuum and  $\eta$  is the zero-frequency viscosity. Applying dynamic magnetic field ( $\mathbf{H}(t) = H\mathbf{e}_x$ ) in the direction of the x-axis particles will organize in the chains parallel to the lines of the magnetic field. If two chains are close and parallel to each other, they will diffuse toward the closest end of the other chain.

*Experimental procedure and video recording:* when chains reach a certain length ( $\geq 25$  particles) we apply the dynamic magnetic field in the direction of the y-axis with phase difference of  $90^\circ$ , creating the rotating magnetic field in x-y plane ( $\mathbf{H}(t) = H(\cos \omega t \mathbf{e}_x + \sin \omega t \mathbf{e}_y)$ ). Frequency varied in the range from  $\nu=3$  Hz to  $\nu=60$  Hz (see figure Fig 5.1.1). For each frequency we varied the magnetic field from  $H \sim 200$  A/m to  $H \sim 1200$  A/m (see figure Fig 5.1.1). The same procedure was applied in the experiment with SDS stabilized ferrofluid droplets (APG-820 Ferrofluid). All experiments were visualized with the polarization microscope Leica DM 2500P using a 100x oil immersion objective and 0,55x C-mount. Videos were recorded with the help of a digital color camera Basler A311fc at 30 frames per second. More details concerning this experimental results one can find in Chapter 5.1.

## 6.2.2 Dynamic conformations of self-assembled helical ribbons

In this Chapter we will explain basic experimental procedures used for realizing the experiment presented in Chapter 5.2.

*Sample preparation:* We repeat the same procedure of adding the sample to a Petri dish and sedimentation of particles as we described in Chapter 6.2.1.

*External magnetic field and optical microscopy:* when particles were sediment above the glass surface an external static magnetic field in direction of x-axis was applied. When chains reach a certain length ( $\geq 40$  particles) we apply the dynamic magnetic field in the direction of the y-axis with phase difference of  $90^\circ$ , creating the dynamic magnetic field that will induce an attractive force between the chains in the direction of y-axis. Thus we are able to create structures that consist of two chains in direct connection (ribbon). In our experiments we are interested only in ribbons that

consist only two connected single chains. We develop techniques which allow us to heal the ribbons that have particles in the third and fourth chain. These healing techniques were explained in more details in Chapter 5.3.

*Experimental procedure and video recording:* after a ribbon was formed we apply the dynamic magnetic field in the direction of the z-axis with phase difference of  $90^0$ , creating the rotating magnetic field in y-z plane. Ratio between the static and rotating magnetic field is kept in relation 2:1 i.e. the static field is always double the strength of the precessing magnetic field in on order to prevent distraction of the ribbon structure. This ratio was used for all values of the frequency and magnetic field strength used in this experiment. Field modulation was changed from circular magnetic field toward the slightly elliptical magnetic field in the direction of z-axis with increasing frequency value (frequency was varied from  $\nu=11$  Hz to  $\nu=40$  Hz). All experiments were visualized with the polarization microscope Leica DM 2500P using a 50x oil immersion objective and 0,75x C-mount. Videos were recorded with the help of a digital color camera Basler A311fc at 30 frames per second. More details concerning this experimental results can be found in Chapter 5.2.

### **6.2.3 Healing of the ribbons, frequency and eccentricity dependent colloidal structures**

In this chapter we will explain basic experimental procedures used for realizing the experiment presented in Chapter 5.3.

*Sample preparation:* We repeat the same procedure of adding the sample to Petri dish and sedimentation of particles as we described in Chapter 6.2.1.

*External magnetic field and optical microscopy:* when particles were sediment above the glass surface we follow two different ways to build up structures that consists of two, three or more chains in direct connection. The first way is to apply an external static magnetic field in the direction of x-axis and first form single (one dimensional) chains and then apply the dynamic magnetic field in the direction of the y-axis and form ribbons or structures that consist more than two chains. The second way is to apply a static magnetic field in the direction of the x-axis and the dynamic magnetic field in the direction of the y-axis at the same time. In our work we used the first way because it provide a more controlled way to build up structures that have desired length and shape.

*Experimental procedure and video recording:* after we formed structures that have more than two direct connected chains we apply the dynamic magnetic field in the direction of the z-axis with a phase difference of  $90^0$ , creating the precessing magnetic field in the y-z plane. The static magnetic field is always kept stronger than the field in the direction of y- and z-axis. This relation was used for all values of the frequency and magnetic field strength used in this experiment. Field modulation was changed from circular magnetic field toward the elliptical magnetic field ( $\epsilon = 0.3$ ) in the direction of the z-axis. When the ribbon was healed (consists only two single chains connected together) we change the eccentricity of the elliptical magnetic field in the direction of the z-axis to the elliptical magnetic field in the direction of y-axis ( $\epsilon = 0.05-0.1$ ) in order to preserve the ribbon structure. For the frequency up to  $\nu=18$  Hz a ribbon can be successfully healed. For the frequency up to  $\nu=18$  Hz a ribbon can be further dissolved to the single chain applying elliptical magnetic field ( $\epsilon = 0.2-0.5$ ) in the direction of z-axis after the structure is healed to the ribbon. For the frequency between  $\nu=18$  Hz and  $\nu=28$  Hz unhealed structures can be collapse in to the cluster and later stretch to a single chain that can manipulate the eccentricity of the magnetic field in the direction of the z- and y-axis. All experiments were visualized with the polarization microscope Leica DM 2500P using a 50x oil immersion objective and 0,75x C-mount. Videos were recorded with the help of a digital color camera Basler A311fc at 30 frames per second. More details concerning these experimental results can be found in Chapter 5.3.

#### **6.2.4. Preparing the PSS solution**

To prepare the solution of poly sodium 4-styrenesulfonate or short PSS for coating the Petri dish with a thin layer of negative charges we used the following procedure:

1. 100 mg of PSS was dissolved in 20 ml of ultrapure water placed in a tube.
2. 0.58 g of NaCl (0.5 M) was added to the solution.
3. The bottle was sealed and stored to the fridge.

#### **6.2.5. Coating with PSS solution**

With pipette solution of PSS was added to Petri dish in amount that completely covers the bottom of the Petri dish. For successful coating process we applied the following steps:

## 6 Materials and Methods

---

1. The Petri dish was placed horizontally in a sonicator (put name) and sonicated for 15- 20 minutes.
2. The remaining solution of PSS was removed using micropipette.
3. The Petri dish was dried with compressed air and ready for experimental use.

# 7 Summary

We have studied the dynamic self-assembly of paramagnetic micrometer size particles at the solid-liquid interface. Applying conditions where the Mason number is very high we were able to realize the motion of paramagnetic chains and ribbons which have not been previously presented. We have shown that in our colloidal system the kinetics of folding is dominated by friction arising along the slopes of the energy landscape rather than by transitional rates over flat saddle points. The shortest pathway from a pearl chain toward a cluster via the buckling of the chain is suppressed by the friction of relative motion between the adjacent surfaces of the particles and not by the presence of barriers in the energy landscape. The system therefore avoids the pathway of the steepest descent and chooses an alternative longer pathway via the bending soliton that minimizes the friction. We confirm these findings in two experiments with different systems. In the system of solid spheres systems follows the lower friction pathway (not the shortest pathway). A system of ferrofluid droplets will choose the pathway of steepest decent. These findings were supported with agreeable numerical simulations which were able to confirm experimental results.

We have also realized a system that can perform propelling motion above a solid-liquid interface. We have shown that the interplay between dipolar interactions created by external magnetic fields and gravity forces an ensemble of paramagnetic beads into a ribbon. The twist of the ribbon is a mathematical property of the finite cross section of the ribbon that is absent in slender bodies. It can be controlled by the frequency and the eccentricity of the applied precessing field. The ribbon changes from a flat lying ribbon via travelling twist domain walls toward a standing ribbon. In the frequency regime where domain walls are formed, the ribbon is propelled along its axis. The geometrical efficiency of propulsion scales with the domain wall density. Beside the propulsion efficiency we have shown that for a certain frequency and experimental conditions the system will experience “oscillating” behavior. The domain walls with alternating wave lengths will travel through the ribbon. For this “oscillating” behavior we do not have a proper theoretical explanation, but from experimental observations, we believe that the length of the ribbon has a crucial role which will generate oscillating domain walls traveling through the ribbon. For more detailed and theoretically sustained explanations there is a need to perform further experimental measurements and computer simulations.

Beside propulsion motion we have shown that our colloidal system can perform different types of behavior depending on the frequency and eccentricity of the external magnetic field. We have shown how we can successfully heal the system and remove all defects from the system. By changing the eccentricity of the field we were able to reorganize the unhealed ribbons into the healed ones. By further change in the eccentricity we were able to transform the system from a ribbon into a single chain and into a cluster by simply changing the field frequency and eccentricity. By changing these parameters we could expand and compress the ribbon. By expansion and compression we can draw the system from single chain to the cylinder which can perform very stable rotational motion. This process is reversible and can be completely controlled externally, which makes this system a very good candidate for further research in the field of dynamic self-assembly.

## Zusammenfassung

In dieser Arbeit haben wir die dynamische Selbstassemblierung Mikrometer großer paramagnetischer Partikel an einer flüssig festen Grenzfläche studiert. Durch abruptes anlegen von Magnetfeldern bei hohen Masonzahlen konnten wir bisher nicht beobachtete Bewegungen von magnetischen Ketten und Bändern erzeugen. Wir haben gezeigt, dass in unserem kolloidalen System, die Kinetik des Faltungsprozesses durch hydrodynamische Reibung entlang der Abhänge der Energielandschaft, und nicht durch Übergangsraten über Sattelpunkte bestimmt ist. Der kürzeste über ein Verkumpeln der Kette führende Faltungspfad von einer Kette zu einem Cluster wird nicht durch Energiebarrieren sondern durch die beim aneinander vorbei Gleiten der Partikeloberflächen auftretende Reibung unterdrückt. Das System vermeidet also den Pfad des steilsten Abstieges und wählt einen längeren dafür weniger dissipativen Faltungspfad, welcher die Reibung minimiert. Experimente an zwei unterschiedlichen Systemen bestätigen diese Ergebnisse: Das System aus harten Kugeln folgt dem längeren Pfad minimaler Reibung. Ein System aus flüssigen Ferrofluidtropfen wählt den kürzesten Pfad des steilsten Abstieges. Unsere numerischen Studien zu beiden Systemen sind in Übereinstimmungen mit diesen experimentellen Ergebnissen.

Wir haben darüberhinaus ein System realisiert welches sich über einer flüssig festen Grenzfläche schwimmend fortbewegt. Wir haben gezeigt, dass das Zusammenspiel durch externe Magnetfelder induzierter dipolarer Wechselwirkungen mit der Gravitation, eine Ansammlung paramagnetischer Partikel in die Form eines Bandes zwingt. Die Verdrillung des Bandes ist eine mathematische Eigenschaft des endlich großen Bandquerschnittes, die in einem schlanken Körper nicht vorkommt. Sie kann durch die Frequenz und die Exzentrizität des angelegten externen Magnetfeldes kontrolliert werden. Das Band verändert sich als Funktion beider Parameter von einem flachen liegenden Band über wandernde Verdrillungswände hin zu einem flachen stehenden Band. Im Frequenzbereich der wandernden Verdrillungswände schwimmt das Band entlang seiner Längsachse. Die geometrische Effizienz der Schwimmbewegung skaliert mit der Verdrillungswanddichte. Des Weiteren tritt bei bestimmten Frequenzen ein Zweierzyklus abwechselnd kurz- und langwelliger wandernder Verdrillungswände aus, der bisher theoretisch nicht erklärt werden kann, aber vielleicht mit der Kommensurabilität der Wellenzüge mit der Bandlänge zu tun hat. Hier können weitere Experimente und Computersimulationen vielleicht eine Antwort liefern.

Nicht nur die Schwimmeffizienz sondern das gesamte dynamische Verhalten des Bandes kann durch die Frequenz und die Exzentrizität des externen Magnetfeldes verändert werden. Wir haben gezeigt dass ein Band durch zeitliche Variation der Exzentrizität von Banddefekten geheilt werden kann, bzw. durch Variation der Frequenz und Exzentrizität auch in eine Einzelkette oder einen Cluster verwandelt werden kann. Die Formveränderungen erfolgen über eine Expansion bzw. Kompression des Bandes. Auch kann ein Band zu einem in sich geschlossenen Zylinder zusammengerollt werden, der dann eine stabile Rotationsbewegung ausführt. Alle Prozesse sind reversibel und können vollständig durch das externe Feld kontrolliert werden. Die macht unser System zu einem guten Kandidaten für weitere Untersuchungen zur dynamischen Selbstassemblierung.



# 8 Bibliography

- [1] C. B. Anfinsen and H. A. Scheraga, “Experimental and theoretical aspects of protein folding”, *Adv. Protein Chem.*, **29**, 205-300, (1975).
- [2] J. N. Onuchic, Z. Luthey-Schulten and P. G. Wolynes, “Theory of protein folding: the energy landscape perspective”, *Annu. Rev. Phys. Chem.*, **48**, 545-600, (1997).
- [3] B. Nolting, *Protein Folding Kinetics: Biophysical Methods* (Springer, Berlin) 1999.
- [4] W. A. Eaton, V. Muñoz, S. J. Hagen, G.S. Jas, L.J. Lapidus, E.R. Henry, J. Hofrichter, ”Fast kinetics and mechanisms in protein folding”, *Annu. Rev. Biophys. Biomol. Struct.*, **29**, 327-359, (2000).
- [5] V. Daggett and A. Fersht, “The present view of the mechanism of protein folding”, *Nat. Rev. Mol. Cell Biol.*, **4**, 497-502, (2003).
- [6] J. D. Bryngelson, J. N. Onuchic, N. D. Socci, P. G. Wolynes,” Funnels, pathways, and the energy landscape of protein folding: a synthesis”, *Proteins: Struct. Funct. Genetics*, **21**, 167-195, (1995).
- [7] N. Kikuchi, J. F. Ryder, C. M. Pooley, J. M. Yeomans, ”Kinetics of the polymer collapse transition: the role of hydrodynamics”, *Phys. Rev. E*, **71**, 061804, (2005).
- [8] M. Cieplak and S. Niewieczerał, ” Hydrodynamic interactions in protein folding”, *J. Chem Phys.*, **130**, 124906, (2009).
- [9] A. van Blaaderen, R. Ruel, P. Wiltzius,” Template-directed colloidal crystallization”, *Nature* **385**, 321-324, (1997).

- 
- [10] E. R. Weeks, J. C. Crocker, A. C. Levitt, A. Schofield, D. A. Weitz, "Three-Dimensional Direct Imaging of Structural Relaxation Near the Colloidal Glass Transition", *Science*, 287, 627-631, (2000).
- [11] N. Osterman, I. Poberaj, J. Dobnikar, D. Frenkel, P. Zihlerl, and D. Babić, "Field-Induced Self-Assembly of Suspended Colloidal Membranes", *Phys. Rev. Lett.*, **103**, 228301, (2009).
- [12] J. Baumgartl, M. Zvyagolskaya and C. Bechinger, "Tailoring of phononic band structures in colloidal crystals", *Phys. Rev. Lett.*, **99**, 205503, (2007).
- [13] R. Toussaint, G. Helgesen and E. G. Flekkoy, "Dynamic roughening and fluctuations of dipolar chains", *Phys. Rev. Lett.*, **93**, 108304, (2004).
- [14] P. Tierno, R. Muruganathan and T. M. Fischer, "Viscoelasticity of dynamically self-assembled paramagnetic colloidal clusters", *Phys. Rev. Lett.*, **98**, 028301, (2007).
- [15] P. Tierno, J. Claret, F. Sagués, A. Cēbers, "Overdamped dynamics of paramagnetic ellipsoids in a precessing magnetic field", *Phys. Rev. E*, **79**, 021501, (2009).
- [16] A. P. Gast and C. F. Zukoski, "Electrorheological fluids as colloidal suspensions", *Adv. Colloid Interface Sci.*, **30**, 153-202, (1989).
- [17] S. Melle, O. G. Calderón, M. A. Rubio, G. G. Fuller, "Microstructure evolution in magnetorheological suspensions governed by Mason number", *Phys. Rev. E*, **68**, 041503, (2003).
- [18] S. L. Biswal and A. P. Gast, "Rotational dynamics of semiflexible paramagnetic particle chains", *Phys. Rev. E*, **69**, 041406, (2004).

- [19] J. Černák and G. Helgesen, “Aggregation of magnetic holes in a rotating magnetic field”, *Phys. Rev. E*, **78**, 061401, (2008).
- [20] V. G. Levich, *Physicochemical Hydrodynamics* (Prentice-Hall, Englewood Cliffs, NJ), 1962.
- [21] H. Tanaka and T. Araki, “Simulation method of colloidal suspensions with hydrodynamic interactions: fluid particle dynamics”, *Phys. Rev. Lett.*, **85**, 1338, (2000).
- [22] P. Peyla, “Rheology and dynamics of a deformable object in a microfluidic configuration: A numerical study”, *Europhysics Letters (EPL)*, **80**, 34001, (2007).
- [23] J. Rotne and S. Prager, “Variational Treatment of Hydrodynamic Interaction in Polymers”, *J. Chem. Phys.*, **50**, 4831, (1969).
- [24] Thomas B. Jones, “Electromechanics of Particles”, *Cambridge University Press*, Cambridge, 1995.
- [25] S. Melle, G. G. Fuller, and M. A. Rubio, “Structure and dynamics of magnetorheological fluids in rotating magnetic fields”, *Phys. Rev. E*, **61**, 4111-4117, (2000).
- [26] S. Melle, M. A. Rubio, and G. G. Fuller, “Orientation dynamics of magnetorheological fluids subject to rotating external fields”, *Int. J. Mod. Phys. B*, **15**, 758-766, (2001).
- [27] S. Melle and J. E. Martin, “Chain model of a magnetorheological suspension in a rotating field”, *J. Chem. Phys.*, **118**, 9875, (2003).
- [28] J. E. Martin, “Thermal chain model of electrorheology and magnetorheology”, *Phys. Rev. E*, **63**, 011406, (2000).

- 
- [29] S. Melle, O. G. Calderón, M. A. Rubio, and G. G. Fuller, “Rotational dynamics in dipolar colloidal suspensions: video microscopy experiments and simulation results”, *J. Non-Newtonian Fluid Mech.*, **102**, 135-148, (2002).
- [30] S. Melle, O. G. Calderón, M. A. Rubio, and G. G. Fuller, “Chain rotational dynamics in MR suspensions”, *Int. J. Mod. Phys. B*, **16**, 2293-2299, (2002).
- [31] O. Sandre, J. Browaeys, R. Perzynski, V. Cabuil, R. E. Rosensweig, “Assembly of microscopic highly magnetic droplets: Magnetic alignment versus viscous drag”, *Phys. Rev. E*, **59**, 1736–1746, (1999).
- [32] P. Domínguez-García, S. Melle, J. M. Pastor, and M. A. Rubio, “Scaling in the aggregation dynamics of a magnetorheological fluid”, *Phys. Rev. E*, **76**, 051403, (2007).
- [33] J. H. E. Promislow and A. P. Gast, “Aggregation kinetics of paramagnetic colloidal particles”, *J. Chem. Phys.*, **102**, (1995).
- [34] G. Bossis, O. Volkova, S. Laciš, and A. Meunier, “Magnetorheology: Fluids, Structures and Rheology”, Stefan Odenbach (Ed.): LNP 594, pp. 202–230, 2002, *Springer-Verlag Berlin Heidelberg* 2002.
- [35] H. Löwen, “Colloidal soft matter under external control”, *J. Phys.: Condens. Matter*, **13**, R415–R432, (2001).
- [36] P. Domínguez-García, S. Melle, O. G. Calderón, M. A. Rubio, “Doublet dynamics of magnetizable particles under frequency modulated rotating fields”, *Colloids and Surfaces A: Physicochem. Eng. Aspects*, **270-271**, 270–276, (2005).
- [37] J. de Vicente, D. J. Klingenberg and R. Hidalgo-Alvarez, “Magnetorheological fluids: a review”, *Soft Matter*, **7**, 3701-3710, (2011).

- [38] C. Wilhelm, F. Gazeau, and J.-C. Bacri, "Rotational magnetic endosome microrheology: Viscoelastic architecture inside living cells", *Phys. Rev. E*, **67**, 061908 (2003).
- [39] I. Petousis, E. Homburg, R. Derks and A. Dietzel, "Transient behaviour of magnetic micro-bead chains rotating in a fluid by external fields", *Lab on a Chip*, **7**, 1746–1751, (2007).
- [40] E. M. Furst and A. P. Gast, "Dynamics and lateral interactions of dipolar chains", *Phys. Rev. E*, **62**, 6916-6925, (2000).
- [41] P. G. de Gennes, *Soft Matter*, this lecture was delivered 9 December 1991, on the occasion of the presentation of the 1991 Nobel Prize in Physics
- [42] D. G. Grier, "A revolution in optical manipulation", *Nature*, **424**, 810-816, (2003).
- [43] F. Leal Calderon, T. Stora, O. Mondain-Moncal, P. Poulin, J. Bibette, "Direct measurement of colloidal forces", *Phys. Rev. Lett.*, **72**, 2959, (1994).
- [44] R. Dreyfus, D. Lacoste, J. Bibette, and J. Baudry, "Measuring colloidal forces with the magnetic chaining technique", *Eur. Phys. J. E*, **28**, 113-123, (2009).
- [45] B. B. Yellen, O. Hovorka, G. Friedman, "Arranging matter by magnetic nanoparticle assemblers", *PNAS*, **102** (25), 8860-8864 (2005).
- [46] S. Krishnamurthy, A. Yadav, P. E. Phelan, R. Calhoun, A. K. Vuppu, A. A. Garcia, M. A. Hayes, "Dynamics of rotating paramagnetic particle chains simulated by particle dynamics, Stokesian dynamics and lattice Boltzmann methods", *J. Phys. Microfluid Nanofluid*, **5**, 33–41, (2008).
- [47] W. M. Winslow, U.S. Patent 25, No.2417850, (1947).

- 
- [48] W. M. Winslow, “Induced Fibration of Suspensions”, *J. Appl. Phys.*, **20**, 1137-1140, (1949).
- [49] J. Rabinow, “The Magnetic Fluid Clutch”, *AIEE Trans.*, **67**, 1308-1315, (1948).
- [50] A. S. Silva, R. Bond, F. Plouraboué, and D. Wirtz, “Fluctuation dynamics of a single magnetic chain”, *Phys. Rev. E*, **54** (5), 5502-5510, (1996).
- [51] B. J. Park, F. F. Fang and H. J. Choi, “Magnetorheology: materials and application”, *Soft Matter*, **6**, 5246–5253, (2010).
- [52] G. Helgesen and A. T. Skjeltorp, ” An experimental system for studying dynamic behavior of magnetic microparticles”, *J. Appl. Phys.*, **69**, 8277-8284, (1991).
- [53] D. Liu, M. R. Maxey and G. E. Karniadakis, “Simulations of dynamic self-assembly of paramagnetic microspheres in confined microgeometries”, *J. Micromech. Microeng.*, **15**, 2298–2308, (2005).
- [54] J. T. Lee, A. Abid, K. H. Cheung, L. Sudheendra, I. M. Kennedy, ”Superparamagnetic particle dynamics and mixing in a rotating capillary tube with a stationary magnetic field”, *Microfluid Nanofluidics*, **13**, 461–468, (2012).
- [55] G. Helgesen, P. Pieranski, and A. T. Skjeltorp., “Nonlinear Phenomena in Systems of Magnetic Holes”, *Phys. Rev. Lett.*, **64**, (1990).
- [56] T. G. Kang, M. A. Hulsen and J. M. J. den Toonder, “Dynamics of magnetic chains in a shear flow under the influence of a uniform magnetic field”, *Physics of Fluids*, **24**, 042001, (2012).
- [57] G. M. Whitesides and B. Grzybowski, “Self-Assembly at All Scales”, *Science*, **295**, 2418-2421, (2002).

## 8 Bibliography

---

- [58] A. Snezhko, “Non-equilibrium magnetic colloidal dispersions at liquid–air interfaces: dynamic patterns, magnetic order and self-assembled swimmers”, *J. Phys.: Condens. Matter*, **23**, (2011).
- [59] S. K. Smoukov, S. Gangwal, M. Marquezbc and O. D. Velev, “Reconfigurable responsive structures assembled from magnetic Janus particles”, *Soft Matter*, **5**, 1285–1292, (2009).
- [60] R. Dreyfus, J. Baudry, M. L. Roper, M. Fermigier, H. A. Stone and J. Bibette, ”Microscopic artificial swimmer”, *Nature*, **437**, 862, (2005).
- [61] S. C. Glotzer, M. J. Solomon, and N. A. Kotov, “Self-Assembly: From Nanoscale to Microscale Colloids”, *American Institute of Chemical Engineers (AIChE)Journal*, **50**, No. 12, (2004).
- [62] <http://www.merriam-webster.com/dictionary/assembly>.
- [63] B. A. Grzybowski, C.E. Wilmer, J. Kim, K. P. Browne and K. J. M. Bishop, “Self-assembly: from crystals to cells”, *Soft Matter*, **5**, 1110–1128, (2009).
- [64] G. A. Ozin,, K. Hou, B. V. Lotsch, L. Cademartiri, D. P. Puzzo, F.Scotognella, A.Ghadimi and J. Thomson, “Nanofabrication by self-assembly”, *Materialstoday*; **12**, 12-23, (2009)
- [65] M. Fialkowski, K. J. M. Bishop, R. Klajn, S. K. Smoukov, C. J. Campbell, and B. A. Grzybowski, “Principles and Implementations of Dissipative (Dynamic) Self-Assembly”, *J. Phys. Chem. B*, **110**, 2482-2496, (2006).
- [66] K. V. Tretyakov, K.J. M. Bishop and B. A. Grzybowski, “The dependence between forces and dissipation rates mediating dynamic self-assembly”, *Soft Matter*, **5**, 1279–1284, (2009).

- 
- [67] B. A. Grzybowski and G. M. Whitesides, “Directed dynamic self-assembly of objects rotating on two parallel fluid interfaces”, *J. Chem. Phys.*, **116**, (2002).
- [68] B. A. Grzybowski and C. J. Campbell, “Complexity and dynamic self-assembly”, *Chemical Engineering Science*, **59**, 1667-1676, (2004).
- [69] L. Li, M. H. Köpf, S.V. Gurevich, R. Friedrich and L. Chi, “Structure Formation by Dynamic Self-Assembly”, *small*, **8**, 488–503, (2012).
- [70] M. Grzelczak, J. Vermant, E.M. Furst, and L. M. Liz-Marzán, “Directed Self-Assembly of Nanoparticles”, *ACS Nano*, **4**, 3591–3605, (2010).
- [71] L. E. Helseth, “Self-Assembly of Colloidal Pyramids in Magnetic Fields”, *Langmuir*, **21**, 7276–7279, (2005).
- [72] A. Snezhko, I. S. Aranson and W.-K. Kwok, “Surface Wave Assisted Self-Assembly of Multidomain Magnetic Structures”, *Phys. Rev. Lett.*, **96**, 078701, (2006).
- [73] A. Snezhko, M. Belkin, I. S. Aranson and W.-K. Kwok, “Self-Assembled Magnetic Surface Swimmers”, *Phys. Rev. Lett.*, **102**, 118103, (2009).
- [74] E. M. Purcell, “Life at low Reynolds number”, *Am. J. Phys.* **45**, 3 (1977).
- [75] M. Manghi, X. Schlagberger and R. R. Netz, “Propulsion with a Rotating Elastic Nanorod”, *Phys. Rev. Lett.*, **96**, 068101, (2006).
- [76] P. Dhar, Th. M. Fischer, Y. Wang, T. E. Mallouk, W. F. Paxton and A. Sen, “Autonomously Moving Nanorods at a Viscous Interface”, *Nano Letters*, **6**, 66-72, (2006).

- [77] O. S. Pak, W. Gao, J. Wang and E. Lauga, “Reconfigurable responsive structures assembled from magnetic Janus particles”, *Soft Matter*, **7**, 8169–8181, (2011).
- [78] P. Tierno, O. Güell, and F. Sagués, “Controlled propulsion in viscous fluids of magnetically actuated colloidal doublets”, *Phys. Rev. E*, **81**, 011402, (2010).
- [79] Y. Nagaoka, H. Morimoto, and T. Maekawa, “Ordered Complex Structures Formed by Paramagnetic Particles via Self-Assembly Under an ac/dc Combined Magnetic Field”, *Langmuir*, **27**, 9160–9164, (2011).
- [80] N. Pamme, “Magnetism and microfluidics”, *Lab on a Chip*, **6**, 24–38, (2006).
- [81] Matthew N.O. Sadiku “Elements of electromagnetics”, 3rd Edition, *Oxford University Press*, Oxford, 2011.
- [82] S. Kim and S.J. Karrila, “Microhydrodynamics: Principles and Selected Applications”, *Dover Publications Inc.*, Mineola, New York, 2005.
- [83] M. Reichert, “Hydrodynamic Interactions in Colloidal and Biological Systems”, *PhD thesis*, Universität Konstanz, 2006,  
<http://nbn-resolving.de/urn:nbn:de:bsz:352-opus-19302>.
- [84] P. Mazur and W. van Saarloos, “Many-sphere hydrodynamic interactions and mobilities in a suspension”, *Physica A: Statistical Mechanics and its Applications*, **115**, 21-57, (1982).
- [85] J. Happel and H. Brenner, “Low Reynolds Number Hydrodynamics”, *Martinus Nijhoff Publishers*, 1983.
- [86] Edward J. Shaughnessy, Jr., Ira M. Katz and James P. Schaffer, “Introduction to fluid mechanics”, *Oxford University Press*, 2005.

- 
- [87] L.D. Landau and E.M. Lifshitz, “Fluid Mechanics Second edition”, *Pergamon Press*, London, 1987.
- [88] J.K.G. Dhont, “An Introduction to Dynamics of Colloids”, *Elsevier*, Amsterdam, 2005.
- [89] C.A. Condat, R.A. Guyer, and M. D.Miller,” Double Sine-Gordon Chains”, *Phys. Rev. B*, **27**, 474–494, (1983).
- [90] Yu. S. Kivshar, N. Gronbech-Jensen, and M. R. Samuelsen, “ $\pi$ -kinks in a parametrically driven sine-Gordon chain”, *Phys. Rev. B*, **45**, 7789-7797, (1992).
- [91] Yu. S. Kivshar, N. Gronbech-Jensen, and R. D. Parmentier, “Kinks in the presence of rapidly varying perturbations”, *Phys. Rev. E*, **49**, 4542-4551, (1994).
- [92] Yu. S. Kivshar, A. Sánchez, and L. Vázquez, “Kink decay in a parametrically driven  $\phi^4$  chain”, *Phys. Rev. A*, **45**, 1207-1212, (1992).
- [93] Yu. S. Kivshar and A. Sánchez, “Kink Drift in Oscillating Fields”, *Phys. Rev. Lett.*, **77**, 582-582, (1996).
- [94] N. R. Quintero and A. Sánchez, “ac driven sine-Gordon solitons: dynamics and stability”, *Eur. Phys. J. B*, **6**, 133-142, (1998).
- [95] M. J. Rice and E. J. Mele, “Phenomenological theory of soliton formation in lightly-doped polyacetylene”, *Solid State Commun.*, **35**, 487-491, (1980).
- [96] M. J. Rice, “Physical dynamics of solitons”, *Phys. Rev. B*, **28**, 3587-3589, (1983).
- [97] V. Stehr, P. Müller, F. G. Mertens, and A. Bishop, “Soliton ratchets in sine-Gordon systems with additive inhomogeneities”, *Phys. Rev. E*, **79**, 036601, (2009).

- [98] V. Zharnitsky, I. Mitkov, and N. Grønbech-Jensen, “ $\pi$ -kinks in strongly ac driven sine-Gordon systems” *Phys. Rev. E*, **58**, R52-R55, (1998).
- [99] H. C. Berg, “Dynamic properties of bacterial flagellar motors”, *Nature*, **249**, 77-79, (1974).
- [100] C. Eloy and E. Lauga, “Kinematics of the most efficient cilium”, *Phys. Rev. Lett.*, **109**, 038101, (2012).
- [101] J. Lighthill, “Flagellar Hydrodynamics: The John von Neumann Lecture, 1975”, *Siam. Rev.*, **18**, 161-230, (1976).
- [102] J. Lighthill, “Helical distributions of stokeslets”, *J. Eng. Math.*, **30**, 35-78, (1996).
- [103] O. Pironneau, and D. F. Katz, “Optimal swimming of flagellated microorganisms”, *J. Fluid. Mech.*, **66**, 391-415, (1974).
- [104] A. T. Chwang, and T. Y. -T. Wu, “Hydromechanics of low-Reynolds-number flow. Part 2. Singularity method for Stokes flows”, *J. Fluid. Mech.*, **67**, 787-815, (1975).
- [105] H.Wada, R. R. Netz, “Model for Self-Propulsive Helical Filaments: Kink-Pair Propagation”, *Phys. Rev. Lett.*, **99**, 108102, (2007).
- [106] A. Beveratos, I. Sagnes, S. Haliyo and S. Regnier G. Hwang, R. Braive, L. Couraud, A. Cavanna, O. Abdelkarim, I. Robert-Philip, “Electro-osmotic propulsion of helical nanobelt swimmers”, *Int. J. Robot. Res.*, **30**, 806-819,(2011).
- [107] R. Livanovics and A. Cebers, “Magnetic Dipole with a Flexible Tail As a Self-Propelling Microdevice”, *Phys. Rev. E*, **85**, 041502, (2012).

- 
- [108] J. J. L. Hidgon, “The hydrodynamics analysis of flagellar propulsion: helical waves”, *J. Fluid Mech.*, **94**, 331-351, (1979).
- [109] L. Zhang, J. J. Abbott, L. Dong, B. E. Kratochvil, D. Bell, and B. J. Nelson, “Artificial bacterial flagella: Fabrication and magnetic control”, *Appl. Phys. Lett.*, **94**, 064107, (2009).
- [110] B. A. Grzybowski, J.A. Wiles, and G. Whitesides, “Dynamic self-assembly of rings of charged metallic spheres” *Phys. Rev. Lett.* , **90**, 083903 (2003).
- [111] G. Calugareanu, “L'intégrale de Gauss et l'analyse des noeuds tridimensionnels”, *Rev. Math. Pures Appl.*, **4**, 5-20, (1959).
- [112] J. Yan, M. Bloom, S. C. Bae, E. Luijten, and S. Granick, “Linking synchronization to self-assembly using magnetic Janus colloids”, *Nature*, **491**, 578-581, (2012).
- [113] D. Tam and A. E. Hosoi, “Optimal stroke patterns for Purcell's three-link swimmer”, *Phys. Rev. Lett.*, **98**, 068105, (2007).
- [114] P.L. Kapitza, “Dynamic stability of a pendulum when its point of suspension vibrates”, *Soviet Phys. JETP*, **21**, 588-592, (1951).
- [115] P.L. Kapitza, “Pendulum with a vibrating suspension“, *Usp. Fiz. Nauk*, **44**, 7-15, (1951).
- [116] U.S. National institutes of health, <http://rsb.info.nih.gov/ij/>.

# Acknowledgement

There are many people I would like to thank for their help, support and friendship over the course of my PhD, and I apologize in advance if I miss anyone out.

First and foremost I would like to acknowledge my supervisors Professor Dr. Thomas Fischer. This work would not have been possible without his advice, personal guidance, enthusiasm, understanding and for the doors always opened for all my questions. I would like to thank to him for his confidence in my work even at times when results were not present. I will remain forever grateful to him.

I would also like to acknowledge to Dr. Ziad Khattari from the Hashemite University, Jordan and to Dr. Pietro. Tierno from the Universitat de Barcelona, Spain and to Dr. Natalia Wilke from the Universidad Nacional de Cordoba, Argentina. I would also like to acknowledge Prof. Dr. Walter Zimmermann, Dr. Steffen Schreiber and Dr. Levan Jibuti from Theoretical Physics I, to Prof. Dr. Franz G. Mertens, Niurka Quintero and Renato Alvarez-Nodarse from the University of Seville, Spain.

I would like to say thank you to Carmen Kerling, Klaus Oetter, Christine Linser for their help with the technical, official and administrative works. I would also like to thank all the members of Experimental Physics V.

I take this opportunity to thank all my group members present and former : Uli Langer, Ayan Ray, Tobias Gehring, Saeedeh Aliaskarisohi, Thomas “Boschlein” Bohlein for the great time in the lab and outside of the lab and Christiane “die Deutsch Lehrerin” Jungnickel for her help towards making learning the German language easier and for beating me up occasionally at the taekwondo course at the University of Bayreuth. I would like to thank to present members of our group, Fabian, Sergej, Jürgen, Johannes and Nils. I would like to say thank you to Robert “Bob” Myhill and Esther Posner for heroic fight with English grammar.

I take this opportunity to express my thanks to my friends here in Bayreuth: Andrija, David, Florence, Blanka, Sabine, ToCo, Basti, and I apologize if I forgot somebody. Also I would like to thanks to my friends in Serbia. Big thanks to Ćelava, Miloš, Jovče, Jelena, Kiza, Nada, Džever, Bambi, Ivana, Biljana, Bidžana, Ljilja, Vladi and Nadi Brdarić, Jelena Tripković, to family Žarković, to my friends from the days in the Army, etc.

---

I would like to thank to my mother Draga and to my father Branko for giving me support and love whenever I needed. Without their love I could not have succeeded. I would like to say thanks to my brother Aleksandar, his wife Dragana and their children Tamara and Ivan. Last but not least I would like to say thank you Natalia for making my life colorful.

---

Parts of the research work outlined in this dissertation have been published in:

1. N. Casic, S. Schreiber, P. Tierno, W. Zimmermann and T. M. Fischer, „Friction-controlled bending solitons as folding pathway toward colloidal clusters“, *Europhysics Letters (EPL)*, **90**, (2010), 58001
2. N. Casic, N. Quintero, R. Alvarez-Nodarse, F. Mertens, L. Jibuti, W. Zimmermann, and T. M. Fischer, “Propulsion efficiency of a dynamic self assembled helical ribbon“, *Phys. Rev. Lett.*, **110**, 168302, (2013)

